Mineralogical variation in the basal Upper Zone, Bushveld Igneous Complex, South Africa: implications for ore genesis and mineral extraction

A thesis submitted in fulfilment of the requirements for the degree of

MASTER OF SCIENCE

At

Rhodes University

By

Darryn Ashley van Huyssteen

Department of Geology

Rhodes University, South Africa

Abstract

The 2000 m thick Upper Zone of the Bushveld Igneous Complex hosts approximately 20 m of vanadium-bearing titaniferous magnetite in layers distributed throughout a sequence of magnetite-bearing gabbroic rocks. The Main Magnetite Layer is mined for its ca. 1.8 wt. % V_2O_3 (and is currently the most economically exploited ore layer) however, ore layers in the basal Upper Zone are also being targeted for their high V_2O_3 contents. From the 150 m sampled section below the Main Magnetite Layer, EPMA spot analysis conducted on numerous magnetite grains, it has been established that V_2O_3 contents are highest in magnetite occurring within the extensively weathered disseminated magnetite gabbroic rocks situated near the surface (ca. 1.26 wt. % V_2O_3). The fresh disseminated magnetite gabbro averages 1.13 wt. % V_2O_3, while the magnetite layer itself (> 90 % magnetite) averages only 1.05 wt. % V_2O_3.

Major and trace element geochemistry illustrates a strong mineralogical control on whole-rock geochemistry by the presence of Fe-Ti oxides. Cr has a pronounced vertical depletion from the base of the magnetite layer (> 7000 ppm) to the top (<100 ppm), which can be interpreted as a layered melt model involving bottom crystallisation of magnetite and a slow rate of supply of material to the crystallisation zone. V, Nb, Co and Ni (also highly compatible in magnetite) show a more gradual depletion profile from the base of the magnetite layer upwards, suggesting magnetite layer formation may not be due to processes of early fractional crystallisation from a single magma pulse. Injections of new magma pulses are not likely responsible for magnetite layer formation, on the basis that plagioclase An % above and below the magnetite layer are remarkably similar. However, higher An % of plagioclase and Mg# of clinopyroxene within the magnetite layer suggests magma mixing processes may be operating, most likely due to convective overturn within the stratified magma chamber.

It is postulated that a magma undergoing silicate-dominated fractionation (crystallising cotectic proportions of plagioclase and pyroxene) switched to magnetite crystallisation as a result of an increase in fO_2 or a change in pressure throughout the magma chamber. Consequently, gravity settling of dense magnetite to the floor of the chamber occurs, thus

creating a monominerallic magnetite layer. Regular crystallisation of a silicate-dominated system is then recommenced once the phase boundary is re-shifted.

Fe-Ti oxide oxidation exsolution features throughout the magnetite layer provide further diagnostic evidence for increases in fO_2 within the magma chamber. Most common is internal granular ilmenite exsolution textures, followed by external granular ilmenite exsolution. This is in agreement with the assumption that higher fO_2 prevailed during formation of magnetite layers. In contrast, disseminated magnetite gabbroic rocks do not show internal or external granular ilmenite exsolution but rather lower oxidation degree microtextures. These are most commonly abundant cloth-textured ulvöspinel and trellis intergrowths of ilmenite.

Extraction of magnetite from the highly weathered disseminated magnetite gabbroic rocks seems most plausible as the highest V_2O_3 grades (averaging 1.26 wt. %) occur closest to the Earth's surface; and removal of silicates is a simpler process as they have been weathered to clay minerals. Fresh disseminated magnetite gabbro (averaging 1.13 wt. % V_2O_3) and the magnetite ore layer (averaging 1.05 wt. % V_2O_3) are less attractive economically as they are located at considerably deeper levels than the higher grade weathered product (and contain fresh silicates which are more intimately intergrown with magnetite), making extraction costs higher and therefore less viable.

Declaration

All material contained in this thesis represents the original work of the author except where specific acknowledgement is made to the work of others.

_____

Darryn Ashley van Huyssteen

11th November 2016

Department of Geology

Rhodes University

Grahamstown

6140

Acknowledgements

Firstly, I would like to thank my supervisor, Prof. Stephen Prevec without whom this project would not have been possible. I would like to thank him for the interesting ideas he has provided me with and for countless hours of reviewing and editing drafts. I would also like to thank him for fronting the Magmatic Ore Research Group (MORG) which provided me with much insight into magmatic concepts and applying it to my work.

I would also like to send the greatest thanks to Glencore and the staff at Rhovan vanadium mine, for allowing access to the company's core yard and mine pit and for kindly providing the samples for this study. Without you this project would not have been possible. Further, I would also like to thank the National Research Foundation (NRF) for providing me with financial aid over the two years of study.

Lastly, I would like to thank various individuals who helped with technical aspects and data analysis, also whom without this project would not have been possible. Massive thanks to the technicians at Rhodes University (Mr. Chris Pikoli and Thulani Royi) for their sample preparation and thin section production. I would also like to thank Thapelo Moloto for her assistance with EPMA analysis, Prof. J.S (Goonie) Marsh for XRF analysis and to the staff at Geoscience Laboratories (Sudbury, Canada) for their analysis of whole-rock geochemistry and for providing quality data.

Table of Contents

Figure and Table captions

Figures

Tables

1. Introduction

Layered mafic intrusions play host to major economic ore deposits of Ni-Cu-PGE, Cr and Fe-Ti-V. With an aerial extent of about 66 000 km² (Willemse, 1969), the Bushveld Igneous Complex (BIC) is the largest known layered intrusion in the world, hosting the world's largest chromite and PGE deposits (Saager, 1984) as well as the third largest vanadium (V) deposit (see Figure 1.2). Fe-Ti oxide ore layers are common occurrences in the upper parts of layered ultramafic-mafic intrusions and less commonly at the base of such intrusions (Eales and Cawthorn, 1996). However, few layered intrusions actually contain an entire suite of potentially economic oxide-rich layers as these may have been tectonically disrupted, e.g. the Stillwater and Penikat Complexes (Eales and Cawthorn, 1996). The BIC and the Windimurra Complex in Western Australia are good examples of Fe-rich trends leading to the development of Fe-Ti oxide ore layers in the upper parts of the complex (Eales and Cawthorn, 1996). Other intrusions with similar Fe-Ti oxide deposits include the Panzhihua intrusion (SW China) and smaller Rooiwater and Ushushwana Complexes in SA.

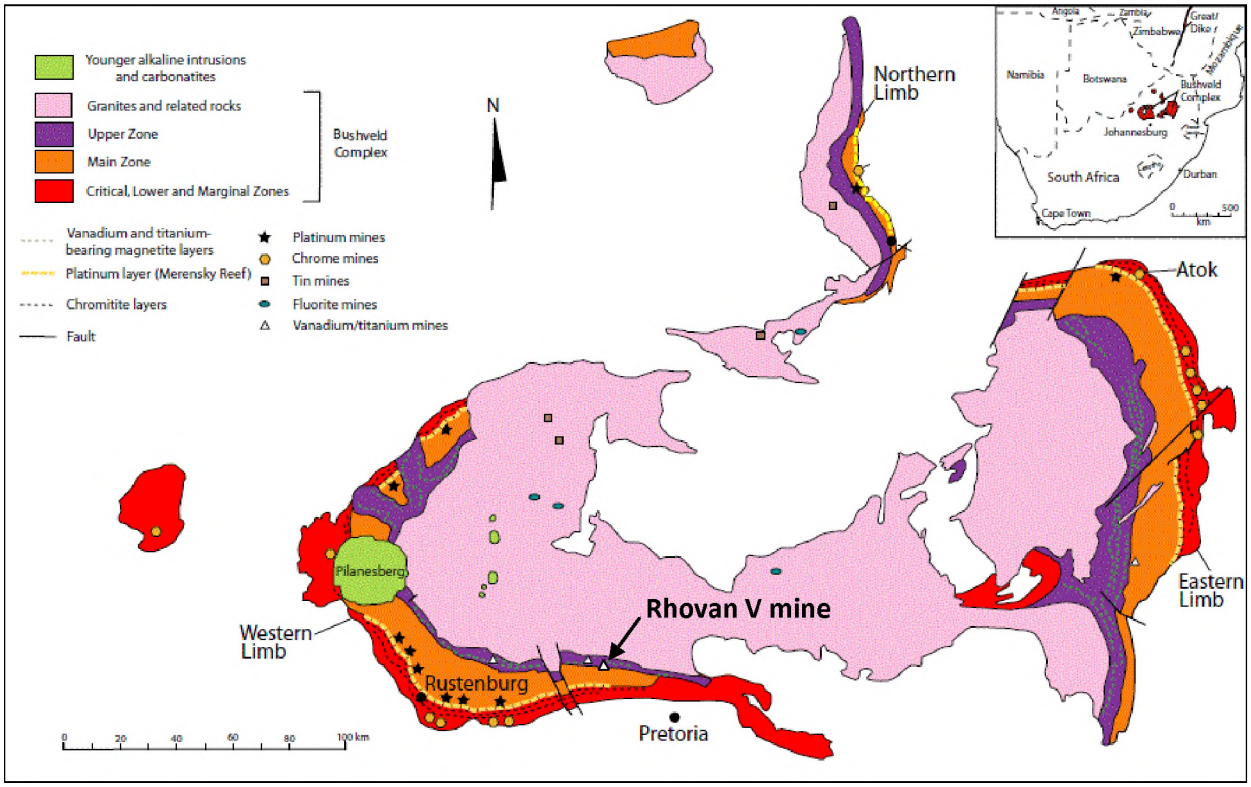

Figure 1.1: Geological map of the Bushveld Igneous Complex and related ore deposits as well as the position of Rhovan V mine (modified after Viljoen and Schurmann, 1998).

1.1. Vanadium occurrences, uses and worldwide production

V is found in over 50 different minerals and is the 22nd most abundant element in the Earth's crust at a mean concentration of 150 g/t, similar to zinc and more common than copper or nickel (Habashi, 2002). V originates from primary sources such as ores, concentrates, metallurgical slags and petroleum residues (Reese, 2001). The element is never found in its pure state but always in the structure of various minerals, including carnotite, vanadinite, patronite, roscoelite and titaniferous magnetite (Moskalyk *et al.* 2003). It is the titaniferous magnetite-hosted V that is by far the most abundant contributor to the V industry, as deposits in China, South Africa, Russia and Australia all play host to layered mafic intrusions rich in Fe-Ti oxide ore layers. China, South Africa and Russia host the world's largest reserves of V (Figure 1.2) and are also the world's largest producers of ferrovanadium; with world resources of V exceeding 63 million tons (USGS, 2015).

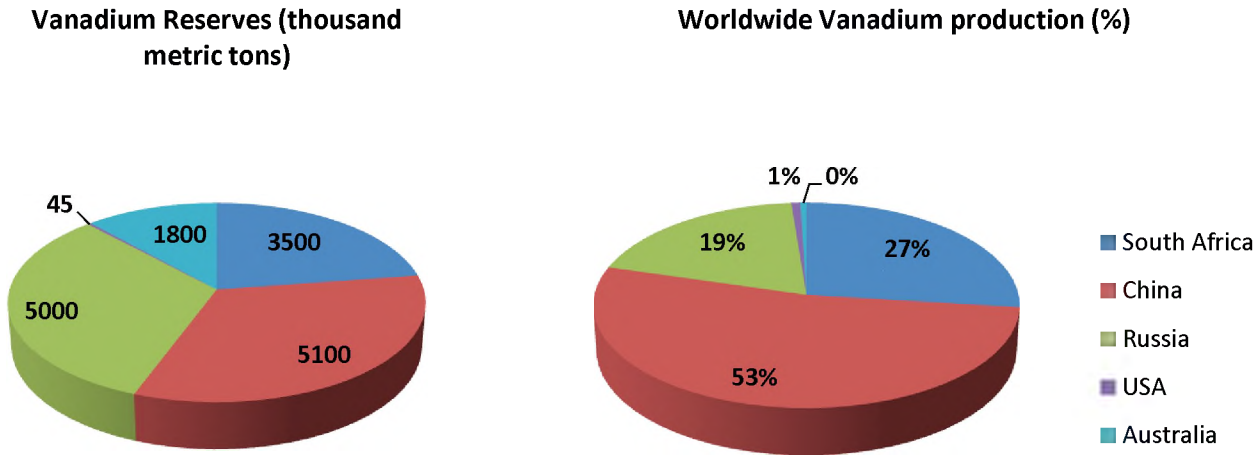

Figure 1.2: Worldwide vanadium reserves (thousand metric tons) as well as vanadium production showing China, Russia and South Africa as the major reserves as well as producers worldwide. Note, South Africa has a much smaller reserve than Russia yet producers more vanadium. Data adopted from USGS (2015).

Many publications cite V_2O_5 content of magnetite, however it is V^{3+} present naturally in magnetite, not V^{5+} (Eales and Cawthorn, 1996). V_2O_5 is the commercially extracted end-product. For the scope of this study, the occurrence of titaniferous magnetite hosted-V is of

particular interest, with core emphasis placed on Fe-Ti oxide ore layers in the basal Upper Zone of the BIC, South Africa. According to Moskalyk *et al.* (2003) V consumption in the iron and steel industry represents roughly 85 % of the V-bearing products produced worldwide. V is employed in a wide range of alloys with applications extending from train rails, tool steels, catalysts, to the aerospace industry (Moskalyk *et al.* 2003). V-bearing materials are treated via several processes (calcium reduction, roasting/leaching, solvent extraction, ion exchange) to recover V either as a metal, ferrovanadium, vanadium pentoxide or in the form of various chemicals (Moskalyk *et al.* 2003).

1.2. Regional geology

The entirety of the BIC comprises of a felsic suite (Rooiberg Group volcanic province, the Rashoop Granophyre Suite and the Lebowa Granite Suite) and a mafic suite (the Rustenburg Layered Suite, hereafter referred to as the RLS). The Complex consists of five limbs, of which only four outcrop in disconnected regions, while the fifth is covered by younger sediment (Eales and Cawthorn, 1996). The RLS consists of an approximately 8 km thick succession of layered mafic and ultramafic rocks intruded into the older rocks of the Transvaal Supergroup (Eales and Cawthorn, 1996; Harney and von Gruenewaldt, 1995). The RLS yields U-Pb isotopic ages spanning over a ca. 7 million year interval, from 2061 to 2054 Ma with major magma emplacement at ca. 2060 and 2055 Ma (Scoates *et al.* 2012). Ages for felsic roof rocks above the Upper Zone diorite range from 2054 to 2056 Ma (Scoates *et al.* 2012), indicating that the mafic and felsic rocks of the BIC are broadly coeval (Van Tongeren *et al.* 2010). Different authors state a variety of ages for the rocks of the BIC although all generally fall within the 2061-2054 Ma time period.

1.2.1. Lithostratigraphic subdivisions

1.2.1.1. Felsic Suite

The Rooiberg Group

The Rooiberg Group is roughly 3-5 km thick and consists from bottom to top of the Dullstroom, Damwal, Kwaggasnek, and Schrikkloof formations (Twist & French, 1983). These rocks represent the roof zone of the complex and are also the first volcanic activity associated with the BIC. The Dullstroom consists of basalt interbedded with andesite, dacite and rhyolite flows; the Damwell primarily of dacite and rhyolite; as well as the Kwaggasnek and Shrikkloof dominated by rhyolites with a higher SiO_2 content (72-74 wt. %) than the previously mentioned formations (Buchanon *et al.* 2002). A Pb-evaporation age of 2061 ± 2 Ma for separated zircons from the Kwaggasnek rhyolites has been determined by Walraven (1997). However, a ^{207}Pb–^{206}Pb concordia age of 2058.9 ± 0.8 Ma obtained by Buick *et al.* (2001) from titanite grains separated from an Upper Zone xenoliths is considered a more reliable age.

Rashoop Granophyre Suite

The Rashoop Granophyre Suite comprises of a group of sills existing throughout the roof zone of the RLS, consisting of three units based on textural variations; the Stavoren Granophyre, the Zwartbank Pseudogranophyre and the Rooikop Granite Porphyry (SACS, 1980). These are generally comprised of micrographic intergrowths of quartz and microcline perthite with accessory plagioclase and hornblende (Mathez *et al.* 2013). Field relationships indicate that the Rashoop Granophyre Suite (2061 ± 5.5 Ma) predates the RLS, confirmed by U-Pb SHRIMP ages calculated by Harmer and Armstrong (2000), but both are somewhat broadly coeval.

Lebowa Granite Suite

The Bushveld granites form a 2-3 km thick sequence of sheet-like sills of highly potassic, magnetite-bearing, A-type granites occupying a total area of 65 000-70 000 km² (Hill *et al.* 1996). The main granites of the Lebowa Granite Suite are the Nebo granites (2054.4 ± 1.8 Ma), occupying most of the central core of the Complex. The granites occur between the RLS and the felsic roof rocks and display intrusive relationships with the Rooiberg rhyolites (Mathez *et al.* 2013).

1.2.1.2. Mafic Suite

The RLS

As previously mentioned, the RLS consists of an approximately 8 km thick succession of layered mafic and ultramafic rocks which have been divided from the base upwards into 5 zones; the Marginal, Lower (LZ), Critical (CZ), Main (MZ) and Upper (UZ) Zones. These units are all briefly outlined below.

The Marginal Zone

The Marginal Zone rocks are unlayered, heterogeneous, noritic rocks which are approximately 800 m thick, forming the base of the Complex (Viljoen and Schurmann, 1998). These norites are generally medium-grained, yet slightly finer grained than those in the central parts of the Complex. The Marginal Zone has been suggested to represent the chilled parent magma to the Complex, although various authors argue against this. For example, Vermaak (1976) suggests this is not the case and that they simply represent composite sills or evolved magmas from within the chamber as a distal facies, while Cawthorn *et al.* (1981) explain that the textural and chemical composition of the norites suggests they are cumulates.

The Lower Zone (LZ)

The Lower Zone reaches a total thickness of 1584 m and can be divided into a basal subzone, lower bronzitite, harzburgite and upper bronzitite (Cameron, 1978). The principle cumulus minerals in the LZ are bronzitite and olivine, with variable chromite as an accessory phase. Plagioclase only occurs in two thin units in the basal subzone (Cameron, 1978). There is no break between the LZ and the CZ, which can be defined by the termination of cumulus olivine in the sequence (Teigler *et al.* 1992). The base of the CZ is determined as the level where interstitial plagioclase in pyroxenite increases from 2 % to 6 % (Cameron, 1978).

The Critical Zone (CZ)

The CZ reaches a maximum thickness of approximately 1500 m and is characterised by regular and rhythmic cyclicity displayed in layers of cumulus chromite hosted in pyroxenites and olivine-rich rocks (Viljoen and Schurmann, 1998). The CZ is broadly subdivided into the Upper CZ (CUZ) and the Lower CZ (CLZ). The CLZ is composed predominantly of bronzitites with lesser chromitites, dunites and harzburgites (Cameron, 1982). On the contrary, the CUZ is composed of more than 70 % norites, with 8 cyclic units of partially complete or complete sequences of an ultramafic base through to norite to anorthosite (Cameron, 1982; Eales and Cawthorn, 1996). Massive reserves of chromite, which are often associated with PGE mineralization, are hosted in the CZ. It is the Upper Group 2 chromitite and the Merensky Reef, two of the world's largest platinum-bearing ore bodies, that make the CZ the most well-researched zone in the BIC.

The Main Zone (MZ)

The Main Zone (MZ) is an approximately 2800 m thick sequence of relatively homogenous (in comparison to the other subdivisions of the RLS) norites and gabbronorites (Eales and Cawthorn, 1996). In comparison to the CZ, the MZ does not display rhythmic layering or lithological complexity and also lacks both olivine and chromite (Eales and Cawthorn, 1996). The MZ is divided into three sections, an upper and lower section containing primary

orthopyroxene and a central section containing pigeonite (von Gruenewaldt, 1973). The MZ also plays host to a distinctive pyroxenite layer, the Pyroxenite Marker, which is located near the top of the sequence.

The Upper Zone (UZ)

The UZ is approximately 2000 m thick and plays host to approximately 20 m of V-bearing titaniferous magnetite in discrete layers, all distributed throughout a sequence of magnetite-bearing gabbroic rocks (Cawthorn and Molyneux, 1986). The most prominent of these is the Main Magnetite Layer (MML) which is currently being mined for its V_2O_3 content (ca. 1.8 wt. % V_2O_3). Layers above the MML are considered uneconomical as the V_2O_3 grade decreases with increasing height. Other mineralisation in the UZ includes localized concentrations of Pt-Pd (Harney *et al*. 1990), vermiculite (von Gruenewaldt, 1973) as well as apatite (P_2O_5) enrichments (Grobler and Whitfield, 1970).

The base of UZ is marked by the first appearance of cumulus magnetite in the sequence and is comprised of a well-layered sequence of magnetite gabbro, anorthosite, massive magnetite layers and olivine-bearing gabbroic rocks (Klemm *et al.* 1985). Von Gruenewaldt (1973) divided the UZ into four subzones on the basis of appearance of new cumulus minerals in the sequence. A basal subzone (subzone A), which is close to 200 m thick, consists of magnetite gabbro interlayered with thin anorthosites and three magnetite layers. The base of the MML marks the base of subzone B (which has the same rock types as subzone A). The appearance of iron-rich olivine marks the base of subzone C which consists of olivine gabbros, magnetite gabbros and magnetite layers. Subzone D is marked by the reappearance of cumulus olivine together with cumulus apatite and rock types include olivine diorites (plagioclase which has a composition below An_{50}) and magnetite layers. Molyneux (1970) identified 25 magnetite layers in the eastern limb, three below the MML (layers 1 to 3) and another 21 above the MML (layers 1 to 21) (See Figure 1.3 after Harney and von Gruenewaldt, 1995). However, linking all the layers from the eastern, western and northern limb has not reliably been performed as of yet. Magnetite layers range in thickness from 3 cm to 10 m and can generally be followed along strike for significant distances. For example, the MML has a strike of about 120 km in the eastern, 200 km in the western and

100 km in the eastern Bushveld (Reynolds, 1985b). One characteristic of these layers is the sharp footwall contacts (commonly consisting of a very thin anorthosite grading into a leucogabbro) and gradational top contacts with the hangingwall rocks. For the purpose of this study, a 150 m section below the MML was sampled, which included magnetite layer three (Figure 1.3).

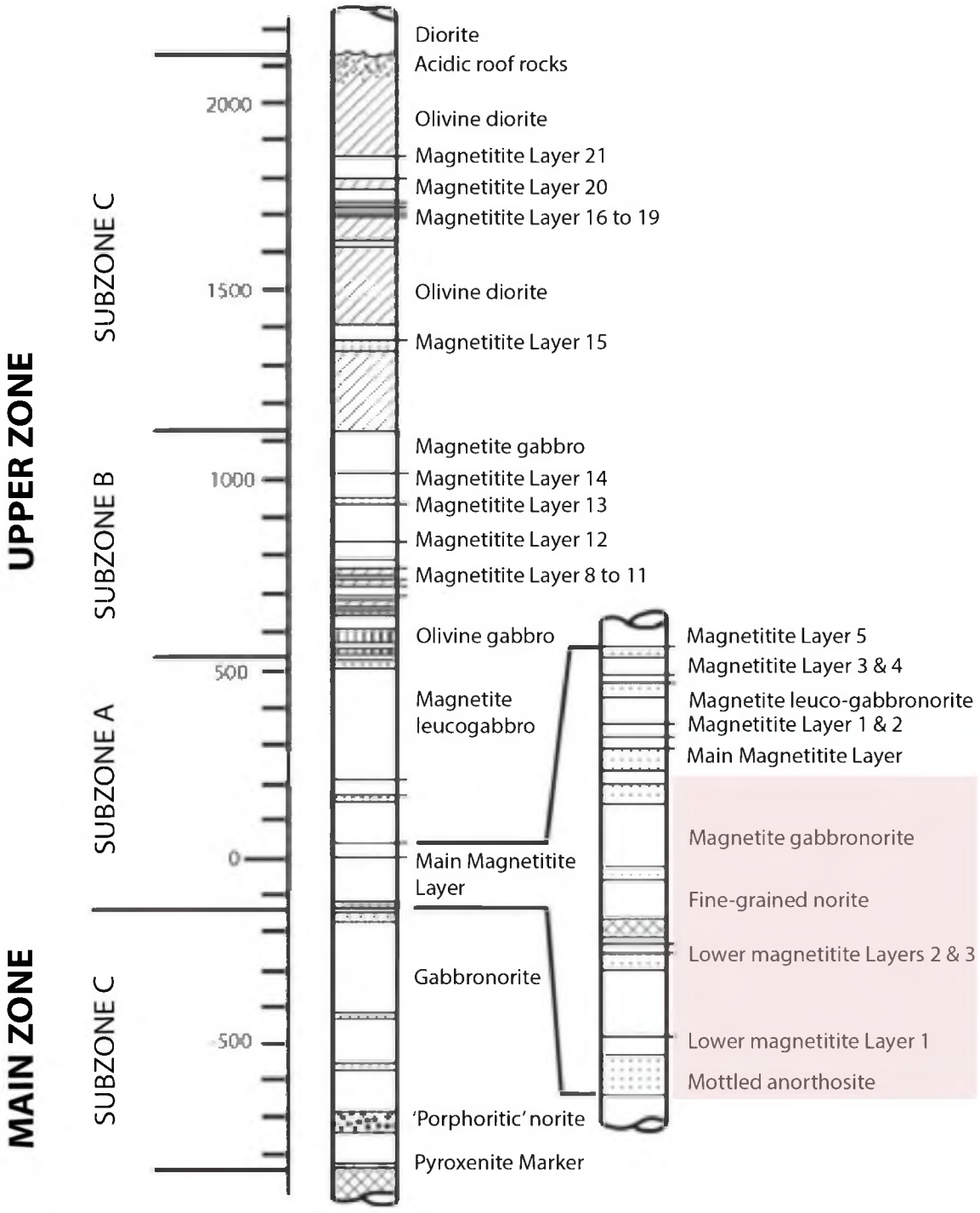

Figure 1.3: Generalised stratigraphic column of the Main and Upper Zone relative to height of the Main Magnetite Layer (MML), adapted after Harney & Von Gruenewaldt (1995). The shaded area represents the study section for this project, 150 m of core stratigraphically below the MML in the basal Upper Zone.

1.3. Formation of Fe-Ti oxide ore layers – review of previous work

There has been a great deal of research done on the formation of Fe-Ti oxide ore layers over the previous few decades. With particular interest to the BIC, much work has been done to unravel the history behind the formation of these deposits e.g. Cawthorn and McCarthy (1980), Reynolds (1985a, 1985b), Klemm *et al.* (1985), Harney and von Gruenewald (1995). The mechanisms proposed in the formation of Fe-Ti oxide ore layers includes: Spontaneous increases in oxygen fugacity (fO_2) (Klemm *et al.* 1985, von Gruenewaldt *et al.* 1985); Liquid immiscibility (Reynolds, 1985a, 1985b; Zhou *et al.* 2005); magma mixing events resulting in the breakdown of densely stratified liquid layers or influxes of a small volume of new magma (Harney and von Gruenewaldt, 1995); settling and sorting (Wager and Brown, 1968) and changes in pressure (Osborn, 1984; Cawthorn and McCarthy, 1980). Each of these mechanisms will be discussed in detail later and have been briefly outlined below.

1.3.1. Increases in fO_2

It has been suggested that an increase in fO_2 may commence magnetite crystallisation (Ulmer, 1969; Klemm *et al.* 1985;). Klemm *et al.* (1985) concluded that the formation of the Fe-Ti oxide ore layers formed in response to an increase in fO_2 at the solid-liquid boundary at the base of the magma chamber. von Gruenewaldt *et al.* (1985) showed that there are distinct differences in exsolution textures between Ti-rich magnetite in magnetite layers compared to those in disseminated magnetite gabbroic host rocks, variations that can be attributed changes in fO_2 during crystallisation and subsolidus oxidation. The distribution of certain major elements (Mg, Al and Si) which are enriched in layer-hosted magnetites compared to disseminated magnetites can be interpreted as spontaneous crystallisation of the magnetite layers under conditions of disequilibrium with the magma. The lower concentrations of V in magnetite layers are also considered to be consistent with higher fO_2 conditions in the magma during crystallisation of magnetite layers in comparison to the disseminated magnetite gabbros. The problem with this model is actually discovering the exact mechanism responsible for the fO_2 increase and how these layers are distributed over such large lateral extents.

1.3.2. Liquid immiscibility

The separation of an evolving magma into Fe-rich and Si-rich immiscible liquids has been proposed by Bateman (1951) for the origin of magnetite layers (Cawthorn & Ashwal, 2009). Reynolds (1985a) proposed that a lengthy period of fractional crystallisation resulted in the concentration of large amounts of Fe, Ti and V in the residual magma, which remained sufficiently dense not to mix with the overlying magma, forming a stagnant layer from which copious amounts of Ti-magnetite may have crystallised. He also suggests that the precipitation of Ti-magnetite depends on the Fe_2O_3/FeO ratio of the liquid, which is also a function of fO_2 in the chamber. However, experimental work on Fe-rich immiscible liquids in basaltic systems (Philpotts and Doyle, 1983; Veksler *et al.* 2007; Jakobsen *et al.* 2005) suggest that these liquids only have approximately 28 wt. % total FeO, values that are significantly lower than those observed in Fe-Ti oxide ore layers. Thus, it implies crystallisation of Ti-magnetite from these liquids would need to be concentrated into layers. Zhou *et al.* (2005) state that the origin of the Fe–Ti–V-rich oxide melts is uncertain, but that they possibly form as immiscible melts within the magma chamber and then settle to the bottom of the chamber, where they accumulate as a layer.

1.3.3. Magma mixing & small pulses of new magma

Harney and von Gruenewaldt (1995) ascribe the formation of Ti-bearing magnetite layers as a response to magma mixing events, which result either from a breakdown of densely stratified liquid layers or an influx of a small volume of new magma. This model is supported by findings of Merkle and von Gruenewaldt (1986) and Harney *et al.* (1990), evidence supported from whole-rock geochemistry. Compositional data of pentlandite and olivine define cycles of differentiation in the upper parts of the UZ in the western Bushveld. The observed reversals in the composition of olivine led these authors to conclude that cycles were produced by magma mixing events. Kruger and Smart (1987) as well as Harney *et al.* (1990, 1996) suggest that a resident magma column may be internally stratified and that the collapse of two or more density stratified liquid layers may result in a such a magma mixing event.

1.3.4. Settling and sorting

The general model of settling and sorting of crystals proposed by Wager and Brown (1968) can be applied to magnetite layers and the cumulate gabbroic host rocks. This mechanism can be applied as many magnetite layers have sharp basal contacts and gradational tops, features indicative of settling and sorting within a magma chamber (Cawthorn *et al.* 2005). However, not all magnetite layers show this feature. Assuming that the magma is saturated in magnetite, pyroxene and plagioclase and that should be the order in which the minerals accumulate from the base upward (Cawthorn and Ashwal, 2009), one can use this as a descriptive feature for a settling and sorting model. However, this is not always the case suggesting a settling and sorting model alone cannot account for the formation of magnetite layers.

1.3.5. Changes in pressure

An increase in pressure is proposed as a mechanism of formation for Fe-Ti oxide ore layers by Cawthorn and McCarthy (1980) as it presents a solid resolution to the lateral consistency of many Fe-Ti oxide ore layers. Osborn (1984) and Lipin (1993) attribute pressure increases in the magma chamber as a triggering mechanism for crystallisation and production of monominerallic chromite seams in the Stillwater Complex (USA). As with an increase in fO_2, this model is attractive is it does not require any changes in magma chemistry particularly with respect to An content of plagioclase across magnetite layers (Cawthorn and Ashwal, 2009). Whether or not the same process can be applied for the formation of magnetitite layers is up to further investigation as mechanisms resulting in such pressure increases are uncertain.

1.4. Scope of the study and objectives

This study has been conducted using a suite of 43 samples collected from the basal UZ, stretching 150 m below the MML to just a few hundred metres above the Pyroxenite Marker. The sample suite includes 5 closely spaced samples taken across magnetite layer 3

(as described by Harney and von Gruenewaldt, 1995), the magnetite layer directly below the MML. The project involves detailing the mineralogical variations in the basal UZ placing particular emphasis on Fe-Ti oxide compositional variations, with specific relationships to silicates and textural features.

The main objectives of this study are:

1) To undergo a petrographic study detailing the silicate and oxide ore mineralogical assemblage as to unravel the petrological evolution and crystallisation history of these rocks
2) To characterise all geochemical and stratigraphic variations throughout the basal parts of the UZ
3) To detail how V_2O_3 concentrations vary between Lithostratigraphic units - from magnetite layers, to disseminated magnetite gabbro, to weathered magnetite gabbro
4) To outline the suggested parent magma compositions to these rocks and compare them to other Fe-enriched magmas, including the Panzhihua intrusion Fe-Ti oxide equivalents, SW China
5) To constrain the genetic process(es) relating to magnetite crystallisation and precipitation
6) To identify the critical factors relating to the recovery of high-V oxide minerals in the sequence

2. Methodology

2.1. Sampling

The basal UZ section was sampled in July 2014 over an interval of 150 m in height (directly below the MML) utilising Rhovan vanadium mine's (Appendix E) diamond drill core collection, Glencore plc owned. Sampling was completed over irregular spatial intervals, accessing areas of interest, whereby a total of 42 samples of quarter-core were collected. A total of 5 samples were taken from the footwall leucogabbro, 5 across a massive magnetite layer, 24 across a disseminated magnetite gabbro zone, 3 across a microgabbro parting and 5 across a weathered magnetite gabbro zone. The 150 m of core was laid out in core trays and logged in full detail across the entire section. A list of all sample names, depths and lithologies are listed below in Table 2.1.

Table 2.2: Heights, ID's and Lithologies of 42 samples taken from Rhovan V mine, 25°28'27.4"S 27°30'10.4"E.

Height (m)	Sample ID	Lithology
6	LS-1	Weathered disseminated magnetite gabbro
8.5	LS-2	Weathered disseminated magnetite gabbro
11.8	LS-3	Weathered disseminated magnetite gabbro
14.1	LS-4	Weathered disseminated magnetite gabbro
20.8	LS-5	Weathered disseminated magnetite gabbro
34.3	WG-6	Disseminated magnetite gabbro
48.1	WG-5	Disseminated magnetite gabbro
63.1	WG-4	Disseminated magnetite gabbro
75.1	WG-3	Disseminated magnetite gabbro
89.2	WG-2	Disseminated magnetite gabbro
102.1	WG-1	Disseminated magnetite gabbro
111	OHSZ-7	Disseminated magnetite gabbro
112	OHSZ-6	Disseminated magnetite gabbro
118.2	OHSZ-5	Disseminated magnetite gabbro
123.8	OHSZ-4	Disseminated magnetite gabbro
128.5	OHSZ-3	Disseminated magnetite gabbro
130.8	OHSZ-2	Disseminated magnetite gabbro
131.8	OHSZ-1	Disseminated magnetite gabbro

134.5	OBSZ-6	Disseminated magnetite gabbro
136.7	OBSZ-5	Disseminated magnetite gabbro
138.9	OBSZ-4	Disseminated magnetite gabbro
139.9	OBSZ-3	Disseminated magnetite gabbro
141.1	OBSZ-2	Disseminated magnetite gabbro
142.1	OBSZ-1	Disseminated magnetite gabbro
142.5	P-1	Microgabbronorite
143.3	P-2	Microgabbronorite
143.8	P-3	Microgabbronorite
145.1	OFSZ-5	Disseminated magnetite gabbro
145.5	OFSZ-4	Disseminated magnetite gabbro
146	OFSZ-3	Disseminated magnetite gabbro
146.2	OFSZ-2	Disseminated magnetite gabbro
147	OFSZ-1	Disseminated magnetite gabbro
147.25	BS-5	Layer magnetitite
147.4	BS-4	Layer magnetitite
147.6	BS-3	Layer magnetitite
147.8	BS-2	Layer magnetitite
148	BS-1	Layer magnetitite
148.1	An-5	Anorthosite footwall
148.5	An-4	Leucogabbro
149	An-3	Leucogabbro
149.5	An-2	Leucogabbro
150	An-1	Leucogabbro

2.2. Sample preparation

2.2.1. Thin section preparation and crushing

A total of 37 representative samples were cut and unpolished thin sections were prepared for transmitted/reflected light microscopy. Of these, 12 sections were polished and carbon coated for Electron Probe Micro analysis (EPMA). All 42 samples were subsequently crushed in a manganese steel (2.00 % Mn, 0.90 % C, 0.5 % P, 0.2 % Si) ring and puck shatterbox crusher using a Herzog swing mill. The samples were crushed for approximately 3 minutes until desired grain size (<400 mesh) was obtained. After each individual sample was

crushed, the rings of the crusher were washed using sunlight soap and water, followed by drying with acetone and paper towels. If the rings were not thouroughly clean, the process was repeated. In between runs, pure quartzite was crushed. This process was perfromed to elimate the possibility of contamination of the subsequent sample crushed. The crushed samples were then placed into marked sample bags and vials for the preparation of powder pellets.

2.2.2. Powder pellet preparation

42 powder pellets were prepared for trace element analysis using X-ray Fluorescence Spectrometry (XRF). The following procedure was performed:

- Approximately 5 grams of powder from each sample was measured out on the weighing scale;
- The powder was then placed in the pestle and mortar crusher;
- Three drops of Mowial (the binding agent) was then added to the sample and mixed rigorously using in the pestle and mortar crusher;
- Once the powder had reached the desired consistency, it was removed from the pestal and mortor crusher, and placed within the metal cylinder;
- The powder was gently pressed into the standard pellet shape using the plastic press, before approximately 5 ml of Boric acid was added in the pressing vial;
- The metal stomper was then placed on top of the powder and Boric acid before being placed under the press;
- Once in the press, the powder was pressed to a weight of 10 tons, then released slowly;
- The powder pellet was then removed from the press, marked on the underside with a permanent marker, laid in a sample tray and placed in a covered sample box to avoid any contamination of the analytical surface

2.3. Analytical techniques

2.3.1. Petrography

All microscopic observations (mineral identification, textural relationships and modal abundances) were performed using a Leica transmitted light microscope. Photomicrographs were taken using the Leica Application Suite (LAS) under 2.5 X or 10 X magnification, as appropriate.

Mineral modal abundances were calculated using the James Swift point count analyser which attached to the light microscope stage. All counts were set at 250 points per thin section due to the coarse-grained nature of these plutonic rocks. Modal abundances can be seen presented in Figure 4.9.

2.3.2. Trace and Rare Earth Element (REE) geochemistry

Trace elements (Co, Mn, Cr, V, Zn, Cu, Ni, Mo, Nb, Zr, Y, Sr, U, Rb, Th and Pb) for the entire sample set were analysed using a Philips PW1480 wave-length dispersive X-ray Fluorescence spectrometer at the Department of Geology, Rhodes University. It is important to note that V concentrations in these rocks are substantially higher than those available in standards used for calibration, such that the calibration for V was extrapolated beyond its ideal range to determine V in many of the magnetite-rich samples. Therefore, results with V concentrations at >9000 ppm should be viewed as semi-quantitative.

20 duplicate samples were also sent to the Geoscience Laboratories, Sudbury, Canada to run for trace element abundances using a different method, to make comparisons in element concentrations using different methods. Trace elements were analysed using Inductively-Coupled Plasma Mass Spectrometry (ICP-MS) after acid digestion. REE concentrations were analysed using the same method described.

2.3.3. Major element geochemistry

20 representative samples were analysed via XRF (method code XRF-M01) for the major elements Al_2O_3, BaO, CaO, Cr_2O_3, Fe_2O_3, K_2O, MgO, MnO, Na_2O, P_2O_5, SiO_2 and TiO_2 at the Geoscience Laboratories, Sudbury, Canada. It is important to note that TiO_2 greater than 8 wt. % are beyond the scope of the method used, rendering the data semi-quantitative. The interference on BaO is also insufficiently corrected (Remakis, pers comm. 2015).

2.3.4. EPMA

EMPA data acquisition was performed at the Department of Geology, Rhodes University on a JEOL JXA-8230 Superprobe, using 4 WD spectrometers. The analytical conditions were as follows: probe current 20 nA, acceleration voltage 15 kV, counting time 10 seconds on peak and 5 seconds on background, beam size spot <1 micron. Natural standards were used for measuring the characteristic X-rays. The ZAF matrix correction method was employed for quantification. Textural analysis (and backscatter imagery), WDS analysis, elemental distribution maps as well as quantitative mineralogical identification was performed for 12 chosen representative samples (AN-5, BS-1, BS-2, BS-4, BS-5, OFSZ-3, OFSZ-5, OBSZ-6, P-1, WG-4, LS-1 and LS-5). Over 300 oxide and silicate points were analysed. Cation/anion numbers, molar proportions as well as mineral endmembers were calculated for all analysed plagioclase and pyroxene grains. Full element analytical standards, detection limits as well as all raw and calculated EPMA data may be found in Appendices A and C.

3. Macroscopy

3.1. Lithostratigraphic units

The 150 m of sampled core (Figure 3.1) comprises essentially of five main rock units, namely: Anorthosite footwall, magnetitite layer, fresh disseminated magnetite gabbro, weathered and altered disseminated magnetite gabbro, and microgabbro.

Anorthosite

Anorthosite occurs as the footwall unit to a magnetite layer as a discrete, <0.5 m thick layer of coarse-grained plagioclase (>90 %) and minor interstitial clinopyroxene and accessory Fe-oxides. This thin layer grades into a more conventional gabbro with increasing depth, displaying ± 60-70 % plagioclase and 20-30 % clinopyroxene and accessory Fe-oxides (magnetite and ilmenite) as the mineral assemblage. Plagioclase grain size varies from 2 to 3 mm while clinopyroxene grains range from 1 to 2 mm in size.

Magnetite layer

This ± 0.8 m thick layer consists of >90 % magnetite at the base, > 80 % magnetite in the middle of the layer and grades into ± 50 % magnetite at the top of the layer. It consists primarily of coarse-grained magnetite with trapped sub-anhedral plagioclase and clinopyroxene. The basal contact with the footwall anorthosite is not the typical knife-sharp contact characteristic of the base of an oxide-rich layer but is rather an irregular or somewhat gradational contact (Figure 3.2a), much like the upper contact into the disseminated magnetite gabbro.

Fresh disseminated magnetite gabbro

This lithology makes up the bulk of the sampled section and typically comprises of roughly 25-50 % medium to coarse-grained, interstitial magnetite, with well-developed plagioclase laths and lesser anhedral clinopyroxene as the dominant silicate phases (as well as minor orthopyroxene). Magnetite (typically anhedral) and plagioclase grains typically range from 1 to 3 mm in size (Figure 3.3a).

Weathered disseminated magnetite gabbro

In comparison to the fresh disseminated magnetite gabbro, the near-surface weathering zone consists of coarse-grained, altered silicates (predominantly plagioclase altered to clay minerals) and magnetite with hematisation around grain boundaries (Figure 3.3b). Magnetite remains relatively fresh in comparison to the silicates, which show total alteration to clay minerals in certain sections (Figure 3.3c).

Microgabbro

This ± 1 m section of fine-grained gabbroic rock occurs as a parting between disseminated magnetite gabbro approximately 5-6 m above the magnetite layer (see Figure 3.1). It consists predominantly of anhedral plagioclase (± 50 %) and relatively equal modal proportions of clinopyroxene and orthopyroxene, with accessory Fe-oxides making up the remainder of the rock. Grain size varies from 0.1 to 0.5 mm at most.

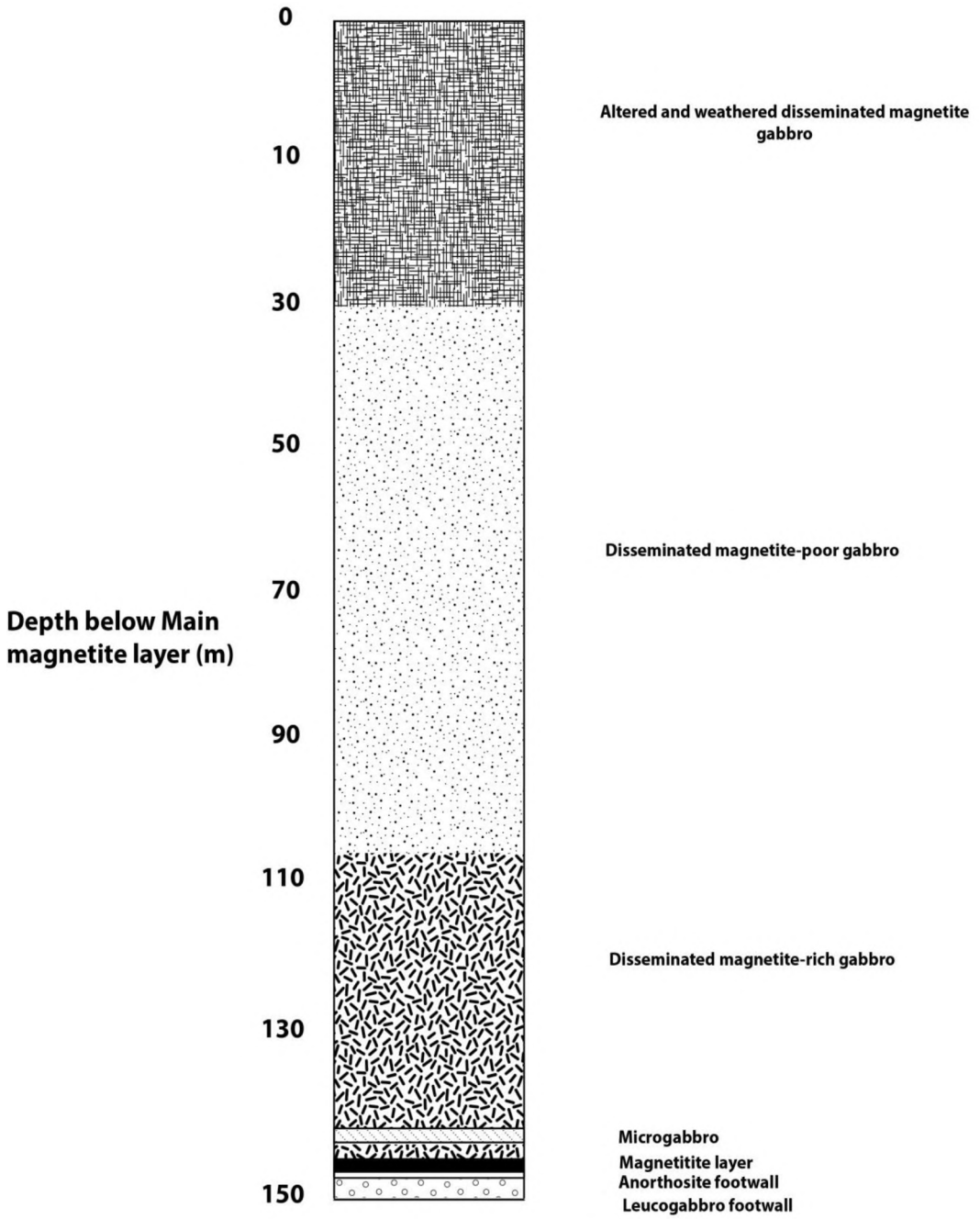

Figure 3.1: Stratigraphic core log depicting the 150 m of core sampled from Rhovan V mine, basal Upper Zone, western Bushveld Igneous Complex. Location 25°28'27.4''S 27°30'10.4''E.

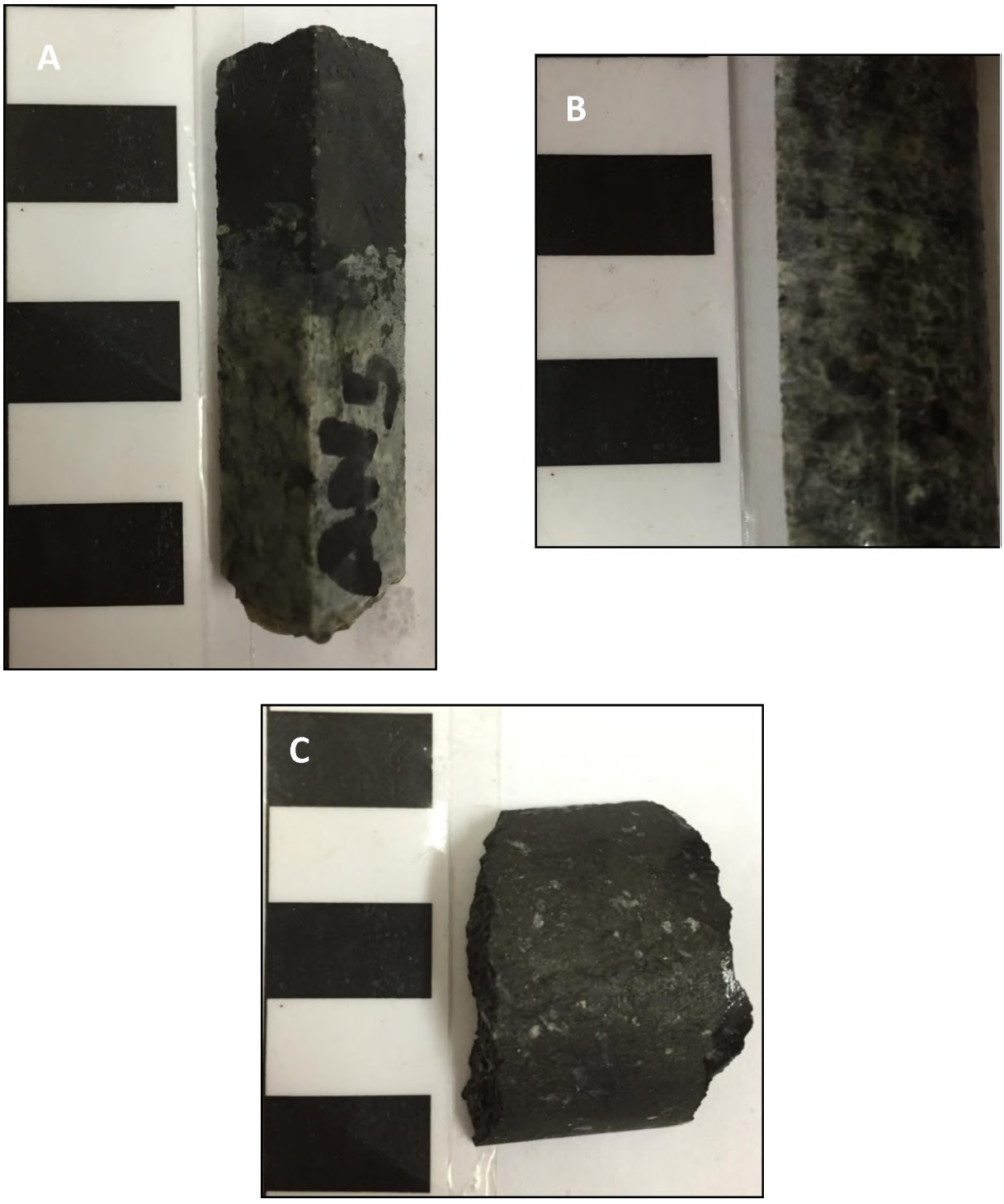

Figure 3.2: (a) Irregular footwall anorthosite contact with a magnetite layer. These contacts are usually sharp with gradational upper contacts to the hangingwall (b) Typical footwall leucogabbro (c) Massive magnetite layer with anhedral silicate inclusions. Scale bar = 1 cm

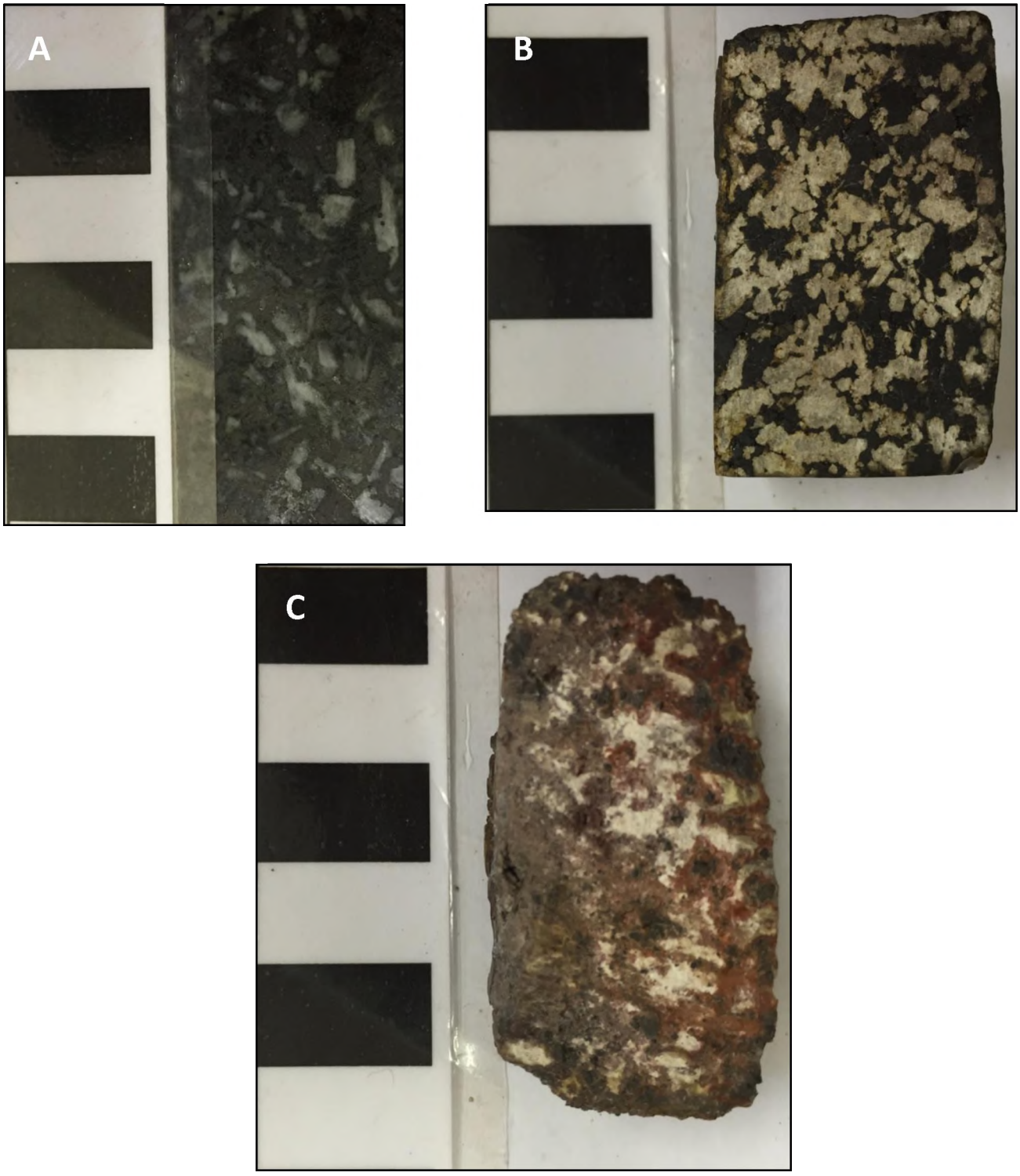

Figure 3.3: (a) Fresh disseminated magnetite gabbro with distinct lath-shaped plagioclase (b) Slightly weathered disseminated magnetite gabbro. Note magnetite remains relatively fresh while silicates have been altered (c) Highly weathered disseminated magnetite gabbro. Note high degree of hematisation surrounding magnetite grains while silicates have been significantly altered to clay minerals. Scale bar = 1 cm

4. Petrography

4.1. Fe-Ti oxide petrography

4.1.1. Layer-hosted magnetites

The basal magnetite layers consists of >90 % magnetite at the base of the layer, grading to ± 50 % at the top. Magnetite is predominantly coarse-grained, with inclusions of fine-grained silicates near the base (Figure 4.1a) and coarser-grained lath-shaped plagioclase near the top (Figure 4.1b,c). Ilmenite only occurs as an oxidation exsolution feature in magnetite (Figure 4.1.d).

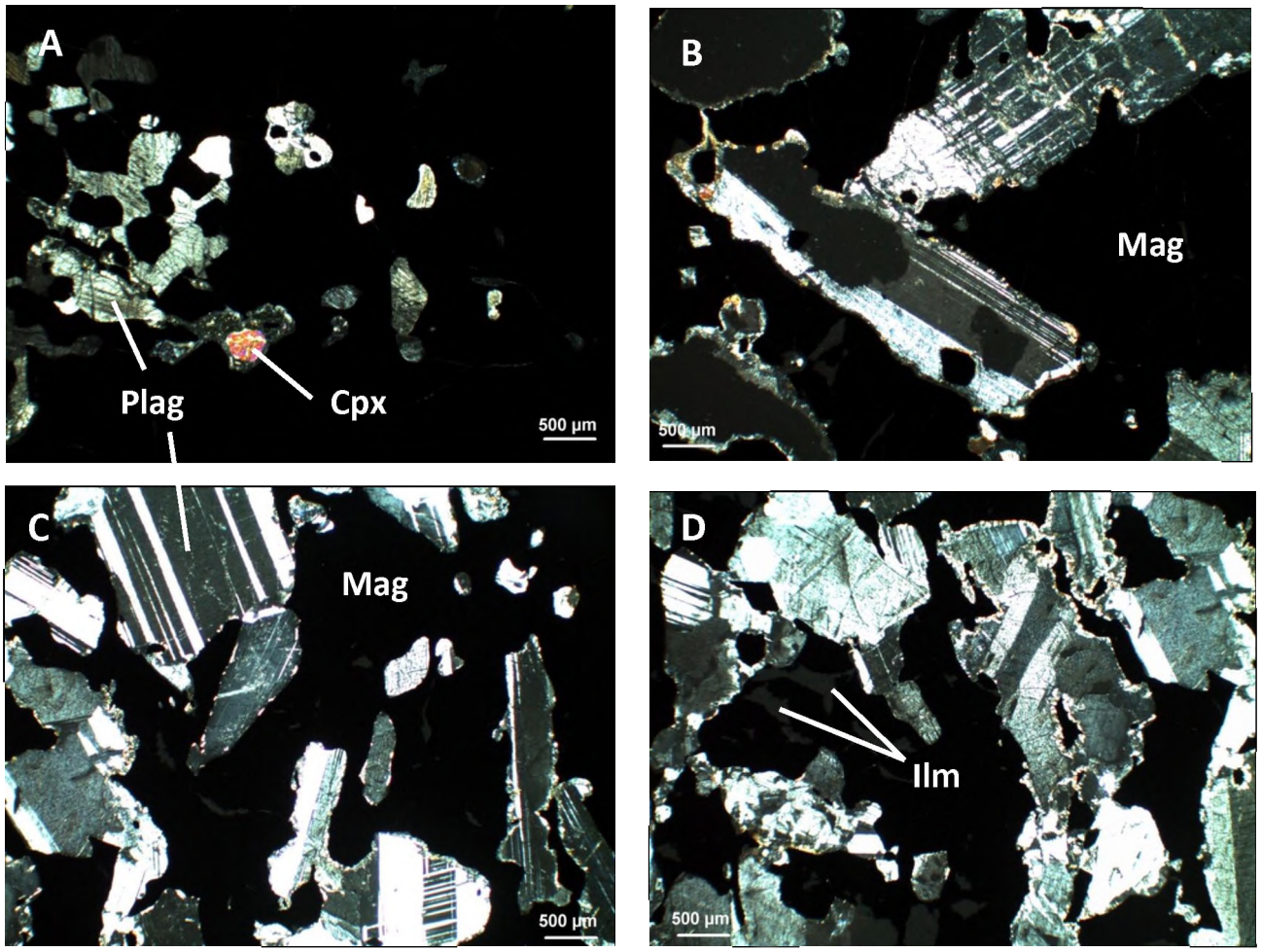

Figure 4.1: Transmitted Xpl images showing layer magnetites with varying modal abundances of silicates. The modal abundance of silicates increases with height within a layer magnetite (i.e. from a-d). At the base of the layer the silicates consist mostly of finer-grained clinopyroxene while coarser-grained plagioclase dominates as the silicate phase with increasing height through the magnetite layer.

Magnetite content varies from 15-40 % modal abundance, consisting primarily of medium-grained, anhedral disseminated magnetite hosted in gabbro. Plagioclase is typically medium to coarse-grained, lath-shaped crystals varying between 40-50 % modal abundance. Clinopyroxene consists of medium-coarse grained, subhedral crystals displaying distinct exsolution lamellae (Figure 4.2b) while orthopyroxene occurs as interstitial, anhedral grains. Modal abundances of clinopyroxene and orthopyroxene vary between 10-30 % and 0-20 % respectively for this lithological unit.

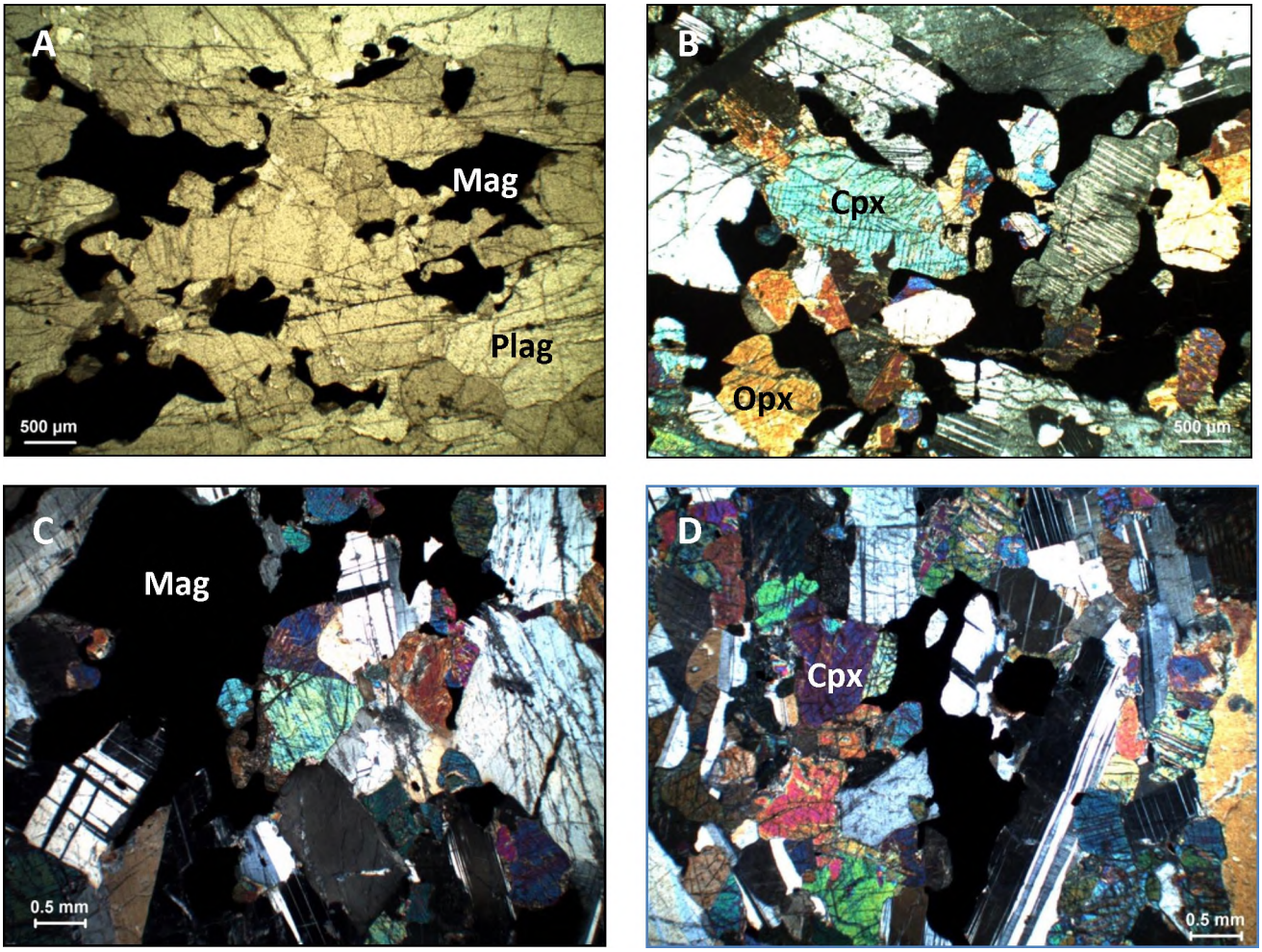

Figure 4.2: Transmitted light images showing disseminated magnetite gabbros with varying modal abundances of oxide and silicate mineralogy Note the anhedral, intimately intergrown nature of the magnetite with the plagioclase and clinopyroxene in all samples. (a) sample OFSZ in ppl (b) sample OFSZ-1 in xpl, (c) sample OHSZ-1 (d) sample OBSZ-5.

4.1.3. Weathered disseminated magnetite gabbros

Near-surface weathering results in primarily silicates (plagioclase and clinopyroxene) being broken-down into clay minerals (Figure 4.3a-c). Magnetite typically remains fresh due to its more resistant nature; however it is typically hematised around grain boundary margins (Figure 4.3d).

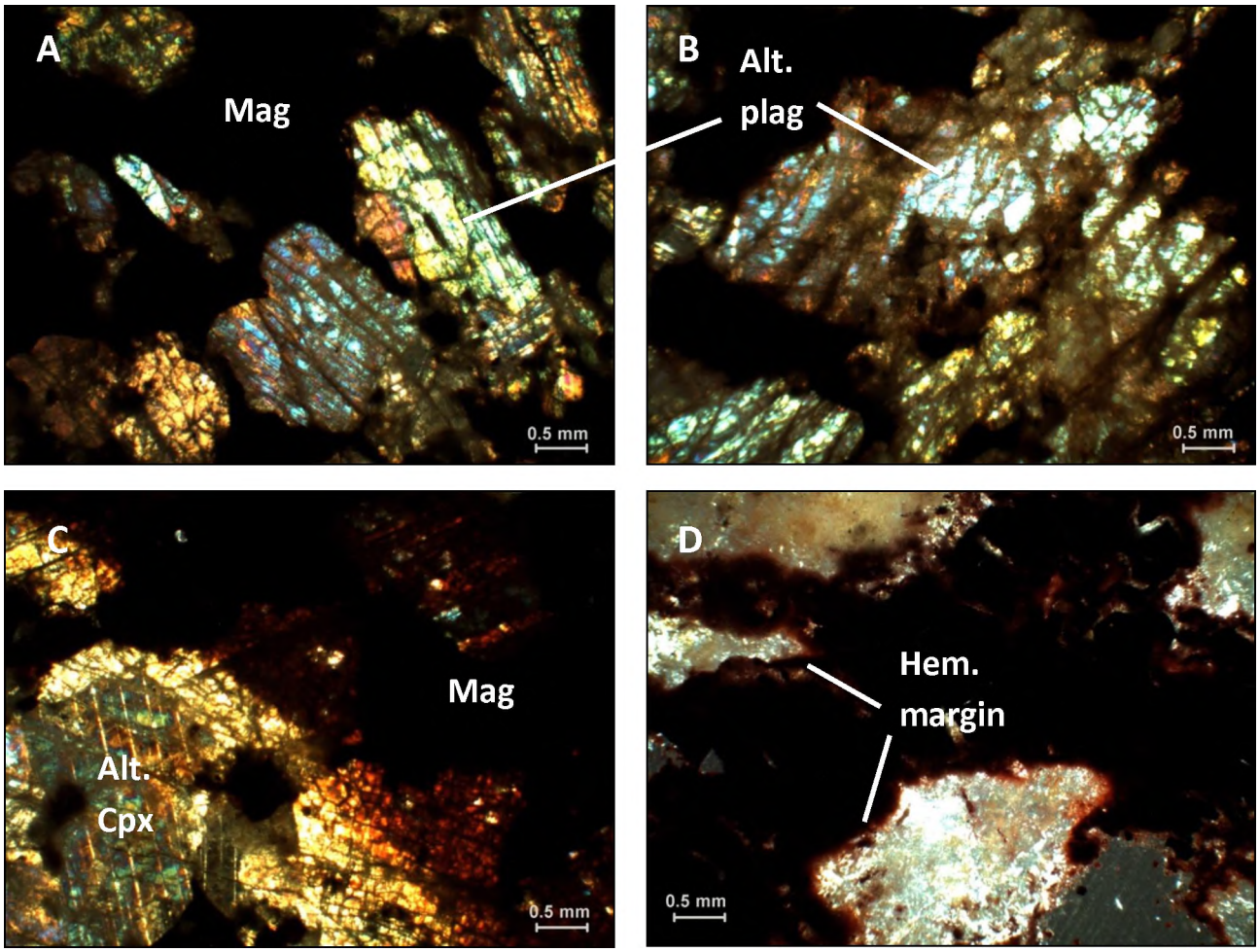

Figure 4.3: Xpl images showing weathering of plagioclase (a,b) and cpx (c) to clay minerals. Magnetite remains fresh and relatively unaffected by the weathering process besides some minor hematisation around grain boundary margins (as visible in d).

4.2. Fe-Ti oxides and associated exsolution features

Ulvöspinel exsolutions are present in all the magnetite layer samples analysed (Figure 4.4 a-d) as the typical cloth texture with exsolution lamellae intersecting each other at right angles (Figure 4.4a-c). The cloth texture is a network of micrometre scale lamellae of ulvöspinel only visible under high magnification (400x or more). Granular ilmenite

exsolution also occurs as discrete grains in magnetite (Figure 4.4e-h). These can be seen throughout magnetite layer and disseminated magnetite samples.

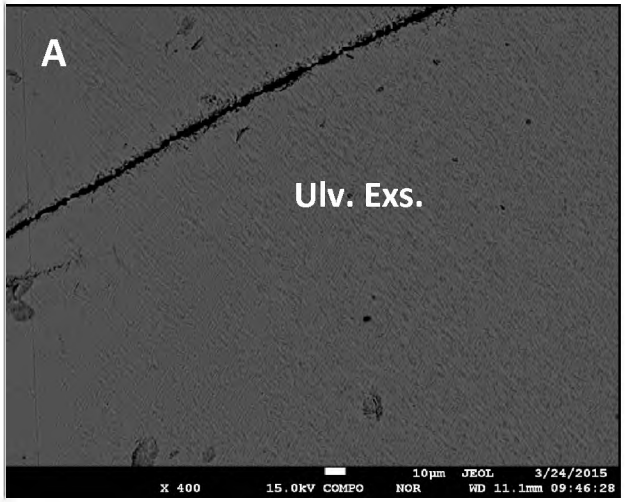

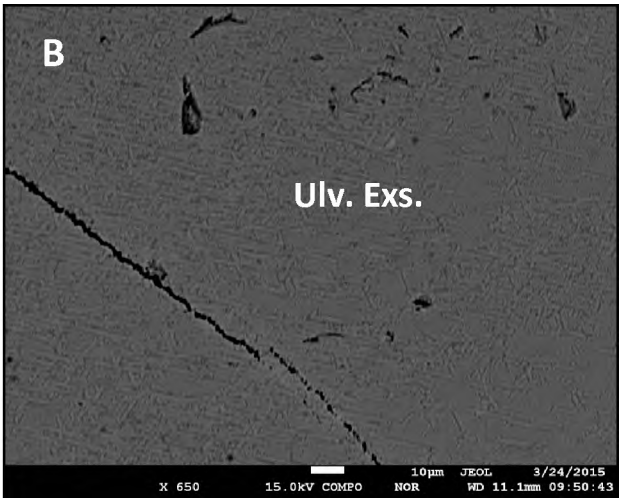

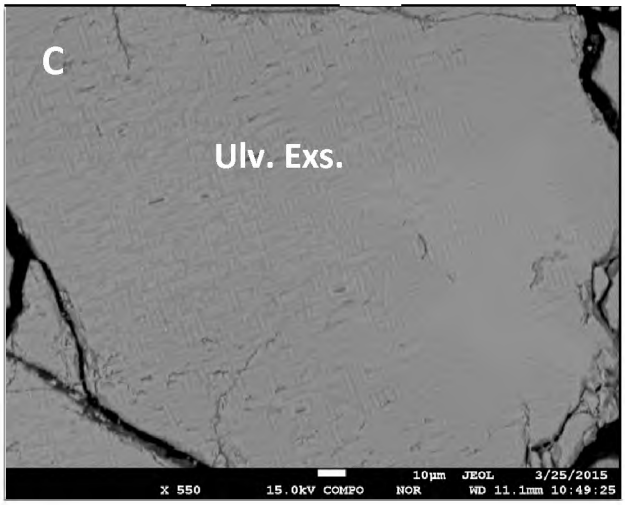

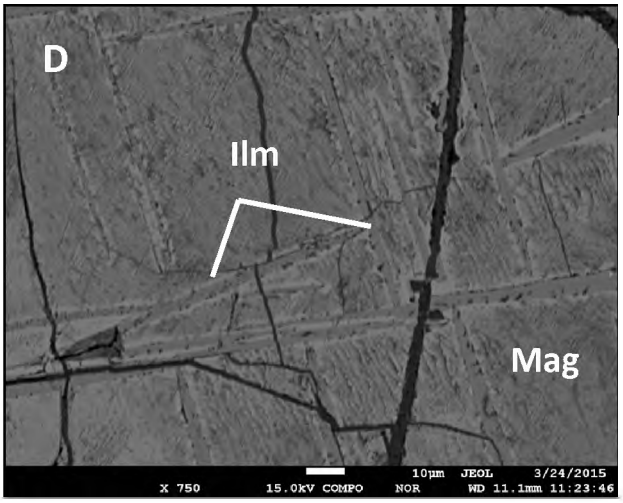

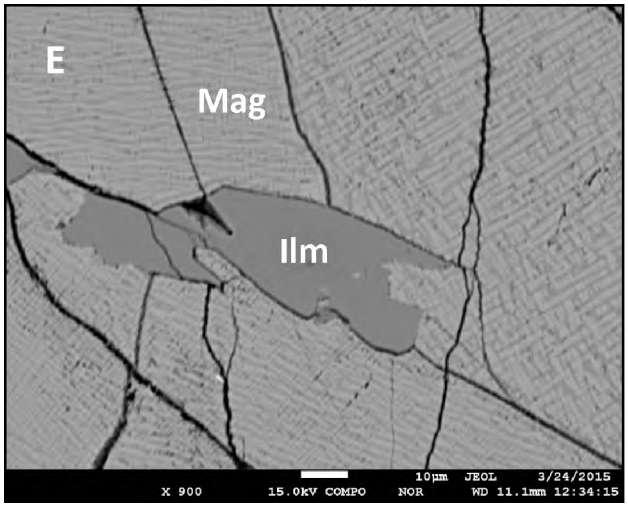

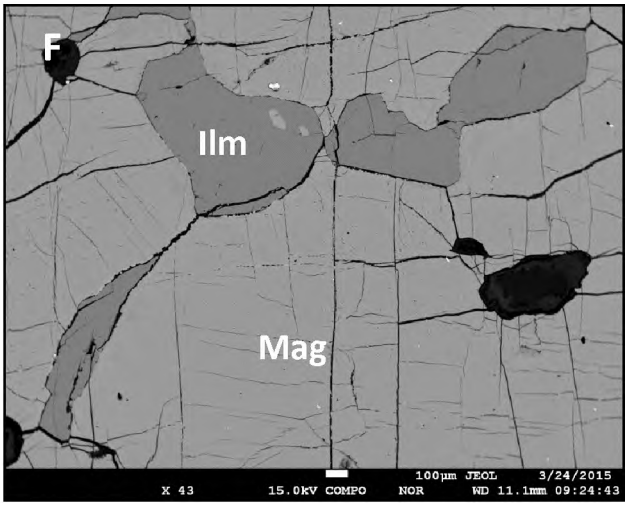

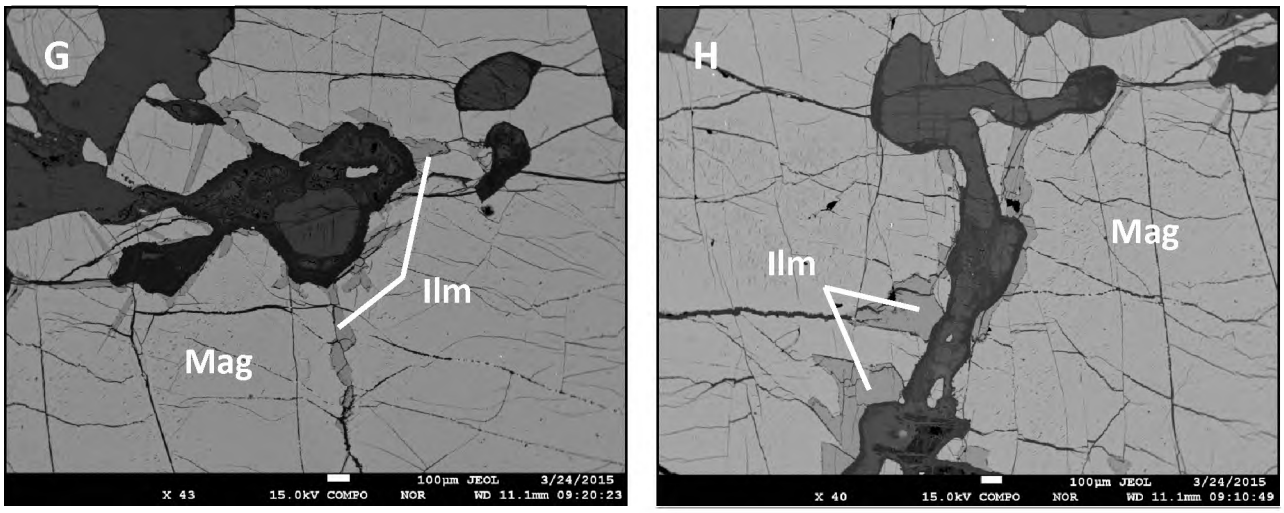

Figure 4.4: BSE images showing exsolution features associated with Ti-rich magnetites. (a-c) Micro-scaled cloth-textured ulvospinel in magnetite (d) trellis ilmentite and associated ulvospinel cloth-texture in magneite (e-f) discrete grains of ilmenite in magnetite. These occur as "internal" (e,f) and "external" granule exsolutions (g,h) either within magnetite or bordering magnetite grains.

4.3. Silicate petrography

4.3.1. Gabbroic mineralogy

Silicate mineralogy is typical of a gabbroic composition consisting primarily of coarse-grained, plagioclase, clinopyroxene (often with distinct exsolution lamellae) and minor interstitial orthopyroxene as the major silicate constituents (Figure 4.5a-c).

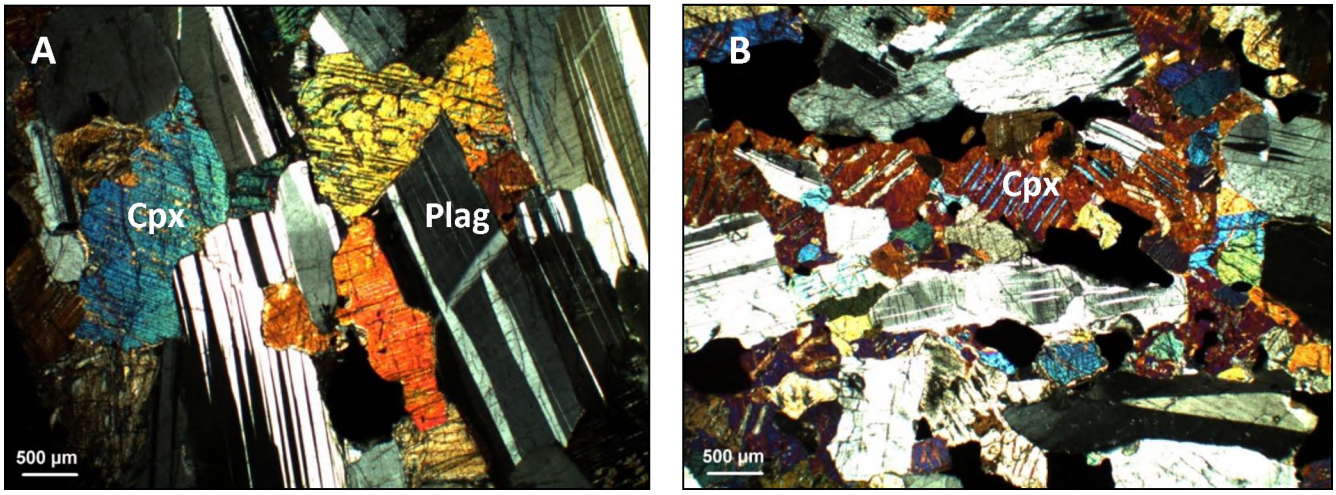

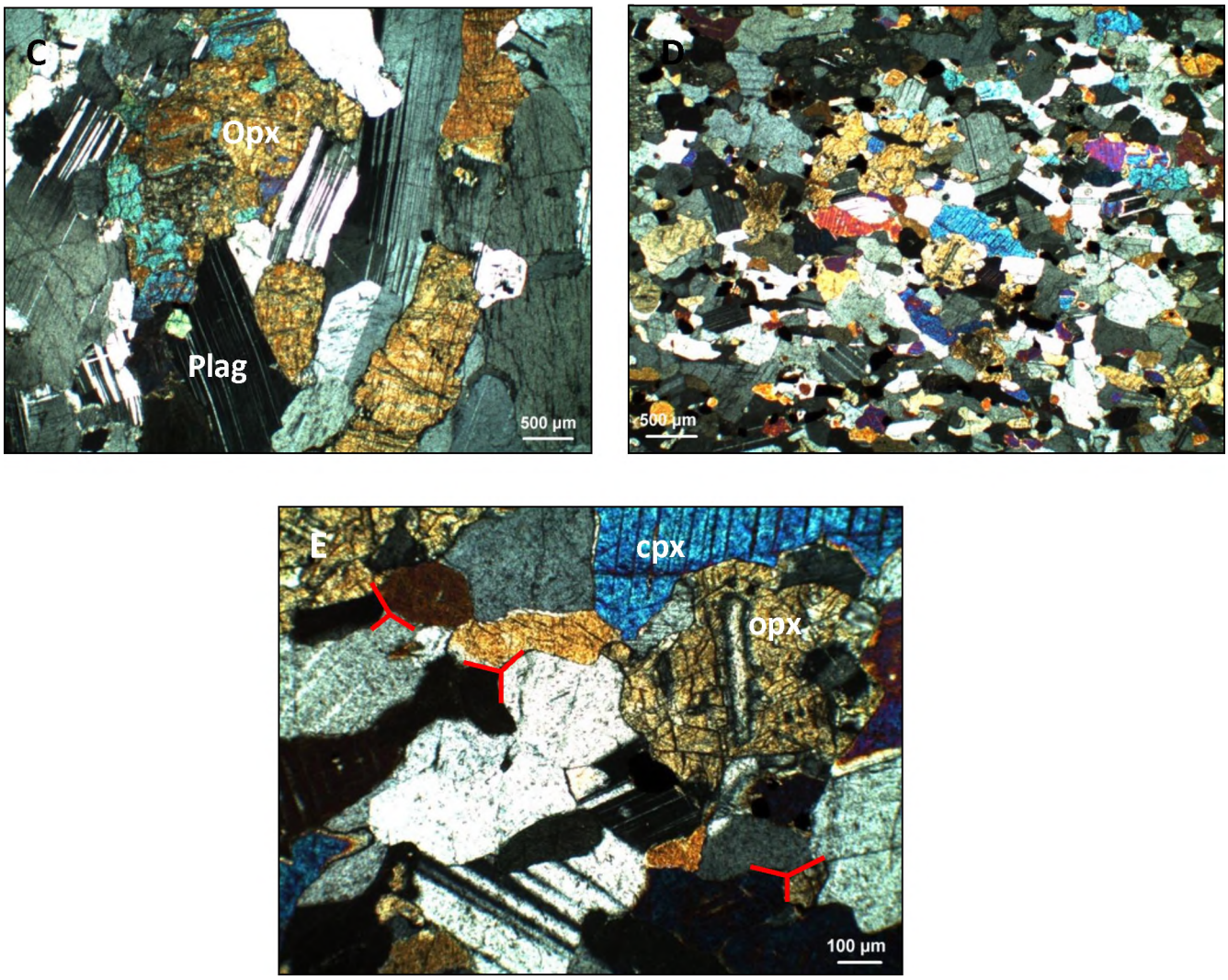

Figure 4.5: Xpl images showing (a) Typical gabbro with euhedral plagioclase laths, cpx and interstitial opx and Fe-Ti oxides (b) Cpx exsolution lamellae in opx (c) Plagioclase laths with cpx and opx with interstital Fe-Ti oxides (d) Microgabbro with anhedral, fine-grained plagioclase, cpx, opx and accessory oxides (e) triple-grain junctions present in microgabbro.

4.4. Reaction rim and coronitic textures

Reaction rim and coronitic mineralogies are primarily in the form of silicate minerals. Fine-grained symplectite intergrowths of orthopyroxene and plagioclase occur at the interface between magnetite and plagioclase grain boundaries (Figure 4.6b,d,e). These are generally well-developed and continuous. Some magnetite grains, particularly in very coarse-grained

sections, display distinct coronas of chlorite (Figure 4.6c,d) capping a symplectite (between magnetite and plagioclase) or sandwiched between a symplectite.

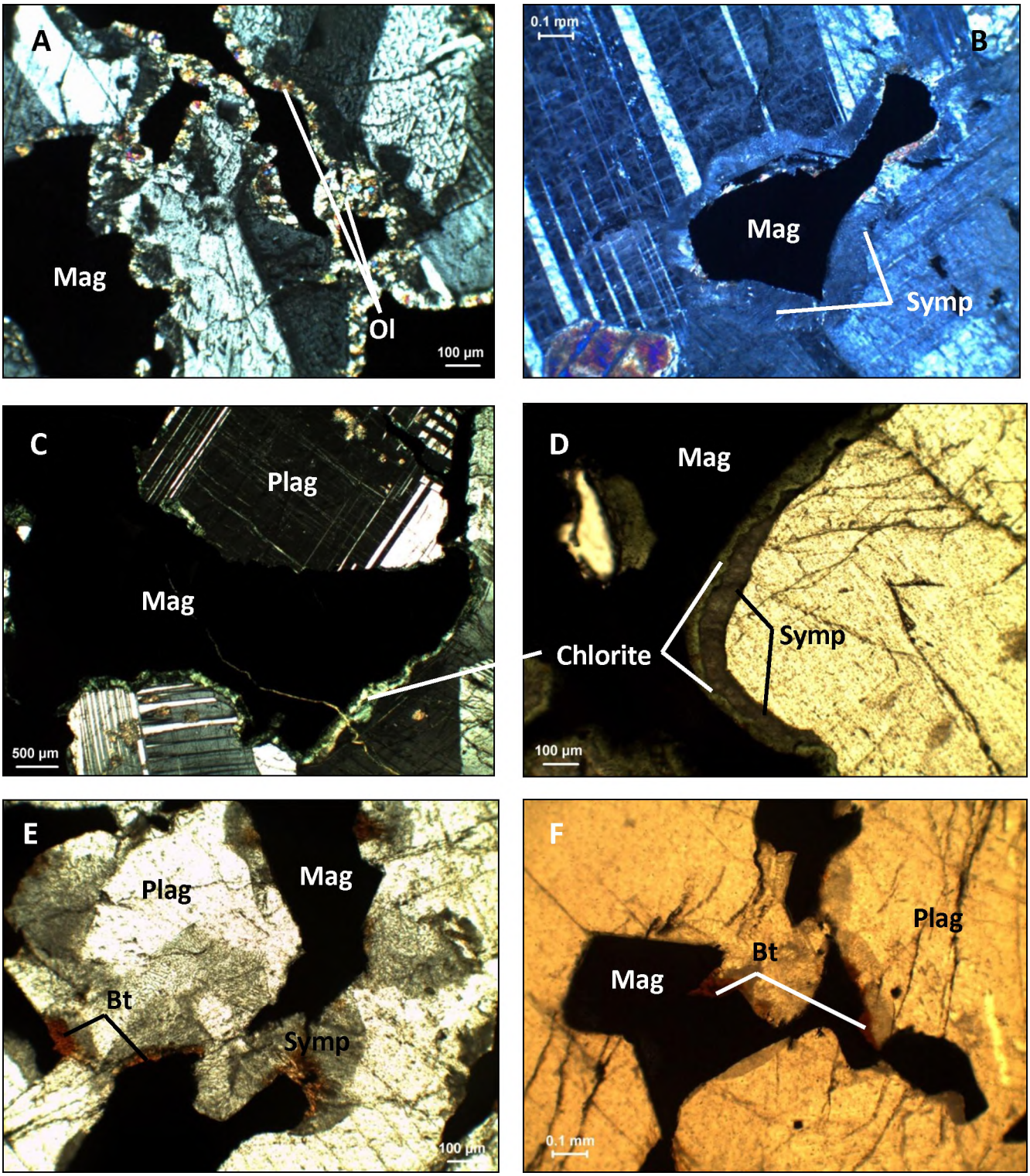

Figure 4.6: (a) Xpl image showing a complex coronitic rim of fine-grained olivine between magnetite and plagioclase. Note this reaction is only seen the magnetite layer and not within the disseminated sections (b) Xpl image showing a symplectite intergrowth of plagioclase and opx between magnetite and plagioclase (c) Xpl image (d) Ppl image showing a complex corona of a plagioclase and opx symplectite intergrowth with a chlorite rim between magnetite and plagioclase (e&f) Ppl images showing discontinuous biotite rims between magnetite and opx + plagioclase symplectites.

Magnetite layer samples also display coronas of fine-grained olivine between magnetite and plagioclase. Discontinuous rims of biotite (not as ubiquitous as symplectites) also occur between magnetite and symplectites in gabbroic sections (Figure 4.6e,f).

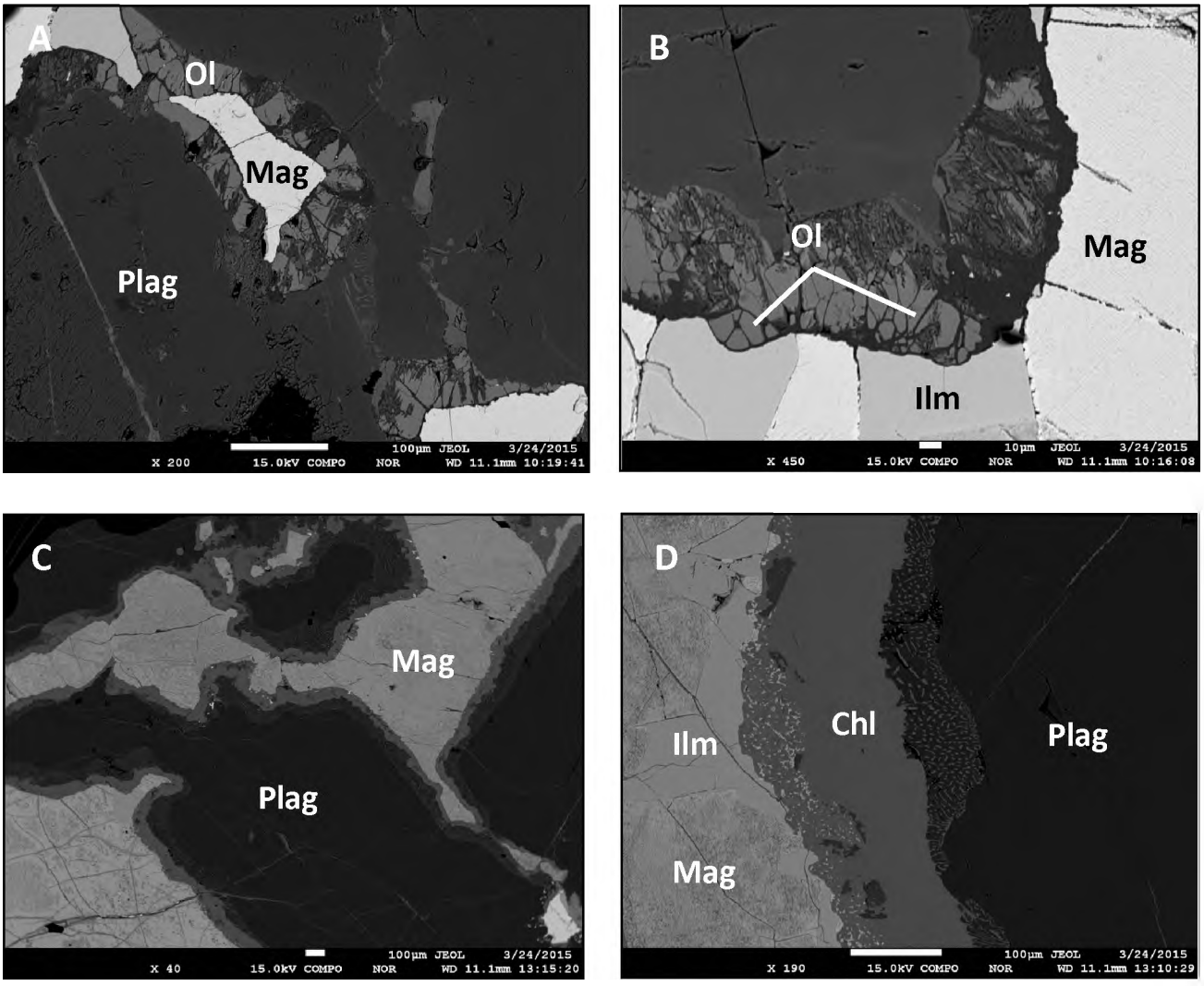

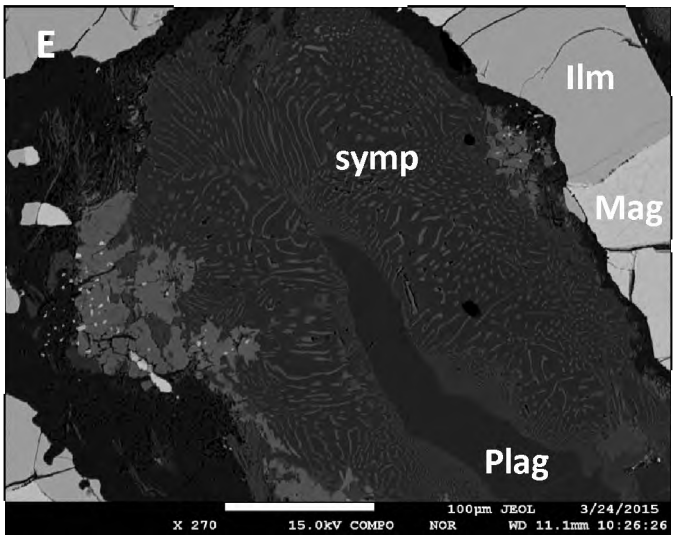

Figure 4.7: BSE images showing (a&b) fine-grained rim of olivine between magnetite and plagioclase. Note the triple junction boundaries between grains (c&d) Complex corona texture of a plagioclase and opx symplectite intergrowth with a chlorite rim between plagioclase and magnetite (d) Fine-grained plagioclase and opx symplectite intergrowth between plagioclase and magnetite.

4.5. Sulphides

Very fine-grained disseminated pyrite and chalcopyrite occur within gabbroic sections, primarily as inclusions in plagioclase (Figure 4.8b,c) and clinopyroxene. Within the microgabbro, these occur as aggregates of grains or 'blebs' within the silicates. Occasionally these grains show compositional zoning from pyrite cores to chalcopyrite rims.

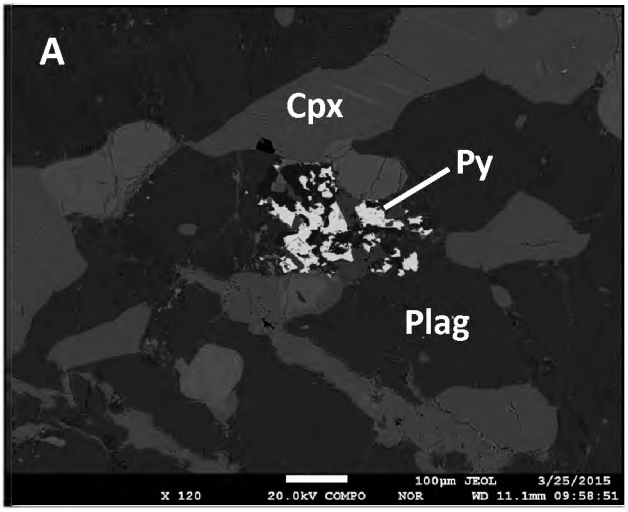

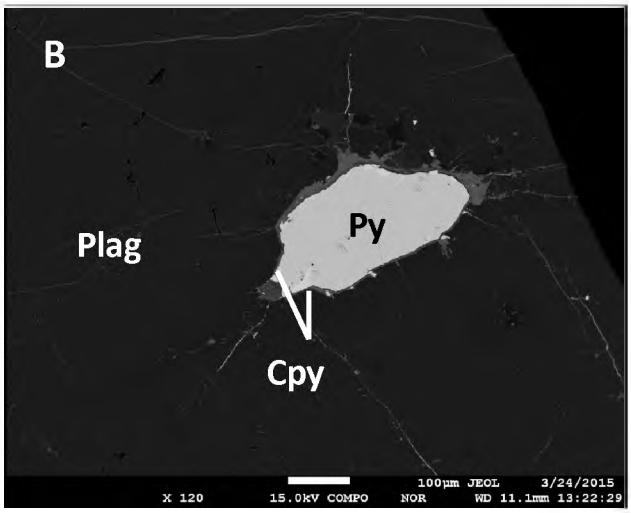

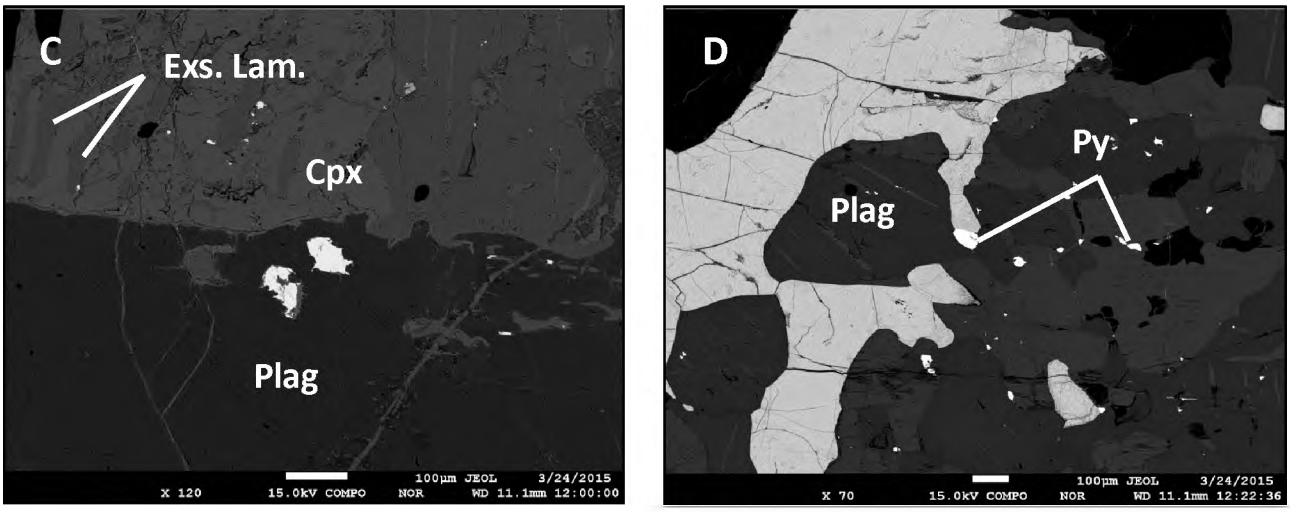

Figure 4.8: BSE images showing (a) Microgabbro with sulphide aggregates or 'blebs' hosted in plagioclase (b) Zoned sulphide with a pyrite core and a chalcopyrite rim, hosted in plagioclase (c&d) Disseminated sulphides hosted in plagioclase and cpx.

4.6. Modal abundances

Figure 4.9 displays the modal abundances of silicates (plagioclase, clinopyroxene, orthopyroxene and coronitic/reaction rim minerals displayed as 'other') and oxides (magnetite and ilmenite) from representative samples throughout the sampled section. The highest abundance of oxides occur at the base of the magnetite layer then decreasing upwards and varying between 10-50 % in the disseminated magnetite gabbros. Plagioclase abundances are highest within the thin footwall anorthosite (> 90 %) and varies between 20-60 % within the magnetite gabbros. Orthopyroxene (0-20 %) and clinopyroxene (10-30 %) abundances are generally lower than plagioclase throughout the gabbroic sections and always less than 50 % modal proportion.

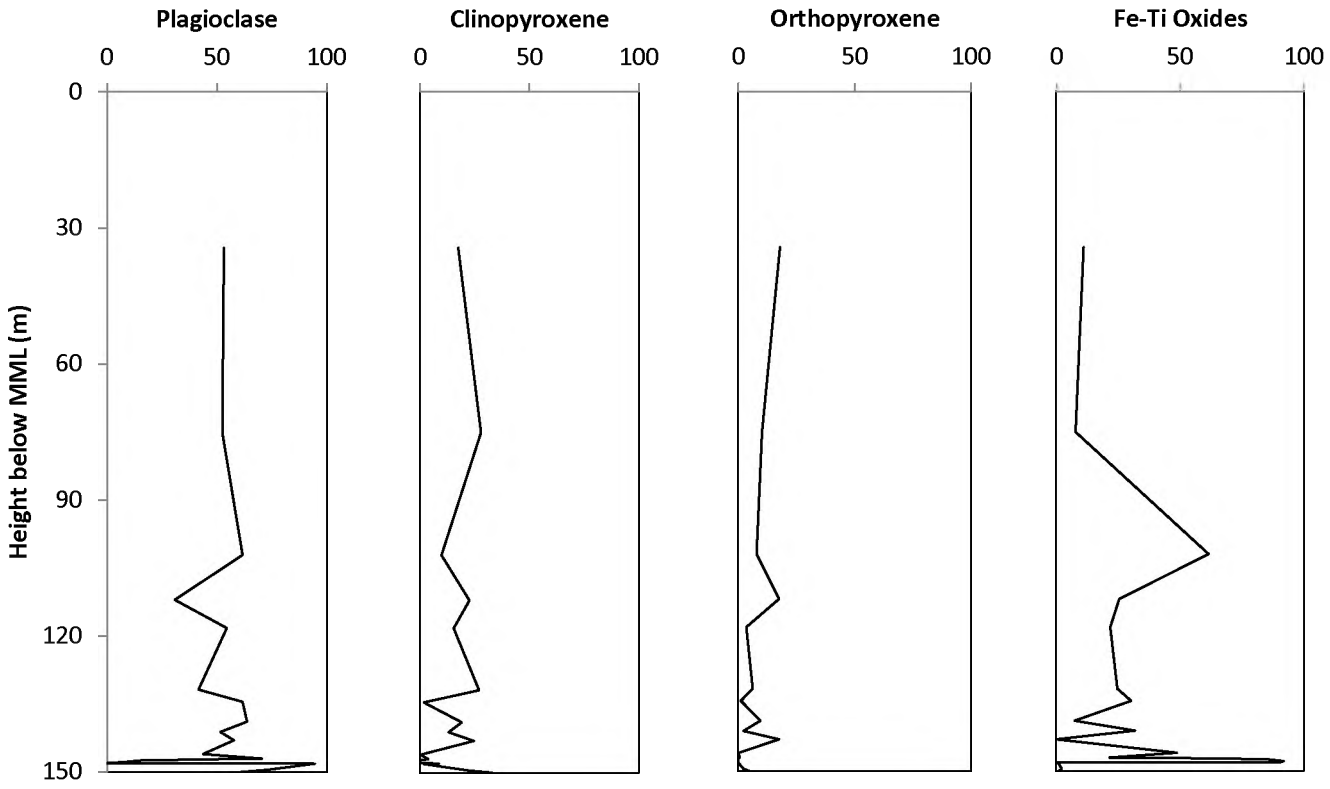

Figure 4.9: Silicate (plagioclase, clinopyroxene and orthopyroxene) and oxide (magnetite and ilmenite combined) modal abundances for the 150 m sampled section. Note, the top 30 m of the borehole consists of highly-weathered rocks and hence most silicates converted to clay minerals rendering modal abundances impossible to determine.

5. Mineral chemistry

5.1. Plagioclase

Mean An % for all measured plagioclase samples is An_{69} with the lowest and highest values being An_{60} and An_{77} respectively. Figure 5.1 displays the mean An % for plagioclase samples analysed across the sampled section, including data from Tegner *et al.* (2006) for the MML and Pyroxenite Marker. There is no obvious variation in An % of plagioclase cores and rims (as detailed by line analysis on a number of plagioclase grains) with homogenous, unzoned laths the norm. Mean plagioclase An % values are slightly less calcic in the footwall anorthosite (An_{67}) than plagioclase occurring in disseminated magnetite gabbro (An_{69}) and layer magnetite samples (An_{70}). An % of some trapped plagioclase grains in layer magnetite samples typically display significantly higher An % (up to An_{74}) in comparison to cumulus plagioclase occurring in the gabbroic host rocks.

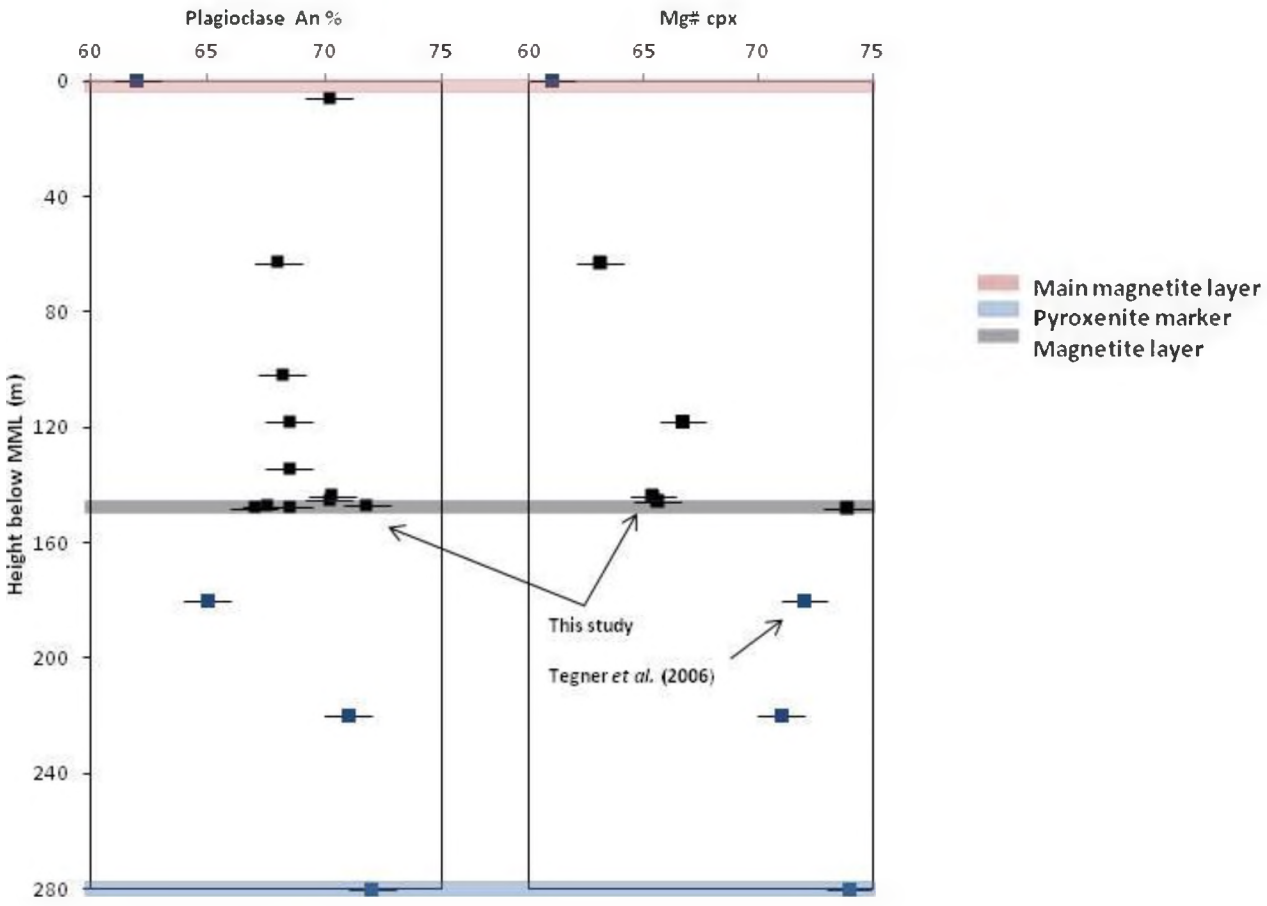

Figure 5.1: Plagioclase An % and clinopyroxene Mg# for the Pyroxenite marker and MML (data after Tegner *et al.* 2006) as well as samples from this study. Note the pronounced spike in Mg# cpx and An % of plagioclase at the base of the magnetite layer and then decreasing with height.

Table 5.1: Selected plagioclase core compositional data from the footwall anorthosite (AN- samples) and magnetite layer (BS- samples). For a full list of plagioclase compositional data see Appendix C.

Depth(m)	148.1	148.1	148.1	147.8	147.8	147.8	147.8	147.4	147.4	147.4
Sample	AN5_plag2	AN5_plag3	AN5_plag8	BS2_plag1	BS2_plag2	BS2_plag3	BS2_plag5	BS4_plag1	BS4_plag4	BS4_plag5
SiO_2	54.50	55.02	53.62	55.08	54.02	54.62	54.95	54.84	55.99	53.86
Al_2O_3	28.48	27.61	28.49	28.18	28.31	27.59	28.41	27.11	28.91	28.28
FeO	0.41	0.26	1.95	0.31	0.21	0.39	0.30	0.37	0.34	0.30
CaO	11.32	10.80	10.42	11.25	11.50	10.99	11.39	10.91	10.84	11.28
Na_2O	5.03	5.37	4.94	5.08	5.09	5.25	4.70	5.45	5.22	4.88
K_2O	0.18	0.11	0.38	0.02	0.00	0.02	0.15	0.06	0.15	0.14
BaO	0.00	0.00	0.00	0.00	0.00	0.00	0.00	0.00	0.00	0.00
Total	**99.91**	**99.16**	**99.81**	**99.91**	**99.13**	**98.87**	**99.89**	**98.74**	**101.45**	**98.74**
Si	2.46	2.50	2.44	2.48	2.46	2.49	2.48	2.50	2.49	2.46
Al	1.51	1.47	1.53	1.50	1.51	1.48	1.51	1.46	1.51	1.52
Fe	0.01	0.01	0.07	0.01	0.01	0.01	0.01	0.01	0.01	0.01
Ca	0.54	0.52	0.50	0.54	0.56	0.53	0.55	0.53	0.51	0.55
Na	0.44	0.47	0.43	0.44	0.44	0.48	0.41	0.48	0.45	0.43
K	0.01	0.01	0.02	0.00	0.00	0.01	0.01	0.01	0.01	0.01
Ba	0.00	0.00	0.00	0.00	0.00	0.00	0.00	0.00	0.00	0.00
Total	**4.97**	**4.98**	**4.99**	**4.97**	**4.98**	**5.00**	**4.97**	**4.99**	**4.98**	**4.98**
An	54	52	53	55	55	53	57	52	53	55
Ab	44	47	45	45	45	46	42	47	46	44
Or	2	1	2	0	0	1	1	1	1	1

Table 5.1 continued:

Depth(m)	147.2	147.2	147.2	147.2	147.2	147.2	147.2	147.2	147.2
Sample	BS5_plag1	BS5_plag2	BS5_plag3	BS5_plag4	BS5_plag6	BS5_plag7	BS5_plag8	BS5_plag10	BS5_plag12
SiO_2	54.23	54.04	54.16	54.07	54.64	54.55	54.32	53.44	55.25
Al_2O_3	27.74	29.00	29.41	29.41	27.69	28.22	28.32	27.53	27.22
FeO	0.37	0.38	0.27	0.26	0.45	0.34	0.37	0.17	0.23
CaO	12.97	13.36	13.10	12.90	11.70	12.20	12.20	12.43	11.42
Na_2O	4.75	4.55	4.67	4.36	5.01	4.79	4.89	4.93	4.89
K_2O	0.21	0.07	0.12	0.12	0.35	0.24	0.11	0.19	0.33
BaO	0.00	0.00	0.00	0.00	0.00	0.00	0.00	0.00	0.00
Total	**100.28**	**101.40**	**101.72**	**101.11**	**99.84**	**100.34**	**100.21**	**98.70**	**99.34**
Si	2.45	2.42	2.41	2.42	2.48	2.46	2.46	2.45	2.51
Al	1.48	1.53	1.54	1.56	1.48	1.50	1.51	1.49	1.46
Fe	0.01	0.01	0.01	0.01	0.01	0.01	0.01	0.01	0.01
Ca	0.63	0.64	0.63	0.61	0.57	0.59	0.59	0.61	0.56
Na	0.41	0.39	0.40	0.37	0.44	0.42	0.42	0.43	0.43
K	0.01	0.00	0.01	0.01	0.02	0.01	0.01	0.01	0.01
Ba	0.00	0.00	0.00	0.00	0.00	0.00	0.00	0.00	0.00
Total	**4.99**	**4.99**	**5.00**	**4.98**	**5.00**	**4.99**	**5.00**	**5.00**	**4.98**
An	59	61	60	61	55	58	58	58	55
Ab	39	38	39	38	43	41	42	41	43
Or	2	1	1	1	2	1	1	1	2

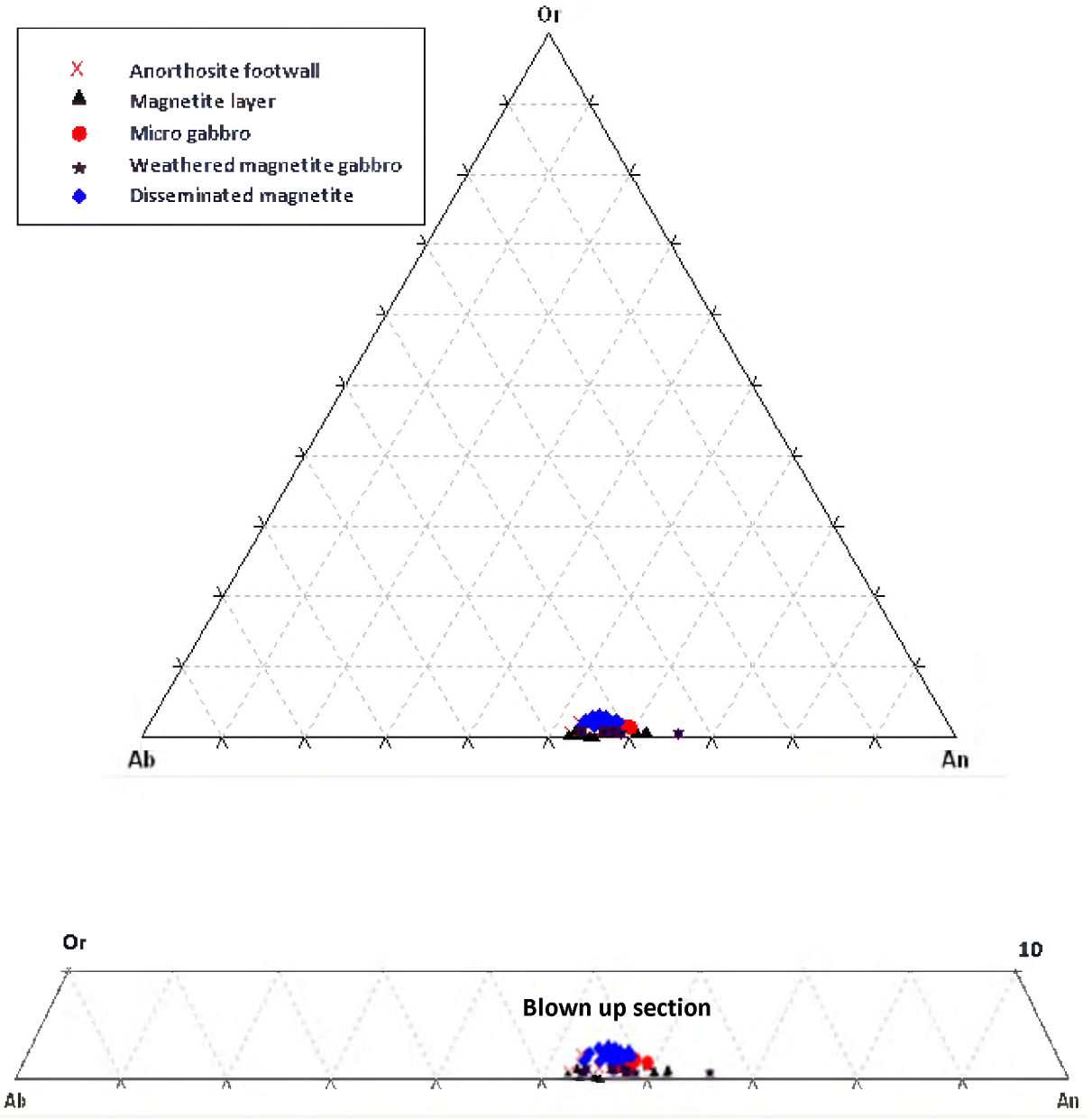

Figure 5.2: Measured plagioclase core compositions throughout the sampled suite of rocks. All measured plagioclase compositions lie within the labradoritic plagioclase field indicating their more calcic nature.

5.2. Pyroxene

5.2.1. Clinopyroxene

The majority of clinopyroxene grain compositions lie within the augite field, with a handful falling in the pigeonite field (Figure 5.3). The average composition of all clinopyroxene grains is $En_{38}Fs_{19}Wo_{43}$. Clinopyroxene occurring as inclusions in layer magnetites (sample BS-1)

have lower FeO content (averaging 9 wt. %) and a higher MgO content (averaging 15 wt. %) compared to cumulus clinopyroxene throughout disseminated magnetite gabbro and microgabbro samples, averaging 12 wt. % FeO and 13 wt. % MgO respectively. The Mg# ranges from 64.8 to 75.4 (averaging 67.3). The highest Mg# values occur within clinopyroxene in layer magnetite samples (averaging 73.9) whilst the Mg# of clinopyroxene grains in disseminated magnetite gabbro and microgabbro samples are significantly lower (averaging 66).

5.2.2. Orthopyroxene

Orthopyroxene compositions all fall in the enstatite field (Figure 5.3) with an average composition of $En_{52}Fs_{44}Wo_3$. The Mg# ranges from 51.7 to 66.8 (averaging 56.4). As with the An % of plagioclase, the Mg# of orthopyroxene grains occurring within layer magnetites is higher (averaging 66.8) compared to orthopyroxene occurring in disseminated magnetite gabbro and microgabbro samples (averaging. 56.8).

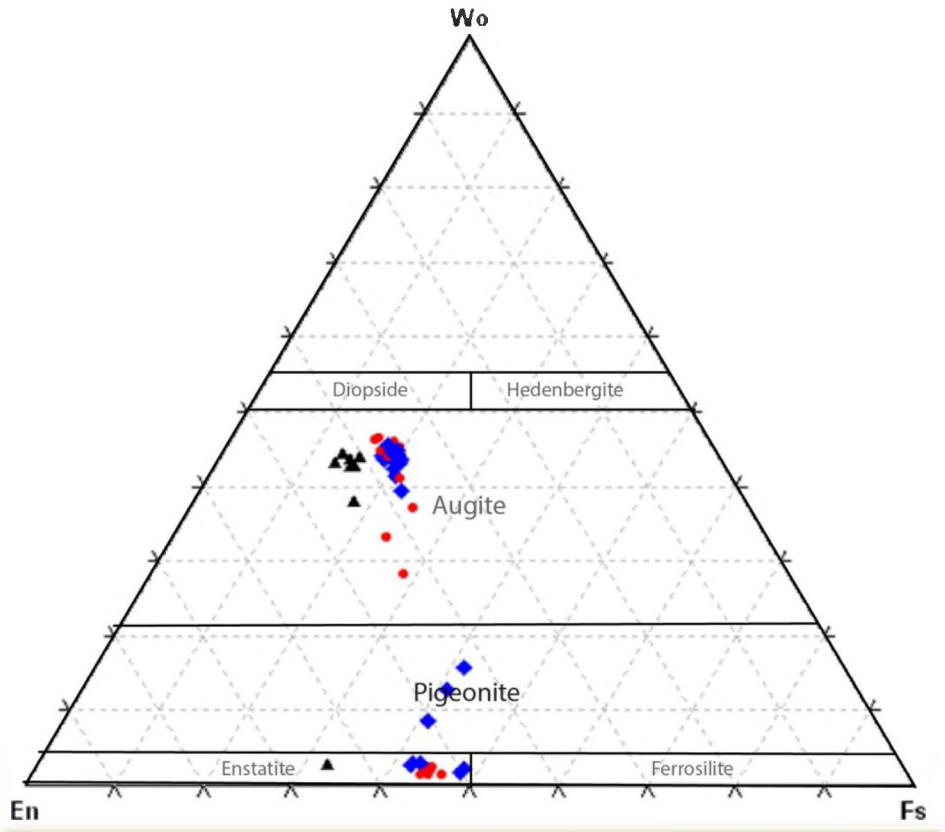

Figure 5.3: Ortho- and clinopyroxene compositions for the entire sample suite with accepted mineral names. Diagram modified after Morimoto *et al.* (1988). Symbols are the same as in Figure 5.2.

Table 5.2: Selected pyroxene compositional data for magnetite layer samples (BS- samples), disseminated magnetite gabbro samples (OFSZ- samples) and microgabbro samples (P-). For a full list of pyroxene compositional data see Appendix C.

Depth(m)	148	148	148	148	148	148	148	148	148
Sample	BS1_pyx1	BS1_pyx2	BS1_pyx3	BS1_pyx4	BS1_pyx5	BS1_pyx6	BS1_pyx7	BS1_pyx8	BS1_pyx11
SiO_2	51.91	52.19	50.59	52.14	53.05	52.56	52.35	51.66	52.60
TiO_2	0.42	0.42	0.40	0.38	0.24	0.38	0.48	0.39	0.54
Al_2O_3	1.66	1.69	1.65	1.58	0.93	1.74	1.65	1.65	1.96
Cr_2O_3	0.17	0.18	0.19	0.26	0.11	0.12	0.19	0.15	0.14
FeO	9.09	10.93	9.95	8.67	20.74	9.72	9.44	7.90	9.66
MnO	0.20	0.35	0.00	0.06	0.41	0.09	0.50	0.35	0.14
MgO	14.79	15.64	14.30	15.09	23.50	15.29	14.83	15.33	14.67
CaO	21.54	18.76	21.49	22.07	1.36	21.54	21.08	21.11	21.06
Na_2O	0.20	0.14	0.24	0.19	0.00	0.15	0.23	0.18	0.23
Total	**99.98**	**100.30**	**98.81**	**100.44**	**100.34**	**101.58**	**100.76**	**98.72**	**101.01**
Si	1.93	1.94	1.92	1.93	1.95	1.93	1.94	1.94	1.94
Ti	0.01	0.01	0.01	0.01	0.01	0.01	0.01	0.01	0.01
Al	0.07	0.07	0.07	0.07	0.04	0.07	0.07	0.07	0.08
Cr	0.01	0.01	0.01	0.01	0.00	0.01	0.01	0.00	0.00
Fe	0.28	0.34	0.31	0.27	0.64	0.29	0.29	0.25	0.30
Mn	0.01	0.01	0.00	0.00	0.01	0.00	0.01	0.01	0.00
Mg	0.82	0.87	0.81	0.83	1.29	0.83	0.82	0.86	0.81
Ca	0.86	0.74	0.86	0.88	0.05	0.85	0.83	0.85	0.83
Na	0.01	0.01	0.01	0.00	0.01	0.01	0.01	0.01	0.01
Total	**4.00**	**4.00**	**4.00**	**4.00**	**4.00**	**4.00**	**3.99**	**4.00**	**3.98**
En	42	44	40	42	65	42	42	44	42
Wo	44	38	44	44	3	43	43	43	43
Fe	14	18	16	14	33	15	15	13	15
Mg#	74	72	72	76	67	74	74	78	73

Table 5.2 continued:

Depth(m)	145	145	145	145	145	145	143	143	143	143
Sample	OFSZ4_pyx3	OFSZ4_pyx4	OFSZ4_pyx5	OFSZ4_pyx6	OFSZ4_pyx7	OFSZ4_pyx8	P1_pyx1	P1_pyx2	P1_pyx3	P1_pyx4
SiO_2	50.06	50.27	50.46	51.00	50.13	50.04	51.04	51.97	51.74	51.81
TiO_2	0.21	0.48	0.43	0.40	0.42	0.37	0.31	0.20	0.30	0.31
Al_2O_3	0.70	1.56	1.56	1.55	1.46	1.37	1.23	0.94	1.33	1.56
Cr_2O_3	0.00	0.03	0.05	0.00	0.00	0.00	0.21	0.16	0.16	0.16
FeO	25.37	12.84	12.90	12.43	12.20	11.65	11.50	9.90	13.36	11.60
MnO	0.59	0.16	0.38	0.33	0.82	0.18	0.40	0.36	0.54	0.20
MgO	17.84	13.06	13.36	13.28	13.42	13.32	12.91	13.35	13.49	12.76
CaO	4.22	22.17	20.42	21.82	22.14	22.72	22.85	22.93	20.79	23.06
Na_2O	0.01	0.19	0.15	0.22	0.15	0.19	0.22	0.20	0.15	0.24
Total	**99.00**	**100.76**	**99.69**	**101.02**	**100.73**	**99.84**	**100.66**	**100.01**	**101.87**	**101.71**
Si	1.92	1.88	1.91	1.90	1.87	1.88	1.92	1.96	1.93	1.93
Ti	0.01	0.01	0.01	0.01	0.01	0.01	0.01	0.01	0.01	0.01
Al	0.03	0.07	0.07	0.07	0.06	0.06	0.05	0.04	0.05	0.06
Cr	0.00	0.00	0.00	0.00	0.00	0.00	0.01	0.00	0.00	0.00
Fe	0.82	0.41	0.41	0.39	0.38	0.37	0.36	0.31	0.41	0.36
Mn	0.02	0.01	0.01	0.01	0.02	0.01	0.01	0.01	0.01	0.01
Mg	1.03	0.73	0.76	0.74	0.75	0.75	0.72	0.75	0.75	0.71
Ca	0.17	0.90	0.84	0.88	0.90	0.92	0.92	0.92	0.83	0.92
Na	0.00	0.01	0.01	0.01	0.01	0.01	0.01	0.01	0.01	0.01
Total	**4.00**	**4.02**	**4.02**	**4.01**	**4.00**	**4.01**	**4.01**	**4.01**	**4.00**	**4.01**
En	50	36	38	37	37	37	36	38	37	35
Wo	9	44	41	43	43	45	46	46	41	46
Fe	41	20	21	20	20	18	18	16	22	19
Mg#	56	64	65	66	66	67	67	70	64	66

5.3. Ti-Magnetite

TiO_2 content of magnetite in layer magnetite and disseminated magnetite gabbro samples ranges between 6-22 wt. % (averaging 14 wt. %). TiO_2 content is noticeably higher in weathered magnetite gabbros (averaging 17 wt. %) in comparison to layer magnetites (averaging 14 wt. %). MgO and Al_2O_3 both show a positive correlation with TiO_2 in layer magnetite samples (Figure 5.4). V_2O_3 contents (Figure 5.4) are highest in weathered disseminated magnetite gabbros (averaging 1.26 wt. %) compared to fresh disseminated magnetite gabbros (averaging 1.13 wt. %) and layer magnetites (averaging 1.05 wt. %). FeO content in layer magnetites ranges between 65-80 wt. % (averaging 74 wt. %) and almost identical throughout disseminated magnetite gabbro samples (averaging 73 wt. %). Cr_2O_3 contents are generally below detection limits except at the base of the magnetite layer where it averages 0.5 wt. %.

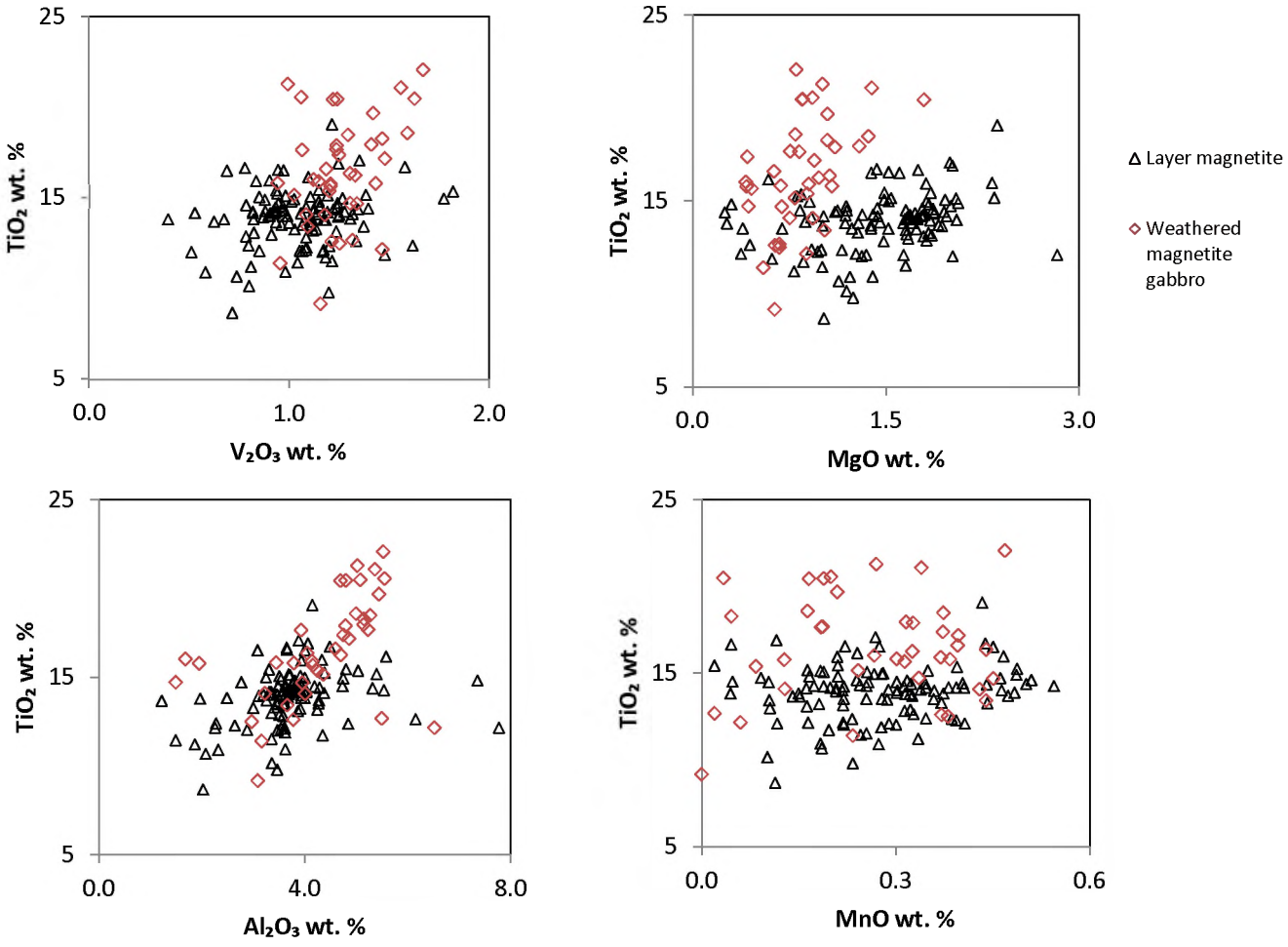

Figure 5.4: Binary diagrams showing TiO_2 versus V_2O_3, MgO, Al_2O_3 and MnO in magnetite for layer magnetite and weathered disseminated magnetite samples. Note, TiO_2 content is higher for magnetite grains in the weathered disseminated magnetite

Table 5.3: Selected ilmenite compositional data for magnetite layer samples (BS-) and disseminated magnetite gabbro samples (OFSZ-). See Appendix C for a full list of ilmenite compositions.

Depth(m)	147.2	147.2	147.2	147.2	147.2	147.2	147.2	147.2	145.5	145.5
Sample	BS5_ilm6	BS5_ilm7	BS5_ilm8	BS5_ilm9	BS5_ilm10	BS5_ilm11	BS5_ilm12	BS5_ilm13	OFSZ4_ilm1	OFSZ4_ilm3
Al_2O_3	0.04	0.02	0.07	0.04	0.04	0.11	0.03	0.01	0.03	0.06
SiO_2	0.02	0.03	0.00	0.11	0.03	0.05	0.03	0.02	0.05	0.01
MgO	2.62	2.83	2.74	2.80	2.78	2.08	2.58	2.65	1.72	0.74
FeO	45.07	43.31	44.82	44.10	43.90	43.21	42.97	41.31	43.24	44.43
MnO	0.59	0.59	0.39	0.75	0.50	0.62	0.36	0.33	0.71	0.97
V_2O_3	0.30	0.23	0.38	0.38	0.14	0.26	0.18	0.29	0.04	0.30
Cr_2O_3	0.02	0.25	0.00	0.90	0.00	0.00	0.37	0.02	0.00	0.00
TiO_2	53.32	53.20	53.03	52.12	52.71	52.15	52.22	53.31	52.81	52.54
Total	**101.99**	**100.47**	**101.44**	**101.12**	**100.10**	**98.48**	**98.74**	**97.95**	**98.60**	**99.04**
Al	0.00	0.00	0.00	0.00	0.00	0.00	0.00	0.00	0.00	0.00
Si	0.00	0.00	0.00	0.00	0.00	0.00	0.00	0.00	0.00	0.00
Mg	0.07	0.07	0.07	0.07	0.07	0.05	0.06	0.07	0.04	0.02
Fe	0.63	0.60	0.62	0.61	0.61	0.60	0.60	0.58	0.60	0.62
Mn	0.01	0.01	0.01	0.01	0.01	0.01	0.01	0.01	0.01	0.01
V	0.00	0.00	0.00	0.01	0.00	0.00	0.00	0.00	0.00	0.00
Cr	0.00	0.00	0.00	0.00	0.00	0.00	0.00	0.00	0.00	0.00
Ti	1.34	1.33	1.33	1.31	1.32	1.31	1.31	1.34	1.32	1.32
Total	**2.04**	**2.02**	**2.03**	**2.01**	**2.01**	**1.98**	**1.98**	**1.98**	**1.98**	**1.97**

5.4. Ilmenite

Ilmenite in magnetite layer samples has slightly higher TiO_2 contents (averaging 53 wt. %) in comparison to ilmenite in disseminated magnetite gabbros (averaging 51 wt. %). MgO contents are also higher in ilmenite grains within layer magnetites (averaging 2.6 wt. %) compared to the disseminated magnetite gabbros (averaging 1.1 wt. %). MnO content ranges from 0.3-0.9 wt. % while V_2O_3 and Cr_2O_3 contents for are in very low abundances and generally below detection limits.

5.5. Sulphides

Pyrite (FeS_2) and chalcopyrite ($CuFeS_2$) are the only sulphide phases present in these rocks. Figure 5.5 shows WDS scans of fine-grained sulphides occurring as inclusions in predominantly plagioclase (and a few within magnetite). Sulphides are not found within layer magnetite samples but are relatively common throughout disseminated magnetite gabbro and microgabbro samples.

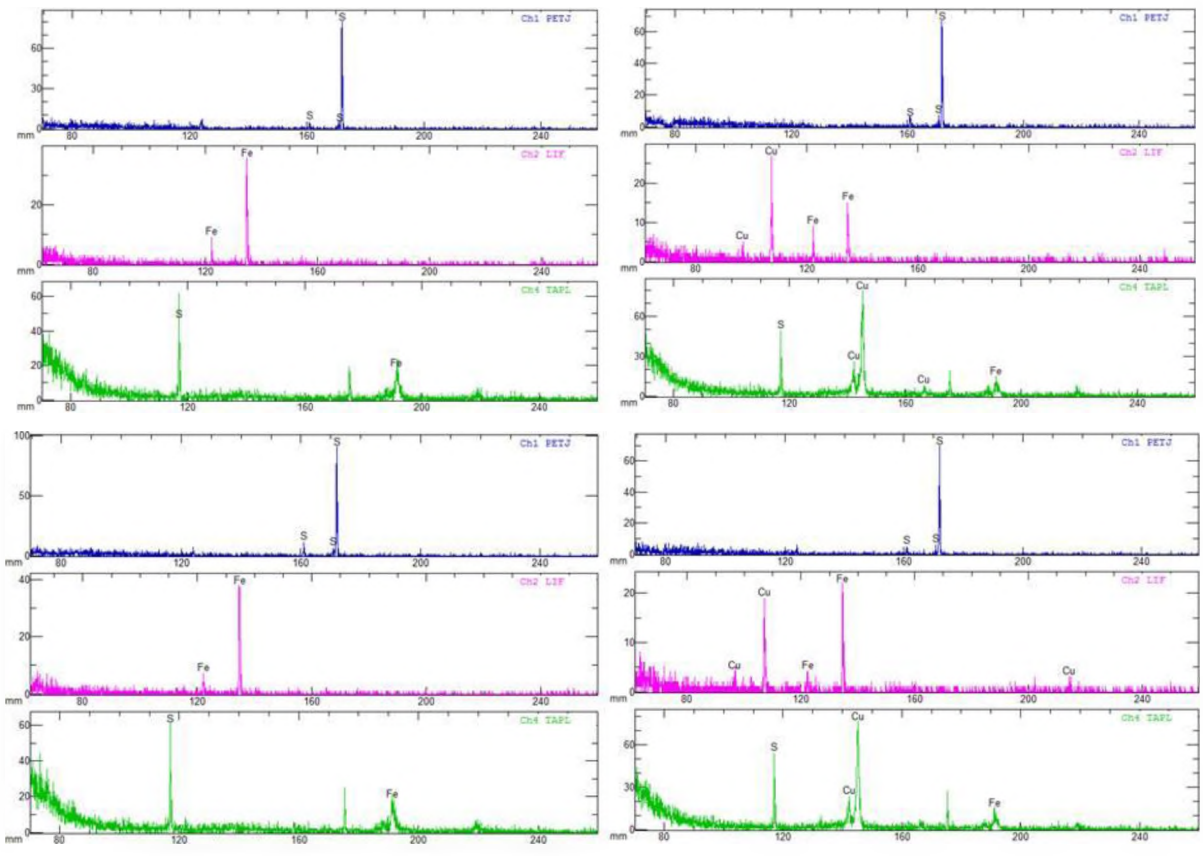

Figure 5.5: WDS scans of (a) pyrite grain, sample OBSZ-6 (b) chalcopyrite grain from disseminated magnetite gabbro, sample OBSZ-6 (c) pyrite grain from disseminated magnetite gabbro, sample OHSZ-4 (d) chalcopyrite grain from microgabbro, sample P-1.

5.6. Reaction rims and corona textures

A few distinct reaction rim and corona textures are observable throughout these rocks. Olivine, plagioclase + orthopyroxene symplectites and chlorite are the three main types observed and are described below. Mineral chemistry of these may have implications for the formation conditions of Ti-magnetite ore layers in the UZ.

5.6.1. Olivine

Fine-grained olivine with triple junction grain boundaries occurs at the interface between magnetite and plagioclase within layer magnetite samples and is particularly well developed in samples BS-3 and BS-5 (Figure 4.6a; 4.7b). The average composition of these olivine grains is Fo_{63}. There is no significant variation in MgO and FeO content (both with a narrow compositional range of 31-32 wt. % respectively).

Table 5.4: Fine-grained reaction rim olivine compositional data

Depth (m)	147.2	147.2	147.2
Sample	BS5_rim4_Olivine	BS5_rim5_Olivine	BS5_rim9_Olivine
SiO_2	36.18	35.99	36.58
TiO_2	0.05	0.27	0.04
Al_2O_3	0.01	0.00	0.18
Cr_2O_3	31.55	0.00	0.00
FeO	0.22	32.90	32.87
MnO	31.51	0.21	0.39
MgO	0.03	32.04	30.29
CaO	0.00	0.03	0.13
Total	**99.54**	**101.44**	**100.49**
Si	0.99	0.97	1.00
Ti	0.00	0.01	0.00
Al	0.00	0.00	0.01
Cr	0.00	0.00	0.00

Fe	0.72	0.74	0.75
Mn	0.01	0.01	0.01
Mg	1.28	1.28	1.23
Ca	0.00	0.00	0.00
Total	**3.00**	**3.00**	**3.00**
Fo	64	63	62
Fa	36	37	38

5.6.2. Symplectite intergrowths

Plagioclase + orthopyroxene symplectite intergrowths (Figure 4.6b-e; 4.7d,e) are a common reaction rim corona texture occurring between plagioclase and magnetite throughout the magnetite layer and disseminated magnetite gabbros. These are very fine-grained intergrowths, often too fine-grained to obtain accurate compositional data as the electron beam is not small enough to analyse any given intergrowth. However, few grains allowed for accurate analysis of which plagioclase compositions reflect compositions similar to the coarse-grained, lath-shaped plagioclase abundant throughout these rocks (11-12 wt. % CaO, 4-5 wt. % Na_2O). The orthopyroxene compositions within the symplectites are a lot more difficult to constrain as they are the finer-grained, 'worm-like' portion of the intergrowth (Figure 4.7e).

5.6.3. Chlorite

Coronas of Fe-rich chlorite occur in very coarse-grained sections at the interface between plagioclase and magnetite grain boundaries (Figure 4.7c,d). These chlorite coronas often have a symplectite intergrowth composed of plagioclase + orthopyroxene surrounding it, but it is occasionally not developed on the magnetite grain boundary side. Compositionally, chlorite has SiO_2 content ranging 28-29 wt. %, Al_2O_3 ranges from 11-13 wt. %, FeO ranges from 42-43 wt. % while MgO ranges from 2-3 wt. %.

5.7. Stratigraphic variations

Plagioclase lath compositions show a small but distinct difference in An % between layer magnetite and disseminated magnetite gabbroic rocks above and below the magnetite layer. An % of plagioclase increases from An_{67} below the magnetite layer to An_{71} within the magnetite layer and decreases again to An_{68} above the magnetite layer. Clinopyroxene Mg# shows a similar trend. Mg# of clinopyroxene within the magnetite layer averages 73.9 and then decreases to 65 within the disseminated magnetite gabbros above the magnetite layer. Magnetite within layer magnetites also typically has significantly higher MgO contents (averaging 1.44 wt. %) than magnetite found in disseminated magnetite gabbros (averaging 0.54 wt. %). This also applies to MgO content of ilmenite being higher within layer magnetites (averaging 2.73 wt. %) and lower within disseminated magnetite gabbros (averaging 1.63 wt. %). Al_2O_3 content of magnetite is higher in weathered magnetite gabbros (averaging 4.31 wt. %) than layer magnetites (averaging 3.75 wt. %) and disseminated magnetite gabbros (averaging 2.97 wt. %). TiO_2 content in magnetite is highest in weathered magnetite gabbros (averaging 16.49 wt. %) with values significantly lower in layer magnetites (averaging 13.84 wt. %) and fresh disseminated magnetite gabbros (averaging 13.22 wt. %).

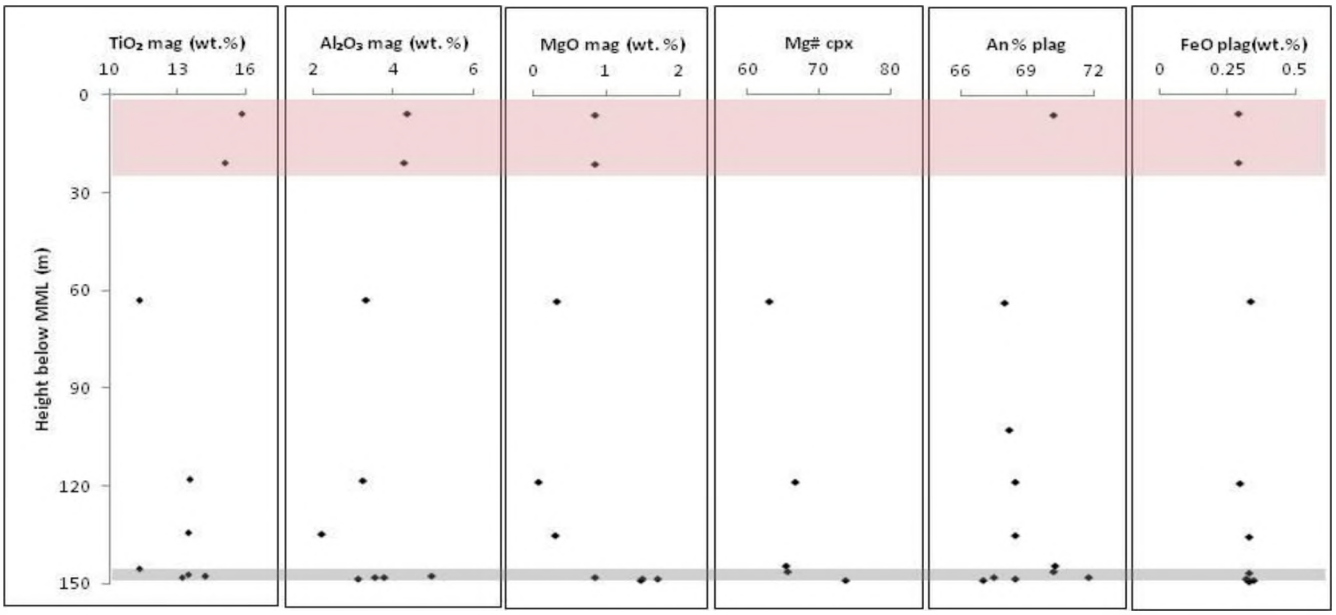

Figure 5.6: Stratigraphic variations of various elements in magnetite, clinopyroxene and plagioclase throughout the 150 m of core. Shaded areas represent a magnetite layer (grey) and a weathered disseminated magnetite gabbro zone (pink).

6. Whole-rock geochemistry

6.1. Trace element geochemistry

Trace element concentrations were analysed using two different methods, namely ICP-MS and XRF spectrometry (for a full description of the methods used see Chapter 2.3). Duplicate samples analysed for XRF vs. ICP-MS show good positive correlations for most elements measured (Appendix D). Absolute concentrations for most elements show similar values for both methods used e.g. Sr, Ni, Zn, Cu, Zr. There are however, a few exceptions e.g. a high Cr concentration for XRF measured 5000 ppm and was only measured to be 3097 ppm using ICP-MS. Another example is Nb, where maximum concentrations measure 6.7 ppm for XRF and 3.4 ppm for ICP-MS (approximately half that of the XRF value).

Therefore, direct comparisons of trace element ratios from XRF vs. ICP-MS can be done with confidence for most elements but caution must still be taken when directly comparing certain elements e.g. Cr, Nb. A full list of whole-rock trace element concentrations can be seen in Appendix B.

6.1.1. Trace element variations

Trace element analysis was performed for the entire sample suite. Trace element variations for Sr, Th, Co, Zr, Zn and Nb plotted against V (ppm) are depicted in Figure 6.1. Th, Co, Zn as well as high field strength elements (HFSE) Zr and Nb all show a strong positive correlation with V whilst Sr displays a fairly strong negative correlation. V concentrations show highest concentrations within the magnetite layer, reaching >17 000 ppm (1.7 wt. %). The weathered magnetite gabbros show a slight depletion in Sr, Co, Zr and Nb relative to the fresh disseminated magnetite gabbros whilst showing a similarly high-V trend.

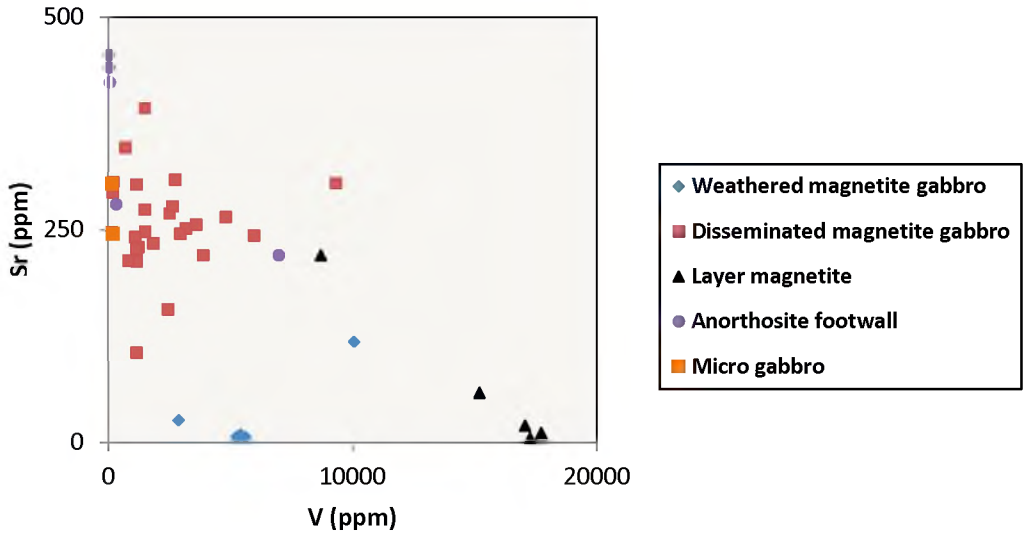
500
250
0
Sr (ppm)
0
10000
20000
V (ppm)
Weathered magnetite gabbro
Disseminated magnetite gabbro
Layer magnetite
Anorthosite footwall
Micro gabbro

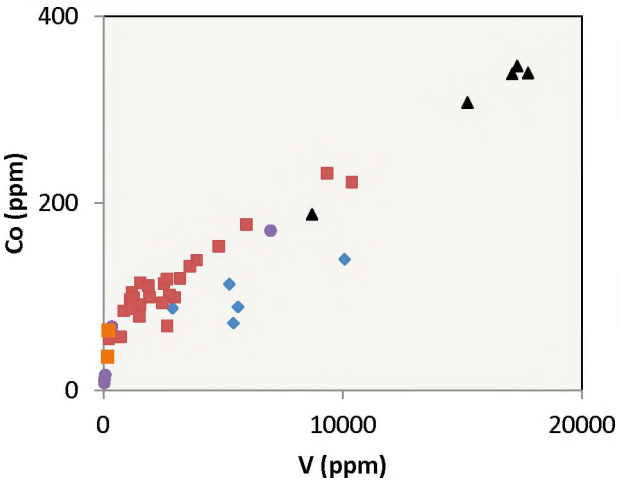
400
200
0
Co (ppm)
0
10000
20000
V (ppm)

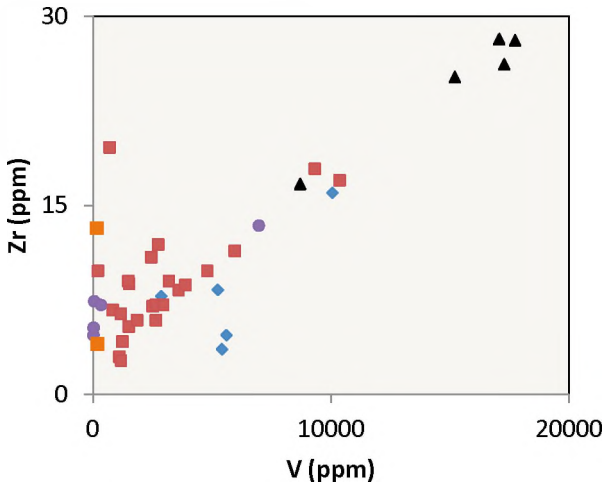
30
15
0
Zr (ppm)
0
10000
20000
V (ppm)

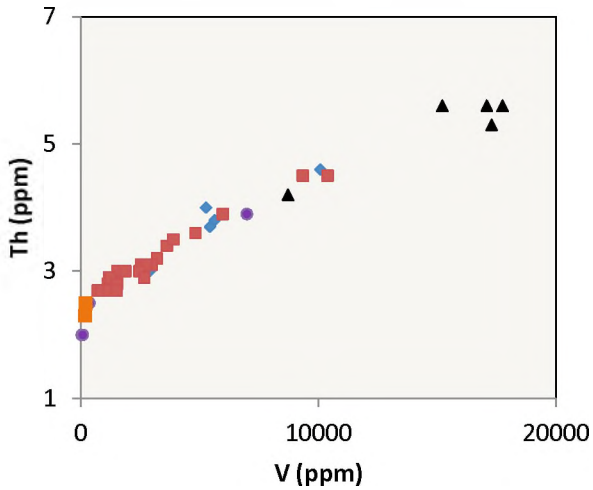
7
5
3
1
Th (ppm)
0
10000
20000
V (ppm)

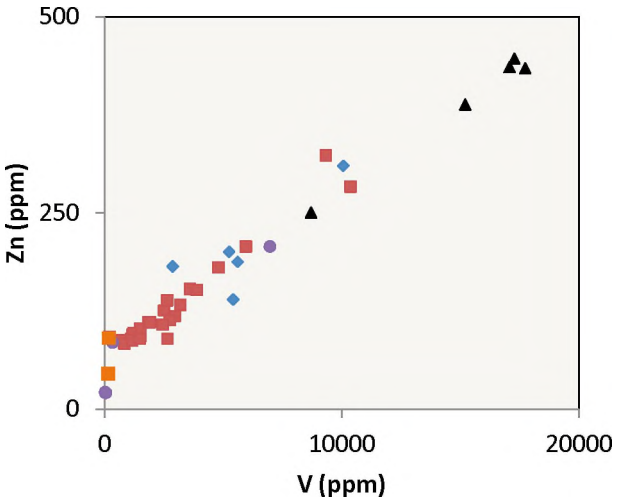
500
250
0
Zn (ppm)
0
10000
20000
V (ppm)

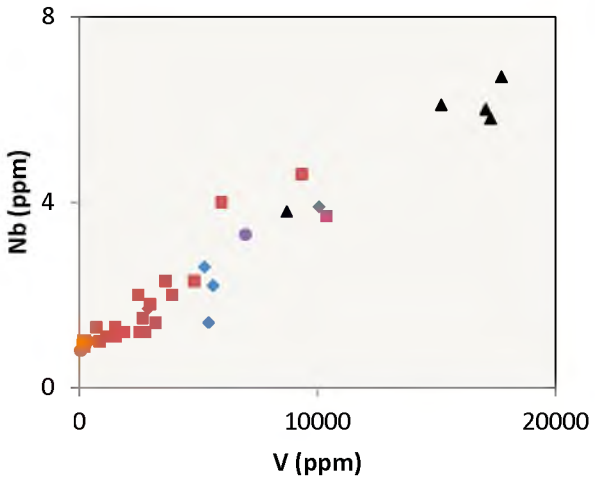

Figure 6.1: Binary diagrams showing Sr, Th, Co, Zr, Nb and Zn whole-rock trace element variations against V (ppm) across the entire 150 m sample suite. Symbols: Blue diamonds = weathered magnetite gabbros; Red squares = Disseminated magnetite gabbros; Black triangles = Layer magnetites; Purple circles = Anorthosite footwall.

Figure 6.2 shows various selected trace element variations. HFSE Zr, Nb, Ta and Hf all positively correlate with one another with particularly high abundances in magnetite layer samples. Large Ion Lithophile Elements (LILE) Rb and Ba do not show any correlation, showing very low abundances in magnetite layer samples and noticeable scatter throughout disseminated magnetite gabbro samples. Ni and Cu illustrate two trends, a high Ni trend in magnetite layer samples and a high Cu trend throughout weathered magnetite gabbro samples. Ni concentrations average 511 ppm in layer magnetite samples and only 143 ppm in disseminated magnetite gabbro samples. Weathered magnetite gabbro samples have high Cu concentrations averaging 893 ppm and much lower Ni concentrations, averaging 197 ppm.

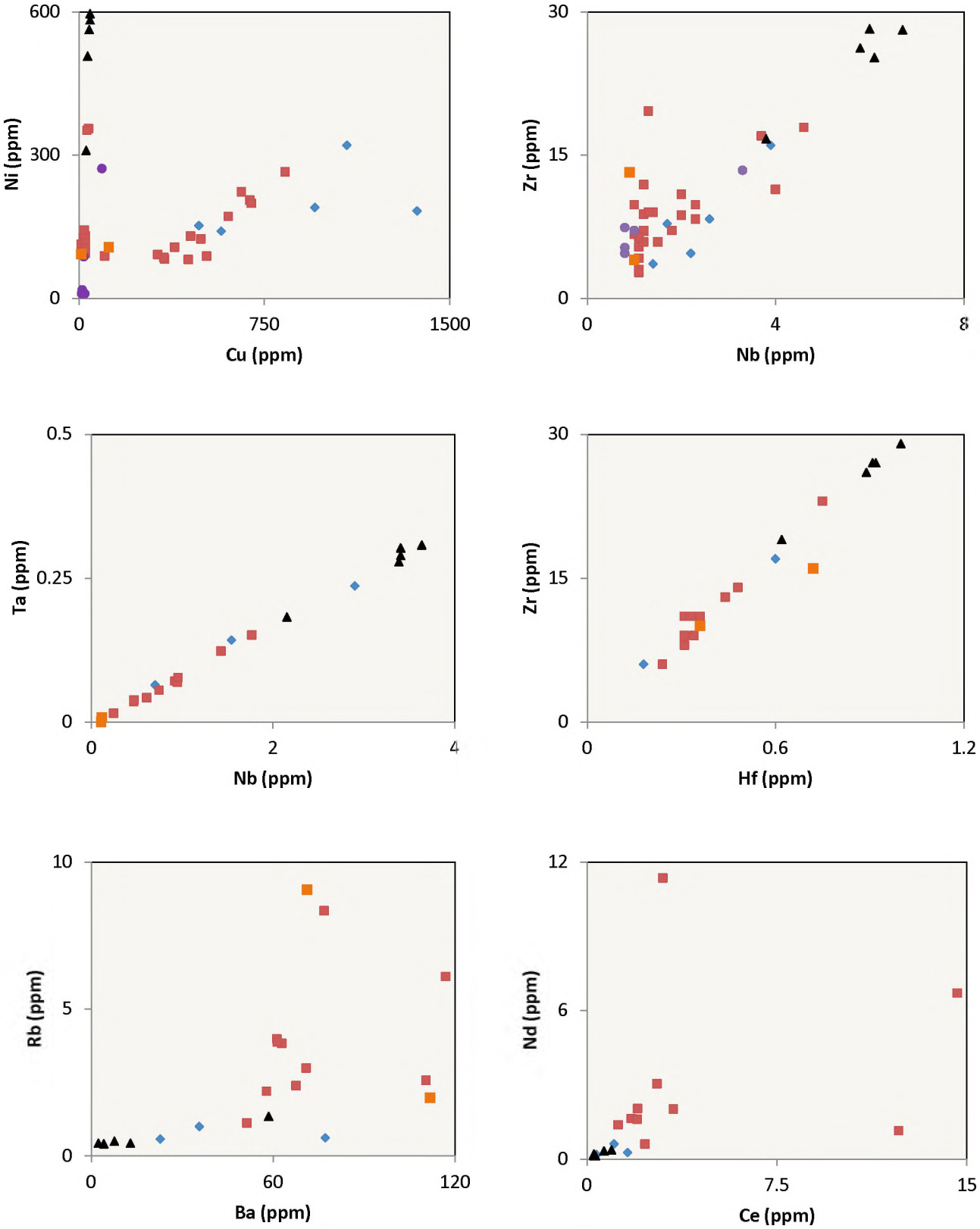

Figure 6.2: Binary plots showing selected trace element variations across the entire 150 m sampled section. Note: Symbols are the same as Figure 6.1.

6.1.2. Trace element stratigraphic variations

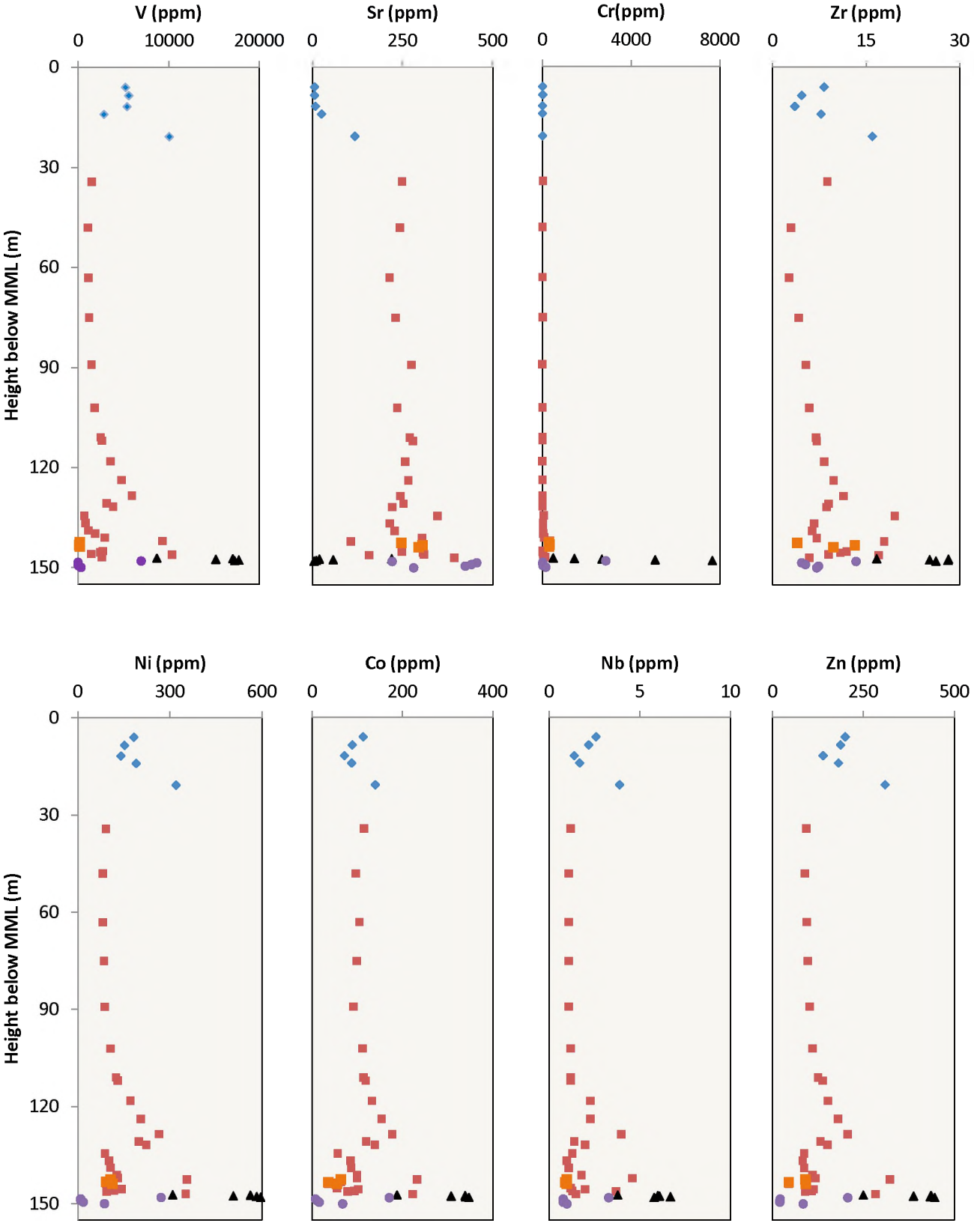

Figure 6.3: Selected trace element stratigraphic variations (V, Sr, Cr, Zr, Ni, Co, Nb and Zn). Symbols are the same as Figure 6.1.

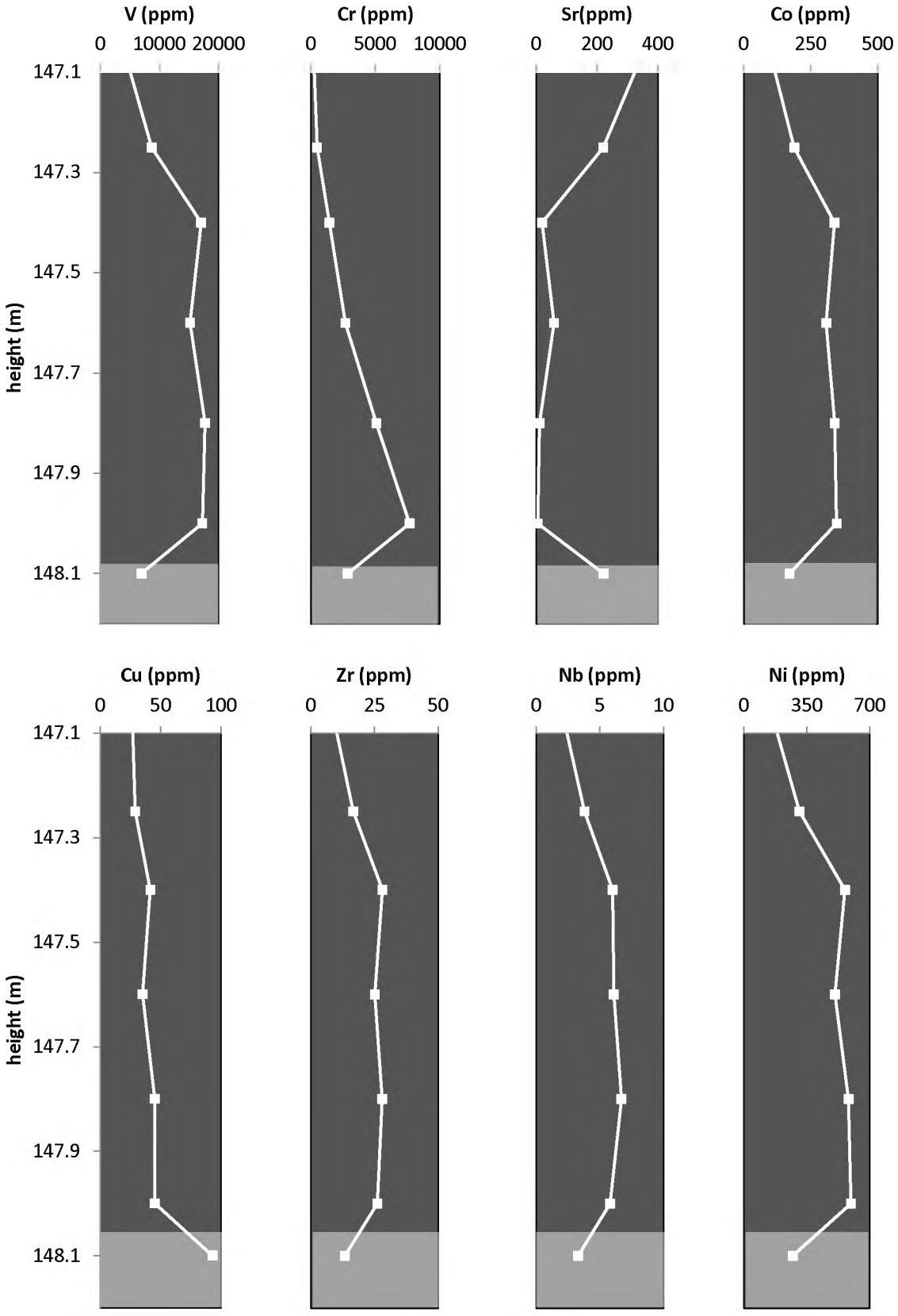

Figure 6.4: Selected trace element variations (V, Cr, Sr, Co, Cu, Zr, Nb and Ni) across a massive magnetite layer from the anorthosite footwall at the base (148.1 m) through to the top where magnetite becomes disseminated, over a one metre section. Light grey = Anorthosite footwall, dark grey = massive magnetite layer.

V, Zr, Ni, Co, Zr, Nb and Zn all show the same trends across stratigraphy (Figure 6.3), high abundances within a magnetite layer and strongly decreasing upwards with a spike again at the base of a weathered disseminated magnetite layer. Sr shows highest abundances within the footwall anorthosite and shows a consistent trend throughout the disseminated magnetite gabbro, and then decreases abruptly throughout the weathered magnetite gabbro.

6.1.3. Magnetite layer trace element variations

Refer to Figure 6.4 for the following trace element variations. Transition metals V, Co and Ni all show highest abundances at the base of the magnetite layer and remain constant over a 0.3 m interval before decreasing at the top of the layer. Cr shows a completely different trend with a rapid vertical depletion directly from the base of the layer upwards (from approximately 7000 ppm at the base to 129 ppm at the top of the layer). Cu is negatively correlated with the other transition metals and abundances are generally less than 50 ppm throughout the layer. HFSE abundances of Zr (<50 ppm) and Nb (<10 ppm) are positively correlated with the transition metals and display the same trends as them. Sr displays a similar trend to Cu, with highest abundances below the base of layer in the footwall anorthosite, decreasing significantly throughout the layer and increasing again towards the top of the layer as more cumulus plagioclase appears in the system.

6.1.4. REE profiles

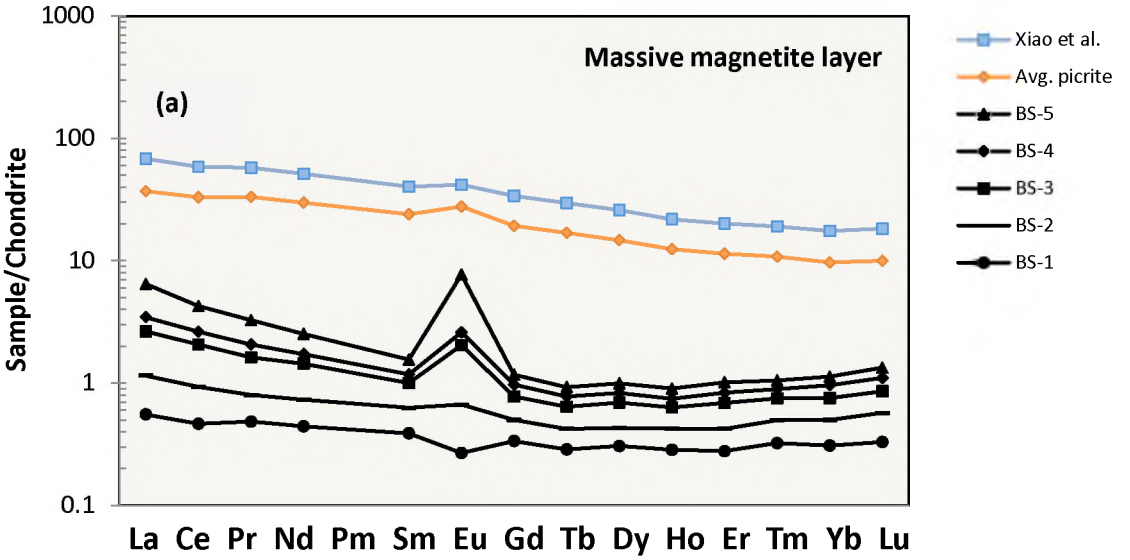

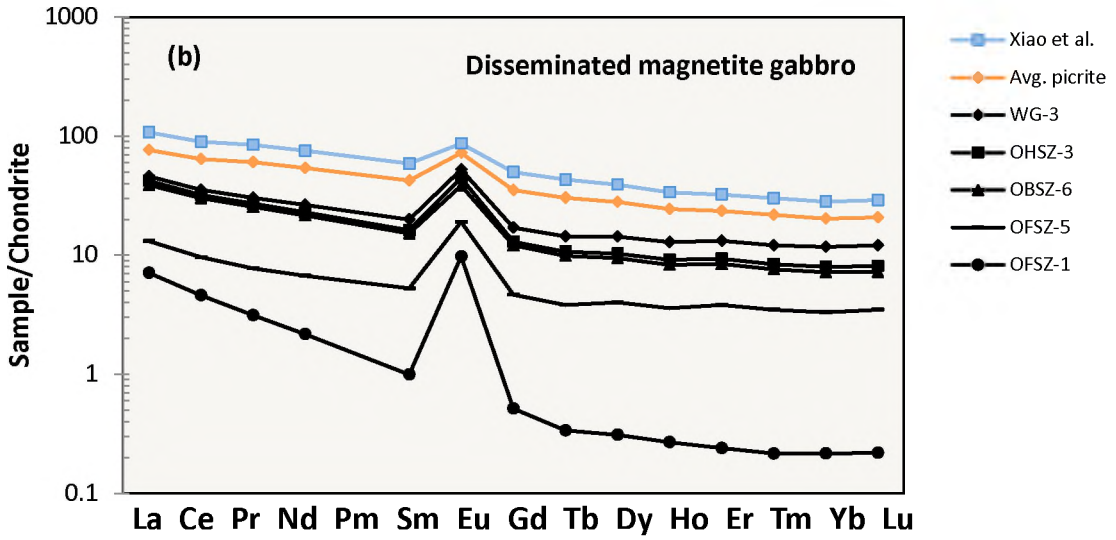

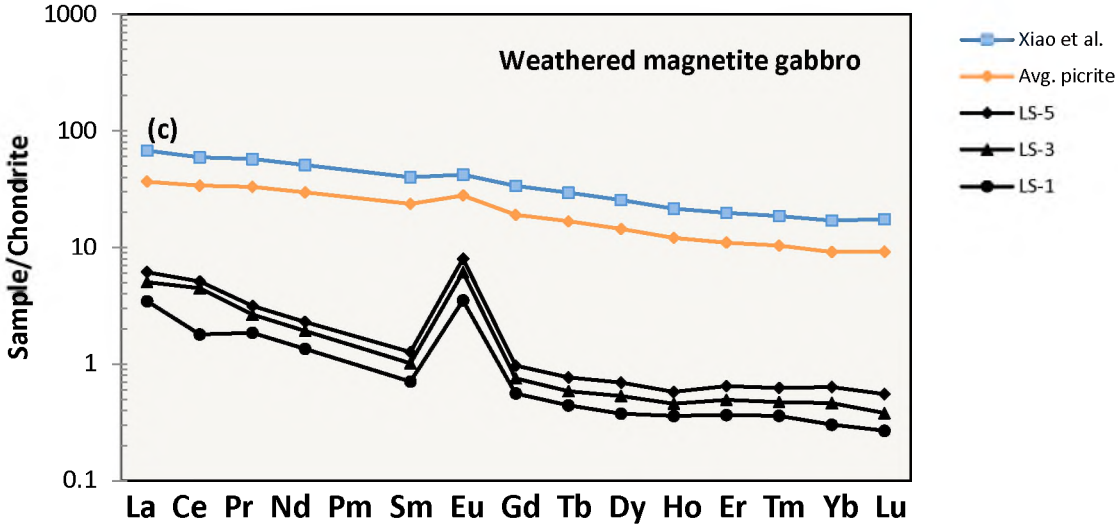

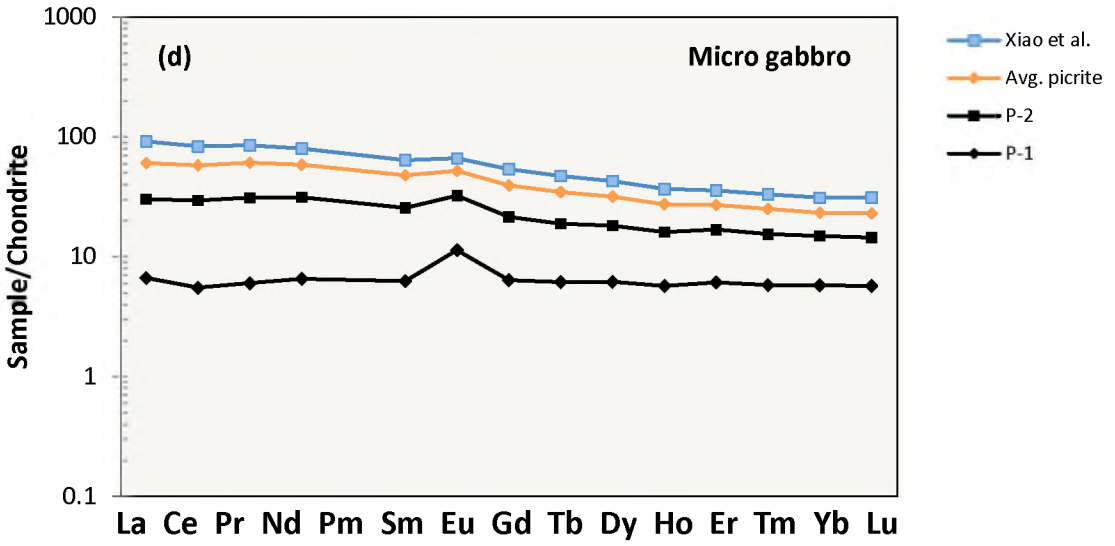

Figure 6.5: Chondrite-normalised (after Anders and Grevesse, 1989) REE profiles for (a) layer magnetite samples, (b) Disseminated magnetite gabbro samples, (c) weathered magnetite gabbro samples and (d) Microgabbro samples. The average picrite from the Emeishan LIP (after Li *et al.* 2010) and high-Ti basalt (after Xiao *et al.* 2004) are plotted for comparative purposes. Blue squares = High-Ti basalt, orange triangles = Average picrite.

REE concentrations are extremely low for the layer magnetite samples (Figure 6.5a), with a slight increase from the base of the layer upwards. LREEs are more enriched (La/Sm ratios ranging from 1.43-7.98) than HREEs (Gd/Yb ratios ranging from 0.85-1.22) which show a flat profile throughout the magnetite layer (La/Lu ratios range from 1.68-12.72). There is a small negative Eu anomaly at the base of the layer and this becomes positive as cumulus plagioclase enters the system. Disseminated magnetite gabbro samples show similar REE profiles to those of an average picrite and High-Ti basalt (Figure 6.5b), with exception to one sample, OFSZ-1 which shows a strong depletion in HREE. La/Lu ratios range from 0.95-12.72 with an outlier of 32.43 in sample OFSZ-1. They all show a positive Eu anomaly with a slight enrichment in LREE (La/Sm ratios ranging from 0.99-3.46) in comparison to HREE (Gd/Yb ratios ranging from 1.04-1.93). Weathered magnetite gabbro samples (Figure 6.5c) have low concentrations of REEs (La/Lu ratios ranging from 6.41-14.19) relative to the average picrite and Hi-Ti basalt. These rocks also show a strong depletion in HREEs (Gd/Yb ratios ranging from 1.21-1.86) compared to LREEs (La/Sm ratios ranging from 4.40-5.15), with a strong positive Eu anomaly present.

6.1.5. Trace element spider diagrams

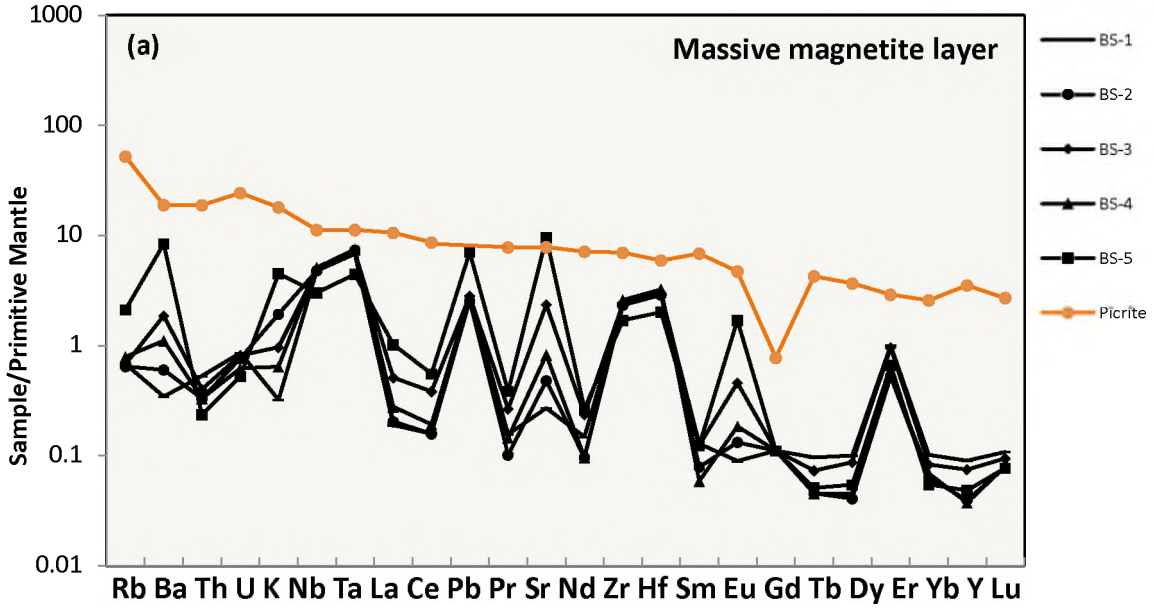

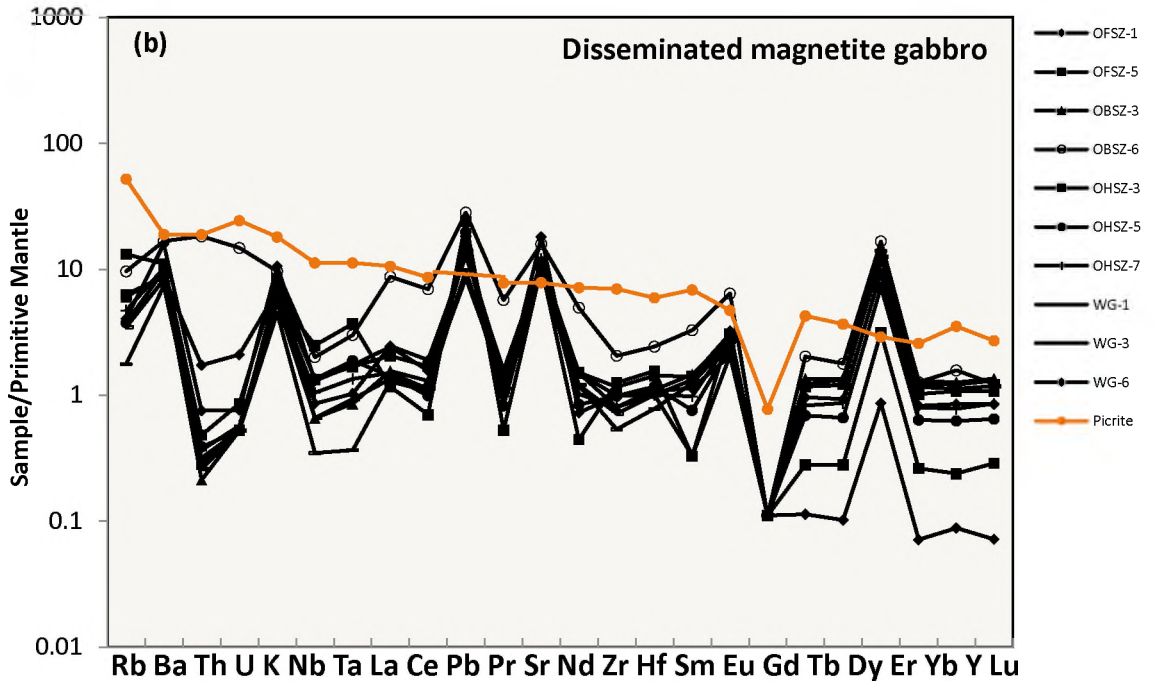

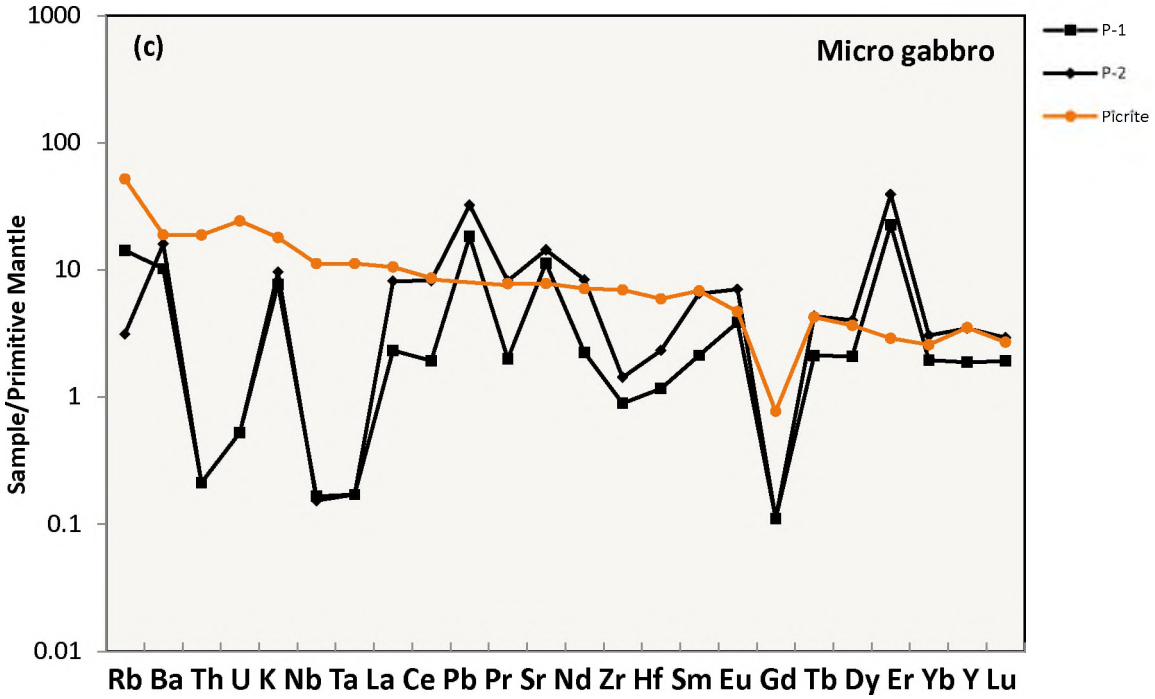

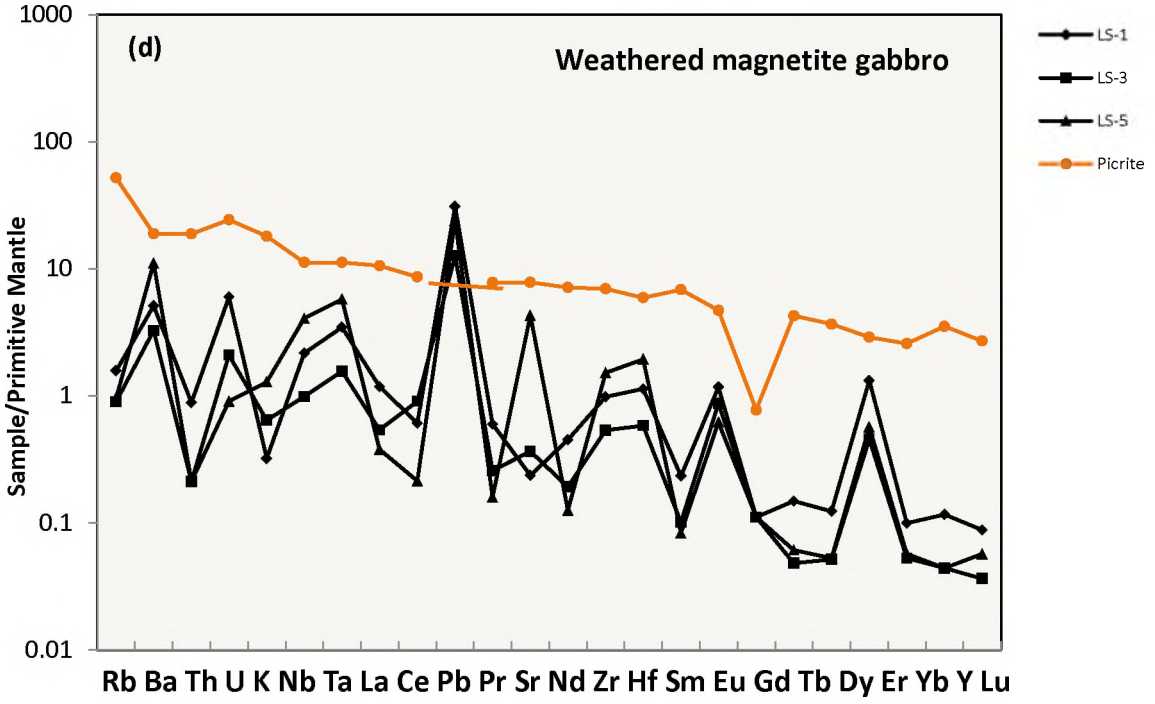

Figure 6.6: Primitive mantle normalised trace element spider diagrams for (a) massive magnetite layer (b) disseminated magnetite gabbro (c) Microgabbro and (d) Weathered magnetite gabbro. Orange symbols represent and average picrite from the ELIP (after Li *et al.* 2010).

6.2. Major element geochemistry

Figure 6.7 shows selected major element variations against SiO_2. CaO concentrations are highest throughout the disseminated magnetite gabbro (averaging 9.8 wt. %) and show a strong positive correlation with SiO_2. MgO concentrations are generally very low throughout the layer magnetite (averaging 1.9 wt. %) and weathered magnetite gabbros (averaging 0.51 wt. %). Overall, MgO shows a weak correlation with SiO_2. Al_2O_3 shows a slightly better correlation with SiO_2, with highest concentrations throughout the disseminated magnetite gabbros (averaging 15.1 wt. %) and weathered magnetite gabbros (averaging 13.7 wt. %). Al_2O_3 concentrations are significantly lower for layer magnetite samples (averaging 6.1 wt. %), correlating well with the low SiO_2 concentrations (averaging 6.64 wt. %). Fe_2O_3 concentrations show a strong negative correlation with SiO_2, with highest concentrations obviously throughout the magnetite layer (averaging 72 wt. %). Fe_2O_3 concentrations throughout the weathered disseminated magnetite gabbros are also considerably higher (averaging 50.1 wt. %) than in the fresh disseminated magnetite gabbros (averaging 21.6 wt. %). $Na_2O + K_2O$ concentrations are considerably low for all the samples (<5 wt. %) but are extremely low for layer magnetite (averaging 0.58 wt. %) and weathered disseminated magnetite gabbros (averaging 0.32 wt. %).

SiO_2, MgO, CaO and $Na_2O + K_2O$ all show lowest abundances within the magnetite layer and increases steadily upwards throughout the disseminated magnetite gabbro (particularly as more cumulus plagioclase and pyroxene crystallises) until the weathered magnetite gabbro zone where abundances then decrease. Al_2O_3 shows a slightly different trend as it remains relatively constant (averaging 14.8 wt. %) from the top of the magnetite layer upwards through into the weathered magnetite gabbro. Interestingly, Al_2O_3 does not show the same depletion trend as CaO and $Na_2O + K_2O$ in this zone, but rather consistent values. Fe_2O_3 concentrations are highest at the base of the magnetite layer and then decrease rapidly upwards until values increase again within the weathered magnetite gabbro.

6.2.1. Major element variations

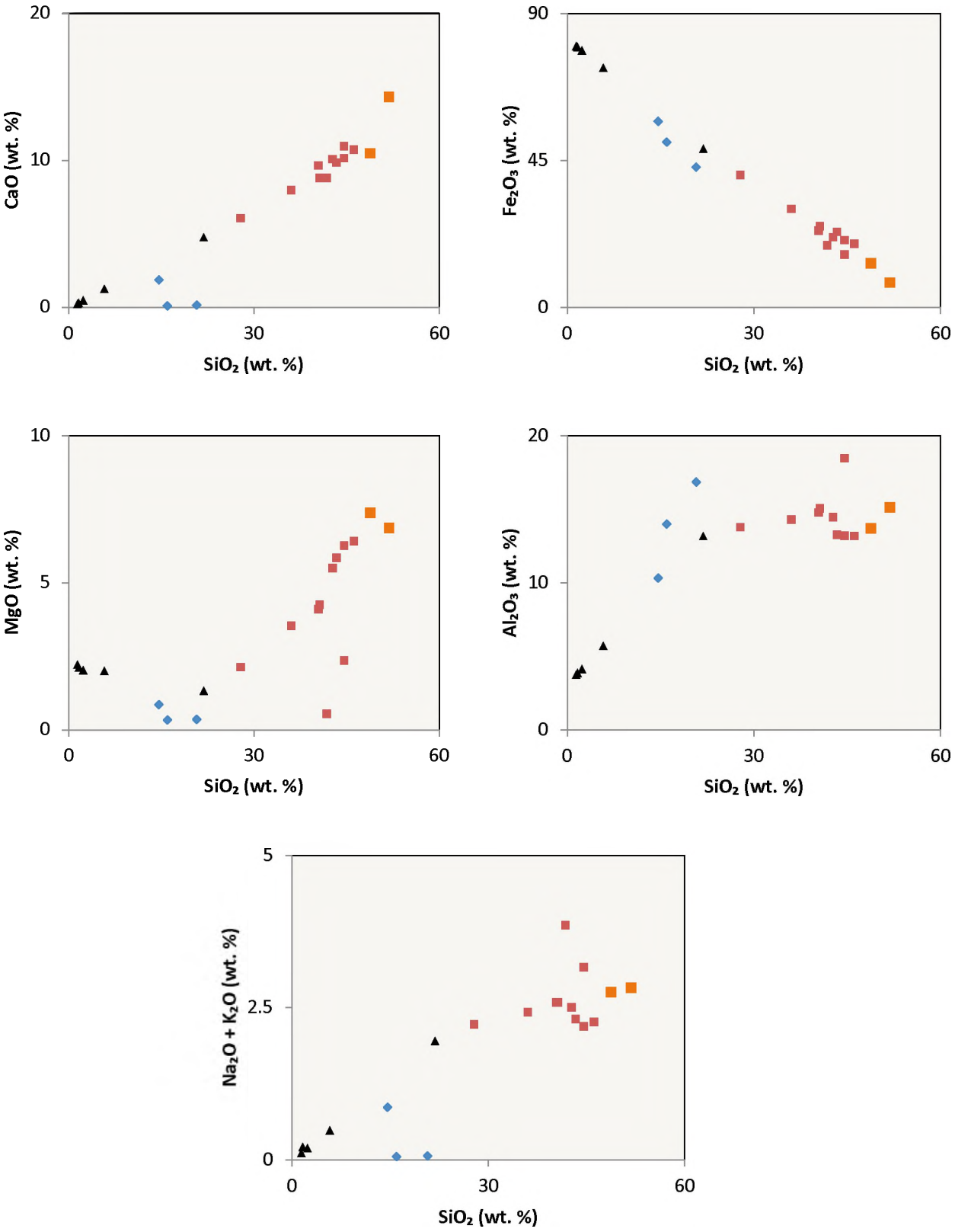

Figure 6.7: Major element variation diagrams for selected elements versus SiO_2. Symbols are the same as in Figure 6.1.

6.2.2. Major element stratigraphic variations

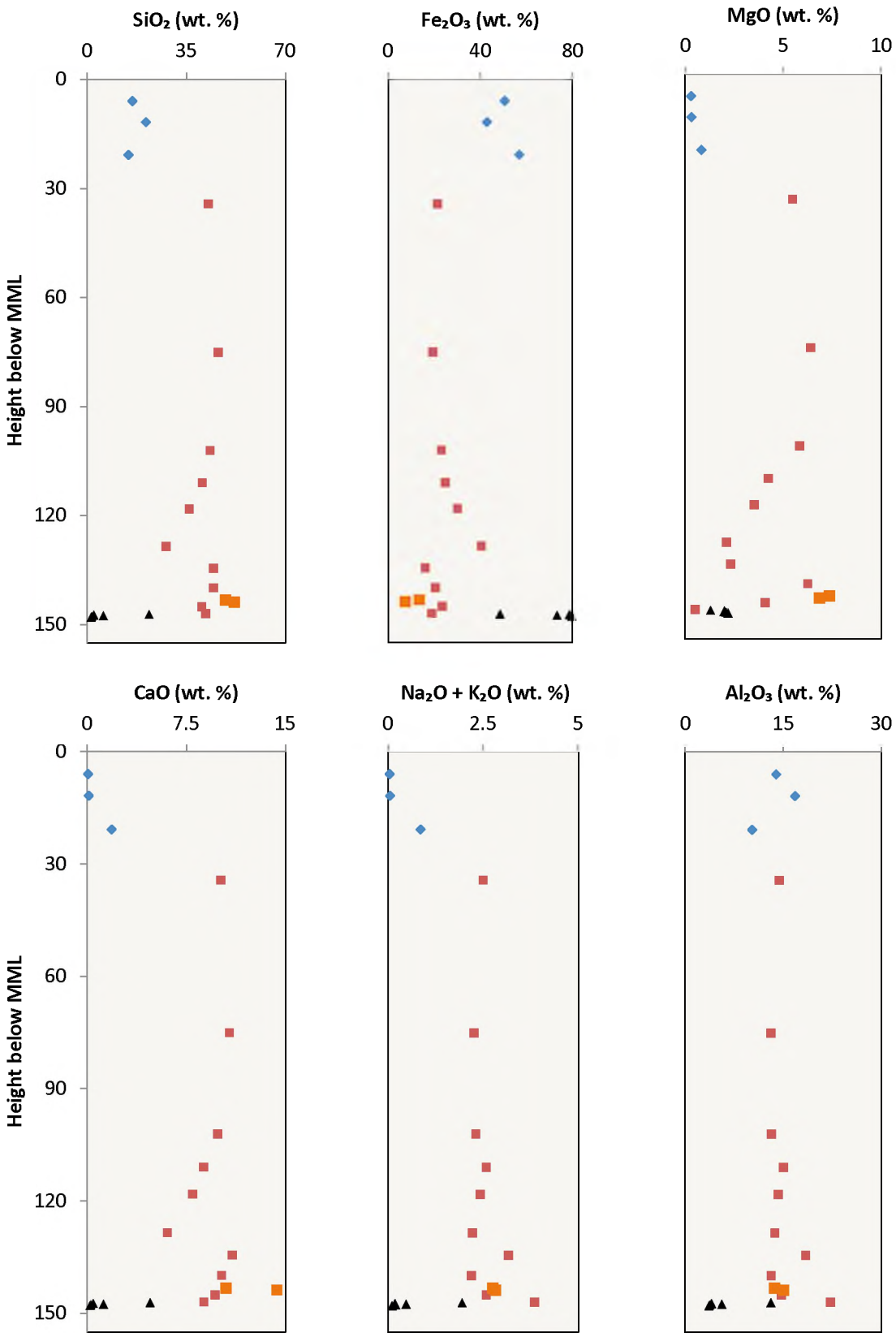

Figure 6.8: Major element stratigraphic variation (SiO_2, Fe_2O_3, MgO, CaO, Na_2O + K_2O and Al_2O_3) diagrams. Symbols are the same as in Figure 6.1.

Refer to Figure 6.9 for selected major and trace element ratios. Zr/Nb ratios decrease steadily up stratigraphy with ratios < 10 ppm (except for two outliers at 134.5 and 143.3 m respectively). Ce/Nd ratios increase from the base of the magnetite layer upwards over one metre, then decreases and remains steady over the entire section (with exception to one outlier in the weathered magnetite gabbro at 11.8 m where the ratio is extremely high, > 6 ppm). Fe_2O_3/TiO_2 ratios hover around 10 ppm for all disseminated magnetite gabbro samples. Ratios for layer magnetite and weathered magnetite gabbro samples could not be obtained (with exception of one sample, LS-1 at 6 m) as TiO_2 concentrations were above the detection limits for the method used. V/Zr ratios are significantly higher in the weathered magnetite gabbro samples (averaging 867 ppm) than in the fresh disseminated magnetite gabbro and layer magnetite samples. From the top of the magnetite layer, V/Zr ratios decrease rapidly upwards before a spiking at 141.1 and 131.8 m after which the ratios begin to decrease steadily upwards.

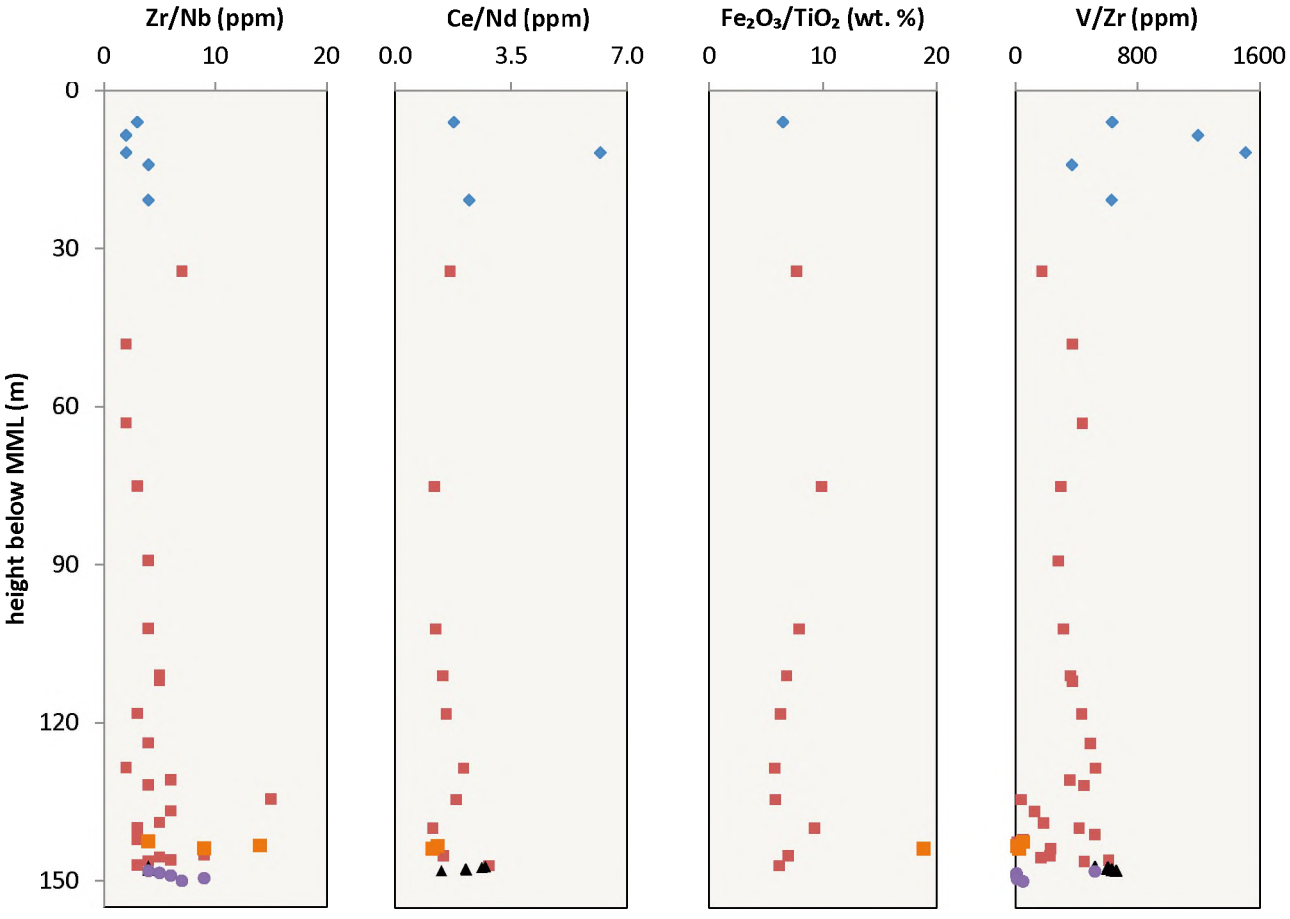

Figure 6.9: Selected major and trace element ratio stratigraphic variations. Note symbols are the same as outlined in Figure 6.1.

7. Discussion

7.1. Petrogenesis of the Upper Zone and Fe-Ti oxide ore layers

Whole-rock geochemistry is strongly controlled by the geochemistry of Fe-Ti oxides and cumulus silicate minerals in the sequence. This is evident as there is a strong negative correlation between total Fe (as Fe_2O_3) and SiO_2 (Figure 6.7). Nearly all Fe_2O_3 in the magnetite layer is in Ti-magnetite, while SiO_2 concentrations increase at the appearance of cumulus plagioclase and pyroxene in the gabbroic host rocks. Ti concentrations are generally above the analytical detection limit and cannot be quantified in the magnetite layer, therefore rendering it impossible to determine if there are actual high or low-Ti trends which could be responses to ilmenite formation.

Trace element variations through the magnetite layer (Figure 6.4) show highly compatible elements in magnetite (V, Nb, Co, Ni) increasing at the base of the layer and remaining constant throughout the layer until it grades into disseminated magnetite gabbro at the top. Cr, also highly compatible in magnetite (partition coefficient of 200 for Cr into magnetite as experimentally determined by Lindstrom- (1976) for basaltic liquids) shows a significantly different trend across the layer. Unlike the other compatible trace elements in magnetite, Cr shows a pronounced vertical depletion from the base (>7000 ppm) of the layer through to the graded top (<100 ppm). This is comparable to the data presented by McCarthy *et al.* (1985) for the MML, which they interpreted to be compatible with a layered melt model involving bottom crystallisation under conditions of a slow rate of supply of material to the crystallisation zone. McCarthy *et al.* (1985) also reported reversals in Cr contents above the MML in the disseminated magnetite gabbro, with small reversals up to 1400 and 1500 ppm Cr respectively. These reversals in Cr content are not evident in the rocks observed above this magnetite layer, possibly suggesting a more rapid supply of material to the crystallisation zone. The lack of a rapid depletion profile for other compatible trace elements in magnetite is interesting in itself, as this could suggest that the magnetite ore layer may not have formed by processes of early fractional crystallisation from a single magma pulse (as envisaged by Cawthorn and McCarthy, 1980).

Incompatible trace elements in magnetite (Sr, Cu, Rb, Ba) show a strong negative correlation with the compatible trace elements (Figure 6.2). Sr concentrations are highest in the

anorthosite footwall (>400 ppm) indicating the primary control of plagioclase crystallisation. Sr concentrations in disseminated magnetite gabbros are relatively constant throughout stratigraphy (averaging 250 ppm) matched with the relatively constant modal abundances of plagioclase (40-50 %). Zr, generally incompatible in magnetite, has high concentrations in the magnetite layer (> 20 ppm) while the disseminated magnetite gabbros have low concentrations (< 10 ppm). This could relate to two factors: (1) late crystallisation of magnetite preferentially incorporating incompatible elements remaining in the liquid, and (2) the cumulate nature of these rocks and loss of interstitial liquids.

The disseminated magnetite gabbroic rocks that have been subjected to extensive near-surface weathering show progressive loss of Si, Ca, Na, K, Mg and Sr (Figure 6.8). This is consistent with weathering primarily of silicates (plagioclase and clinopyroxene in particular) and their replacement by clay minerals, predominantly kaolinite (and hence no loss of Al). Magnetite remains largely unaffected by the weathering process with the exception of some hematisation around grain boundaries. There is no real loss of Fe_2O_3 or of elements compatible with magnetite (e.g., V, Ni, Co).

7.1.1. Microgabbro formation

Plagioclase An % averages An_{57} for microgabbro which is comparable to plagioclase occurring in the coarse-grained gabbroic host rocks (averaging An_{55}). Clinopyroxene compositions are also remarkably alike ($Mg\#_{clinopyroxene}$ of 66 for microgabbro and gabbroic host rocks). That, combined with the lack of any discordant relationships and also no noticeable chill effects with the coarser-grained gabbroic host rocks, suggests that it may actually represent a recrystallised portion of the coarse-grained gabbro and not a quenched melt. This is supported by the presence of triple-grain boundary junctions as a result of grain boundary migration during recrystallisation. This occurs when the system shifts toward a state of minimum interfacial energies between grain boundaries (Ragan, 1969). It could also simply suggest a fine-grained gabbroic portion which has been recrystallised. However, the presence of microgabbro may represent a portion of early injected magma which did not evolve at depth and may be characteristic of the parent magma to the UZ (See Chapter 7.1.5 for further discussion on this topic).

7.1.2. Evidence for variations in fO_2

Increases in fO_2 have been proposed as a mechanism for initiating magnetite crystallisation by various workers (Ulmer, 1969; Klemm *et al.* 1985; Ganino *et al.* 2008). Toplis and Carroll (1995) showed that Ti-magnetite-dominated oxide assemblages crystallise at high fO_2 conditions in excess of Fayalite-Magnetite-Quartz (FMQ), whereas those containing cumulus Ti-magnetite and ilmenite crystallise at fO_2 at FMQ. Therefore, the basal UZ magnetite layers and disseminated magnetite gabbroic host rocks must have crystallised at high fO_2 conditions considering cumulus ilmenite does not occur in the sequence. Ilmenite only occurs as a product of oxidation exsolution (Figure 4.4d-h) in the magnetite layer and never as a cumulus mineral phase, a feature von Gruenewaldt *et al.* (1985) believe probably originates from high-temperature Ti-magnetite via oxidation. This ilmenite is believed to be exsolved from Ti-magnetite by an exsolution-like process as a result of oxidation of the magnetite-ulvöspinel solid solution at temperatures above the magnetite-ulvöspinel solvus (von Gruenewaldt *et al.* 1985). The authors showed that there are distinct differences in exsolution textures between Ti-rich magnetite in the magnetite layers compared to those in the disseminated magnetite gabbroic host rocks, variations that can be attributed changes in fO_2 during crystallisation and sub-solidus oxidation. An experimental study conducted by Buddington and Lindsley (1964) also reveals that a high proportion of ilmenite lamellae within Ti-magnetite can be explained by simultaneous oxidation and exsolution of the magnetite-ulvöspinel solid solution. In addition, Buddington and Lindsley (1964) show that differing degrees of oxidation and diffusion of the magnetite-ulvöspinel solid solution can result in a variety of exsolution textures. Furthermore, they describe a systematic set of fabrics from oxide microtextures that result from increasing degrees of oxidation and diffusion: from (1) single-phase homogenous spinel; (2) trellis intergrowths of thin ilmenite lamellae in all sets of (111) planes; (3) sandwich intergrowths of thick ilmenite lamellae mainly in one set of (111) planes; (4) granules of ilmenite within magnetite (internal granular exsolution); to (5) granules or lamellae of ilmenite on external borders of magnetite (external granular exsolution). Data from these rocks in the basal UZ fits well with that observed by von Gruenewaldt *et al.* (1985). Magnetite layer samples typically show the array of exsolution features consistent with a high degree of oxidation (4-5) as described by Buddington and Lindsley (1964). Most common is internal granular ilmenite exsolutions

followed by external granular ilmenite exsolution (Figure 4.4e-h). This fits well with the assumption that higher fO_2 prevailed during formation of magnetite layers. In contrast, disseminated magnetite gabbros do not show internal or external granular ilmenite exsolution but rather lower oxidation degree microtextures. These are most commonly abundant cloth-textured ulvöspinel (Figure 4.4a-c) and less so trellis intergrowths of ilmenite (Figure 4.4f). Cloth-textured ulvöspinel is a true exsolution process resulting from a decrease in solubility of one component in the other with decreasing temperature (von Gruenewaldt *et al.* 1985). These differences can be related to variations in oxygen fugacity, sub-solidus oxidation, composition, and diffusion or a combination of these variables (von Gruenewaldt *et al.* 1985). Therefore, it can be concluded that the magnetite layer crystallised at relatively higher fO_2 conditions than the associated disseminated magnetite gabbros as indicated by the variation in magnetite exsolution microtextures.

7.1.3. Corona textures and reaction rim development

The development of coronas, reaction rims and symplectites are diagnostic features in these rocks, particularly of reactions occurring between Fe-Ti oxides and plagioclase. These textures are important to note as they indicate a change in the chemical and/or physical factors, as a result of a prograde or retrograde metamorphic event, the latter often associated with igneous cooling (Griffin and Heier, 1973; Mongkoltip and Ashworth, 1983). The formation temperatures of corona textures in gabbroic rocks have been estimated by various workers e.g. 580-880 °C (Acquafredda *et al.* 1992); 800 (± 30) °C (Cleason, 1998) and from experimental work 670-700 °C (Larikova and Zaraisky, 2009). Most workers agree that coronas form by subsolidus mineral reaction involving mass transfer by a fluid phase, however differing models have been proposed for the mechanism of ion diffusion (van Lamoen, 1979). Whether or not individual coronas formed as open or closed systems is also a matter of debate and will be discussed later.

The first corona texture in question is the occurrence of fine-grained olivine (average composition Fo_{63}) developed at the interface between Fe-Ti oxides and plagioclase (Figure 4.6a) near the top of the massive magnetite layer (sample BS-3 and BS-5 in particular). This texture is prominent within the ore layer but does not occur throughout the disseminated

magnetite gabbroic rocks. Reactions involving plagioclase and magnetite would require Mg and Fe to produce olivine yet neither magnetite nor plagioclase contain sufficient Mg to produce olivine of this nature from this type of reaction. Fe is easily sourced from the reaction involving magnetite or ilmenite but Mg must be sourced externally as clinopyroxene and orthopyroxene in these rocks are not directly involved in the breakdown reaction producing olivine. This leads to the assumption that these reactions occur in an open system whereby Mg is externally derived. Olivine as reaction products are also observed as late stage reaction textures in the Skaergaard intrusion (Holness *et al.* 2011). Monocrystalline olivine reaction rims at the grain boundary contacts between plagioclase and magnetite averages Fo_{57} for the Skaergaard intrusion, in comparison to Fo_{63} in the rocks in this study. Olivine as a reaction product is also seen in hydrous partial melting experiments at high temperatures (980 °C) for gabbroic compositions (Koepke *et al.* 2004). Holness *et al.* (2011) attributed poly-crystalline olivine rims as a result of decreasing fO_2 in the interstitial liquid (as a result of Fe-Ti oxide crystallisation) and destabilisation of magnetite and pyroxene. This seems like a plausible model for the basal UZ of the BIC as the olivine rims occur near the top of the Fe-Ti oxide ore layer, where fO_2 is now lower (assuming high levels of fO_2 result in magnetite crystallisation and monominerallic ore layer formation). Therefore, the interstitial liquid might be high enough in Mg abundance to make olivine of this nature, if there has been sufficient destabilisation of pyroxenes in the underlying sequence. So while a closed system, high-temperature olivine-forming reaction is not out of the question, there is no obvious basis to contradict a sub-solidus cooling reaction associated with an Fe- and Mg-enriched fluid.

Symplectic intergrowths are relatively ubiquitous throughout the disseminated magnetite gabbroic rocks, predominantly at the interface between Fe-Ti oxide and plagioclase crystals (Figure 4.6b,d). Van Lamoen (1979) studied corona textures developed between opaque-oxides and plagioclase for olivine gabbros and ascribed these to developing essentially as allochemical systems open to mass transfer by an intergranular fluid phase. Multiple coronas of an inner orthopyroxene + plagioclase symplectite mantled by an outer hydrous shell (hornblende particularly) have been described by Turner & Stüwe (1992) for olivine gabbros. This feature is visible in these rocks, except in this case plagioclase and magnetite react to form plagioclase + orthopyroxene symplectites which are mantled by a hydrous Fe-

rich chlorite shell (rather than hornblende). There are also examples where biotite occurs as the inner shell and orthopyroxene + plagioclase symplectites encase it (Figure 4.6e,f). Turner and Stüwe (1992) argue that symplectites growing into or encroaching on plagioclase provides evidence for high-temperature sub-solidus formation of symplectites. This is a feature visible in these rocks (Figure 4.7c-e). Various authors believe that an open-system reaction model be proposed for opaque oxides-plagioclase coronas (Starmer, 1969; Whitney & McLelland, 1973). Evidence for this is from observations that plagioclase may show complete replacement by a symplectite, with no significant alteration of the surrounding opaque oxides (Turner & Stüwe, 1992). De Haas *et al.* (2002) also propose an entirely late-stage, magmatic origin of symplectites (in that case orthopyroxene + spinel symplectites).

It is proposed here that the orthopyroxene + plagioclase symplectite intergrowths in these rocks formed as a result of sub-solidus cooling forming an exchange between Fe-Ti oxides (predominantly magnetite) and plagioclase, aided by the presence of an Fe and Mg-rich fluid phase (which would also help explain the formation of forsteritic olivine coronas discussed previously) reacting with plagioclase in particular. Magnetite may not have been involved as a reactant due to the low Ti content in symplectites and since Ti is not easily transported by aqueous fluids (Kogiso *et al.* 1997). Therefore, magnetite may be acting as a catalyst to the reaction instead, with/without exchange of Ti.

Biotite rims between plagioclase and magnetite (and bordering symplectites) can be ascribed to the reaction between magnetite and late-stage residual fluids (Morse, 1979; Parsons, 1980). Fe-rich chlorite coronas rimming plagioclase and plagioclase + orthopyroxene symplectites can also be supported by the presence of an Fe- and Mg enriched late fluid phase present during sub-solidus cooling. However, this reaction may be taking place under relatively cooler conditions than that of symplectite formation as chlorite is a common secondary mineral produced during cooling.

7.1.4. Suggested parent magma compositions to the Upper Zone

Identification of marginal zone rocks and sills in the floor of the western and eastern limbs has led to the recognition of several magma types (Cawthorn, 1996), a few which have been

suggested as magmas parental to the various zones of the BIC. The correlation of magma types with certain zones of the layered sequence has been done in two different ways: Cawthorn *et al.* (1981) used mineralogy and chemistry of floor rock sills, while Sharpe (1981) used geographical location of marginal rocks and their proximity to the different zones of the layered sequence. On the basis of this, an assortment of magma types have been proposed for the various sequences to the BIC. Those proposed as parent magmas to the UZ will be reviewed in this chapter.

Table 7.1: Proposed parent magmas to the UZ (1 and 2) as well as microgabbro compositions from this study (3 and 4).

	1	2	3	4
SiO_2	49.32	48.5	51.86	48.79
TiO_2	0.81	0.75	0.4	0.62
Al_2O_3	15.67	16.49	15.11	13.69
FeO(T)	12.77	12.41	7.56	13.5
MnO	0.19	0.19	0.17	0.25
MgO	6.08	7.57	6.86	7.37
CaO	10.83	11.15	14.32	10.49
Na_2O	2.94	2.17	2.58	2.45
K_2O	0.25	0.14	0.24	0.3
P_2O_5	0.07	0.18	0.009	0.009

1- Upper Zone proposed parent magma (Davies and Cawthorn, 1984)
2- Upper Critical Zone B2 proposed parent magma (Sharpe, 1981)
3- Microgabbro sample from this study (Sample P-2)
4- Microgabbro sample from this study (Sample P-1)

On the basis of its relatively homogenous Sr-isotopic composition data, the evolution of the UZ is believed to be as a result of single pulse of isotopically homogenous magma which thoroughly blended before crystallisation (Kruger *et al.* 1987). Davies and Cawthorn (1984) proposed a composition to this parent magma which intruded at the level of the Pyroxenite Marker. This magma is very similar in composition to the proposed parent magma to the UCZ of Sharpe (1981). This magma is similar in trace element and isotopic composition to a tholeiitic B2-type marginal sill, the magma proposed as the CuZ parent. Interestingly, microgabbro samples (P-1 in particular) are relatively similar in major element composition

to the parent magmas proposed by Davies and Cawthorn (1984) and Sharpe (1981). The only exception is the extremely low abundance of P_2O_5 and lower Al_2O_3 content in the P-1 microgabbro sample. The sample also shows similarly flat REE profiles (Figure 6.5d) to that of an average picrite (after Li *et al.* 2010) and high-Ti basalt (after Xiao *et al.* 2004) from the ELIP, yet with lower REE abundances. Sample P-1 could indicate an earlier pulse of magma which did not evolve at depth and signifies the early stages of the UZ, or it simply represents a recrystallised portion of the gabbroic host rocks. Whether or not this microgabbro can be considered as parental to the UZ is uncertain and warrants further study.

7.2. Fe-Ti oxide ore layer formation – model evaluation

Any genetic model for Ti-magnetite layer formation needs to explain the mechanisms that are responsible for the precipitation of copious amounts of Ti-magnetite as well as the development of ore-rich layers (Reynolds, 1985a) and their silicate-rich host rocks. This is done on the basis of their mineralogical, petrological and geochemical characteristics. Various models have been devised by numerous workers, all which pose their own problems and thus further investigation. The models evaluated here includes: increases in fO_2; liquid immiscibility; magma mixing events; changes in pressure, or a combination of the above mentioned processes.

7.2.1. Increases in fO_2

Ulmer (1969) and Klemm *et al.* (1985) have suggested that an increase in fO_2 may initiate magnetite crystallisation, a mechanism that does not require a change in the composition of the magma. This would mean that plagioclase compositions above and below a magnetite layer should show no significant compositional change (Cawthorn and Ashwal, 2009), as they might expect to show in a magma mixing-type model. This is consistent with the data found in this study as plagioclase compositions below the magnetite layer (An_{67}) are relatively similar to compositions of plagioclase above the layer (An_{69}). However, compositions of some trapped plagioclase grains in the magnetite layer display significantly higher An %, up to An_{74} (Figure 5.1). This reversal in An % of plagioclase in the magnetite

layer is coupled with an increase in Mg# of clinopyroxene at the same level in the layer (Figure 5.1). H_2O content of a basaltic melt is enriched during early crystallisation of anhydrous phases (Howarth, 2013) and this could result in a change in An % of plagioclase. Thus evidence for late crystallisation of magnetite in the presence of H_2O could be plausible, which could significantly increase the fO_2 of the magma and cause the high An % of plagioclase in the magnetite layer. However, mineralogy and textural features, predominantly the lack of any primary hydrous phases such as amphibole, suggests this is not the case. However, high An content in plagioclase and stability of magnetite, olivine and clinopyroxene are all enhanced by higher H_2O contents (with or without amphibole stability).

Other evidence for increases in fO_2 can come from the enrichment of minor elements such as Ti, Mg, Al and Si in magnetite hosted in magnetite layers relative to their disseminated concentrations in associated magnetite gabbros (Klemm *et al.* 1985). The authors ascribed these changes in minor element abundances to magnetite crystallising under conditions of disequilibrium with the magma, by spontaneous nucleation and rapid crystallisation. The data in this study are not consistent with the findings of Klemm *et al.* (1985) in the sense that Si and Al in magnetite hosted in the magnetite layer is not necessarily higher than that in the associated disseminated magnetite gabbros. Mg content is, however higher in magnetite hosted in the magnetite layer compared to that of magnetite in the gabbroic rocks (see Figure 5.6, for example). Experimental data of Irving (1978) show that V concentration within crystallising magnetite is very strictly controlled by the partition coefficient and also significantly by the fO_2. He also established that V content of magnetite decreases with increasing fO_2, which supports the crystallisation of magnetite layers under conditions of higher fO_2. This is also supported by experimental studies done by Toplis and Corgne (2002) stating that fO_2 controls the V content of magnetite, with the maximum value of *D*v into magnetite occurring at ~QFM. This is broadly consistent with the findings of this study as disseminated magnetite is, on average, higher in V concentration (averaging 1.13 wt. %) in comparison to the magnetite layer equivalents (averaging. 1.05 wt. %). This is then consistent with other authors' models of magnetite layer crystallisation under conditions of higher fO_2 in the magma. Further evidence for increases in fO_2 is found in the form of varying oxidation exsolution textures in magnetite layers and disseminated magnetite

gabbros (as discussed in section 7.1.3). For example, the presence of internal and external granular exsolutions of ilmenite in the magnetite layer is not present in the disseminated magnetite gabbros, suggesting higher degrees of oxidation in the magnetite layer than in the associated disseminated magnetite gabbroic rocks.

The problem with the increasing fO_2 model is actually discovering the exact mechanism responsible for suddenly introducing large amounts of oxygen into the system. Another issue is exactly how this mechanism causes multiple magnetite layer formation i.e. episodic increases in fO_2 switching on and off. Increasing fO_2 could possibly occur as a result of diffusion of volatiles through the floor of the chamber (as proposed by Klemm *et al.* 1985) or by some other unknown internal/external mechanism which remains to be solved. The final problem is whether or not this mechanism could result in magnetite layers being distributed over such large lateral extents. Whether or not such a mechanism could be a chamber-wide feature is unclear and up to further investigation.

7.2.2. Liquid immiscibility

The separation of dense, Fe-rich immiscible liquids resulting in monomineralic magnetite layers is a model proposed by Bateman (1951) and Reynolds (1985a). This model is also proposed by Zhou *et al.* (2005) for the formation of Fe-Ti-V oxide ore layers in the Panzhihua intrusion, SW China (Figure 7.4) and for late-stage Fe enrichment trends in the Skaergaard intrusion (Jakobsen *et al.* 2011). However, experimental data on Fe-rich immiscible liquids (Philpotts and Doyle, 1983; Jakobsen *et al.* 2005; Veksler *et al.* 2007) show that these liquids only contain a maximum of 28 % total FeO, compared to the conjugate silicate-dominated liquids consisting of 10-15 % total FeO (Philpotts and Doyle, 1983). This means that monominerallic magnetite (with ca. 70-80 wt. % Fe_2O_3) layers do not approximate to the composition of the observed Fe-rich immiscible liquids. Separation of magnetite from an associated Fe-rich silicate phase would therefore also be required to produce such monominerallic magnetite layers. Another feature that argues against this model is the nature of the basal contacts of magnetite layers with the footwall rocks (anorthosite in this case). The basal contacts of magnetite layers in the UZ of the BIC are typically distinctly

sharp and planar, whereas a high density Fe-rich liquid should be expected to penetrate downwards into the underlying crystal mush, producing an irregular basal contact (Cawthorn, 1996). In this study, the nature of the basal contact of the magnetite layer with the footwall anorthosite is irregular (Figure 3.2a), supporting that this could be a dense, immiscible liquid penetrating into the crystal mush of plagioclase grains below. Nonetheless, Cawthorn and Ashwal (2009) suggest that the graded tops of the magnetite layers, which show an increase in plagioclase proportion from 0 to 80 %, should not show such a gradual change at the top of an extremely dense Fe-rich liquid layer (yet gradual upper contacts are distinct features of most magnetite layers in the UZ of the BIC).

In addition, Fe-rich immiscible liquids are characterised by high P_2O_5 contents, which should result in the relationship of magnetite and apatite in a proportion of approximately 2:1 (Philpotts, 1967). Furthermore, Watson (1976) states that Fe-rich immiscible liquids strongly partition phosphorus relative to the conjugate silicate magma (by a factor of more than 10). Now, since the lowermost magnetite layers (including the magnetite layer in this study) do not contain any apatite at all (i.e. extremely low P_2O_5 contents), and apatite is only present above the level of cumulus apatite appearance in the silicate-rich rocks of the UZ, again raises questions as to the involvement of immiscible Fe-rich liquids as the mechanism for producing the oxide-rich ore layers in the UZ of the BIC.

7.2.3. Magma mixing

From theoretical studies, Irvine and Sharpe (1986) concluded that mixing of magmas of different compositions is a feasible mechanism to form chromite and magnetite layers, a model supported by Merkle and von Gruenewaldt (1986) and Harney *et al.* (1990) for magnetite layers in the UZ of the BIC. Kruger and Smart (1987) as well as Harney *et al.* (1990, 1996) suggest that a resident magma column may be internally stratified and that the collapse of two or more density stratified liquid layers may result in a magma mixing event. Addition of new magma could also trigger the formation of magnetite layers, assuming the magma was of course magnetite-saturated. Mineral compositional data, plagioclase An content and pyroxene Mg# in particular, provides evidence for magma mixing events in such

cases. For example, if the composition of plagioclase above a magnetite layer is dissimilar to the composition of plagioclase below the layer, this could suggest that there was addition of magma (Cawthorn and Ashwal, 2009). If any mixing occurred with a less differentiated magma there would be an expected reversal in An content of plagioclase. Namur *et al.* (2010) also show that mixing between resident and primitive magmas can produce a hybrid melt with higher Mg/Fe and Ca/Na content, which should result in concurrent increases in the Mg# of pyroxene and An content of plagioclase.

Data from this study show that there is a small reversal in An % of plagioclase in the magnetite layer, from An_{67} to An_{72}, before shifting back to slowly declining values throughout the disseminated magnetite gabbroic rocks (Figure 7.1). This is coupled with a reversal in Mg# of clinopyroxene near the base of the magnetite layer, Mg# 74, which then shows a constant decline upwards throughout the disseminated magnetite gabbroic rocks (Figure 7.1). Compositional data from Tegner *et al.* (2006) across different magnetite layers showed that there is a systematic up-section decrease in An content of plagioclase, while Harney *et al.* (1996) showed that there is no change in An content of plagioclase above and below two sections of the MML. Data in this study show that the reversals in An % and Mg# of clinopyroxene occur in the magnetite layer, while above the layer there are constantly declining values (but values that are similar below the magnetite layer). This is consistent with a detailed study done by Ashwal *et al.* (2005) in the northern limb, explaining that reversals in An content of plagioclase and Mg# of clinopyroxene can be attributed to magma recharge and mixing processes.

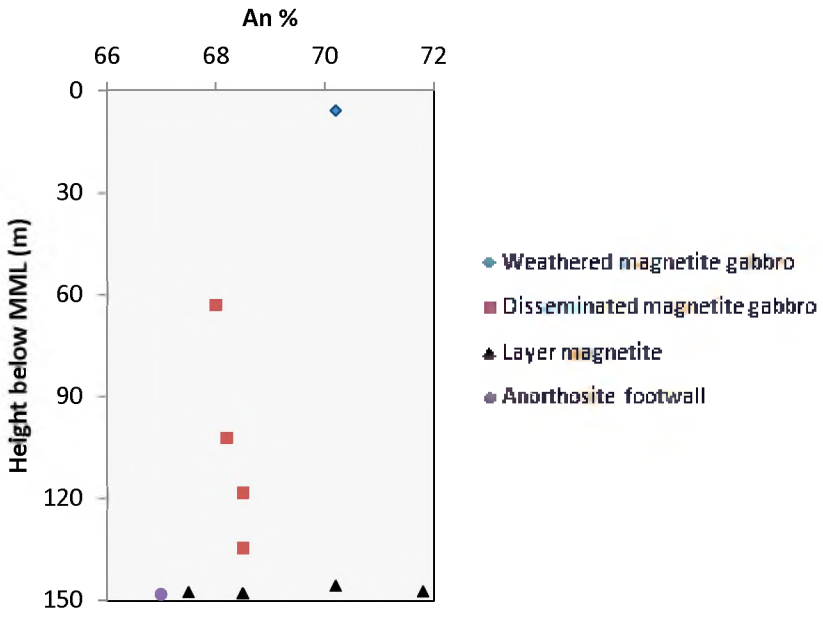

Figure 7.1: Average An % variation in plagioclase grains throughout different lithologies in the sampled sequence.

Harney and von Gruenewaldt (1995) used cyclic variations in whole-rock geochemistry, changes in PGE patterns, the Sr content of plagioclase as well as the composition of olivine and pentlandite to determine that magnetite layers from the upper part of the UZ formed as a response to magma mixing events. They attributed this either to the breakdown of density stratified liquid layers or via an influx of small volumes of new magma. The rocks in this study do show discrete cyclicity in whole-rock geochemistry. There is a clear differentiation cycle from the base of the magnetite layer upwards until 128.5 m (sample OHSZ-3) where another differentiation cycle seems to commence (Figure 6.8). This is clearly defined by the SiO_2, Fe_2O_3 and CaO whole-rock data showing the cyclicity which can be defined by processes of magma mixing throughout the chamber. These variations in geochemistry do not necessarily represent new pulse of magma (as shown by the An content and Mg# of clinopyroxene) but could represent magma mixing as a result of the convective overturn within a stratified magma chamber.

Cawthorn and Ashwal (2009) believe that the matches in compositions of plagioclase above and below most of the magnetite layers in the UZ (16 layers) suggests that magma addition is not likely to be the common mechanism for magnetite layer formation and that internal processes are more likely responsible for this. These internal processes may be a change in fO_2 or pressure changes in the magma chamber (as discussed below), or a combination of both.

7.2.4. Pressure changes

As with the proposal that chromite layers formed as a result of an increases in pressure, such a mechanism has also been proposed for the formation of magnetite layers in the BIC by Cawthorn and McCarthy (1980). These authors believe that chemical and gravitative settling processes alone cannot account for the liquid lying in the magnetite only phase of crystallisation. They do, however, ascribe external processes as the mechanism for creating the phase boundary shift into magnetite crystallisation, such as external tectonic events. Cameron (1977) also appealed to changes in pressure to shift the phase boundaries to

produce the monominerallic layering (particularly chromite) in the CZ, while Lipin (1993) envisaged the same process for formation of chromite layers in the Stillwater Complex, Montana, USA (Figure 7.2).

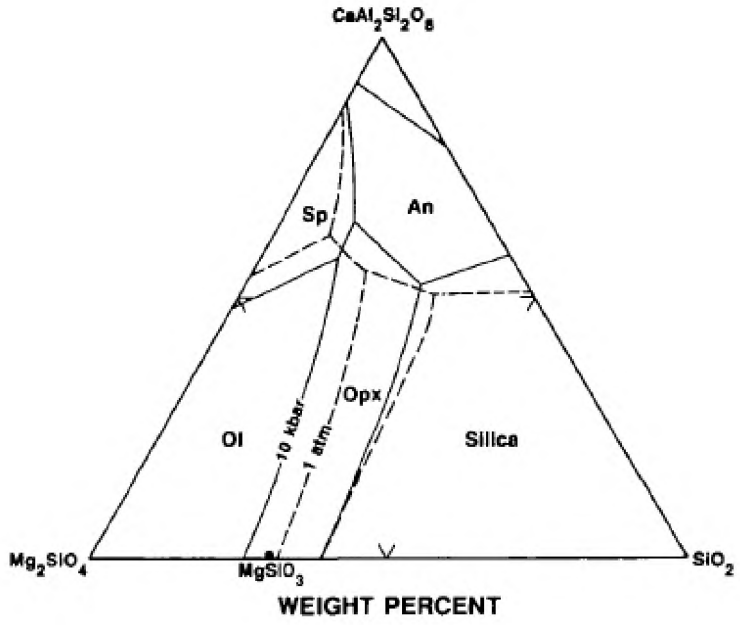

Figure 7.2: Liquidus relations in the Mg_2SiO_4-$CaAl_2Si_2O_8$-SiO_2 system at 1 atm and 10 kbar, showing the shift in the boundary curves with an increase in pressure resulting in spinel (chromite) formation (adopted after Lipin, 1993).

Magnetite crystallisation or magnetite-plagioclase cotectic proportions of crystallisation may result in a magma no longer being saturated in pyroxene (as seen by the lower abundances of pyroxene in comparison to magnetite and plagioclase in these rocks). The advantage of a pressure change mechanism is that it has a practically instantaneous transmission throughout the entire liquid (Cawthorn and McCarthy, 1980). This model then also allows for the incredible lateral distances over which continuous, individual magnetite layers occur (as well as the consistent thicknesses, partings and contact relationships). However, it has been suggested that pressure change is problematic as an explanation (Hatton, 1984) because the exact mechanisms for producing such a pressure change is unknown. It is also difficult ascertain what magnitude of pressure change is required to shift the phase boundaries into magnetite-only crystallisation (as shown by Lipin, 1993). Whether or not this is a feasible model to explain the shift to magnetite-only crystallisation is uncertain and up to further research and debate.

7.3. Comparisons to Panzhihua intrusion

The Panzhihua intrusion is a ±260 Ma old layered mafic intrusion which is one of the suites of intrusions related to the ELIP in SW China (Howarth and Prevec, 2013). This sill-like body hosts giant Fe-Ti-V oxide deposits with 1333 million tons of ore reserves (Zhou *et al.* 2004). The intrusion consists of a Marginal Zone of fine-grained hornblende-bearing gabbro and olivine gabbro, a Lower and Middle Zone consisting of layered gabbro composed of cumulate clinopyroxene, plagioclase and olivine, an Upper Zone consisting predominantly of leucogabbro composed of plagioclase and pyroxene with minor olivine, as well as a carbonate footwall (Zhou *et al.* 2004). The Fe-Ti oxide ore occurs as layers and lenses within the gabbro and are primarily hosted in the lower portion of the intrusion (Zhou *et al.* 2004). One of these layers is a large (±60 m thick) Fe-Ti-V oxide ore layer near the base of the intrusion (e.g. Howarth and Prevec, 2013). The Panzhihua intrusion is believed to form as an open system style magma chamber with at least three injections of magma (Pang *et al.* 2009). Zhou *et al.* (2005) suggest that Fe-Ti oxide ore bodies formed by late-stage crystallisation of V-rich titanomagnetite from an immiscible oxide liquid in a fluid-rich environment.

In comparison to the Fe-Ti oxide ore layers in the BIC, those in the Panzhihua intrusion display significant disequilibrium and silicate consumption by Fe-Ti oxides (Howarth and Prevec, 2013). These typically display plagioclase laths which have resorption textures and embayed grain margins, continuous corona rims of amphibole and/or olivine reaction rims. In light of these textures and parent crystallisation modelling at varying fO_2 and H_2O contents, Howarth and Prevec (2013) interpreted that the formation of Fe-Ti oxide ore layers in the Panzhihua intrusion are a result of the intrusion of H_2O-rich and Ti-magnetite crystal-rich magma (Figure 7.3).

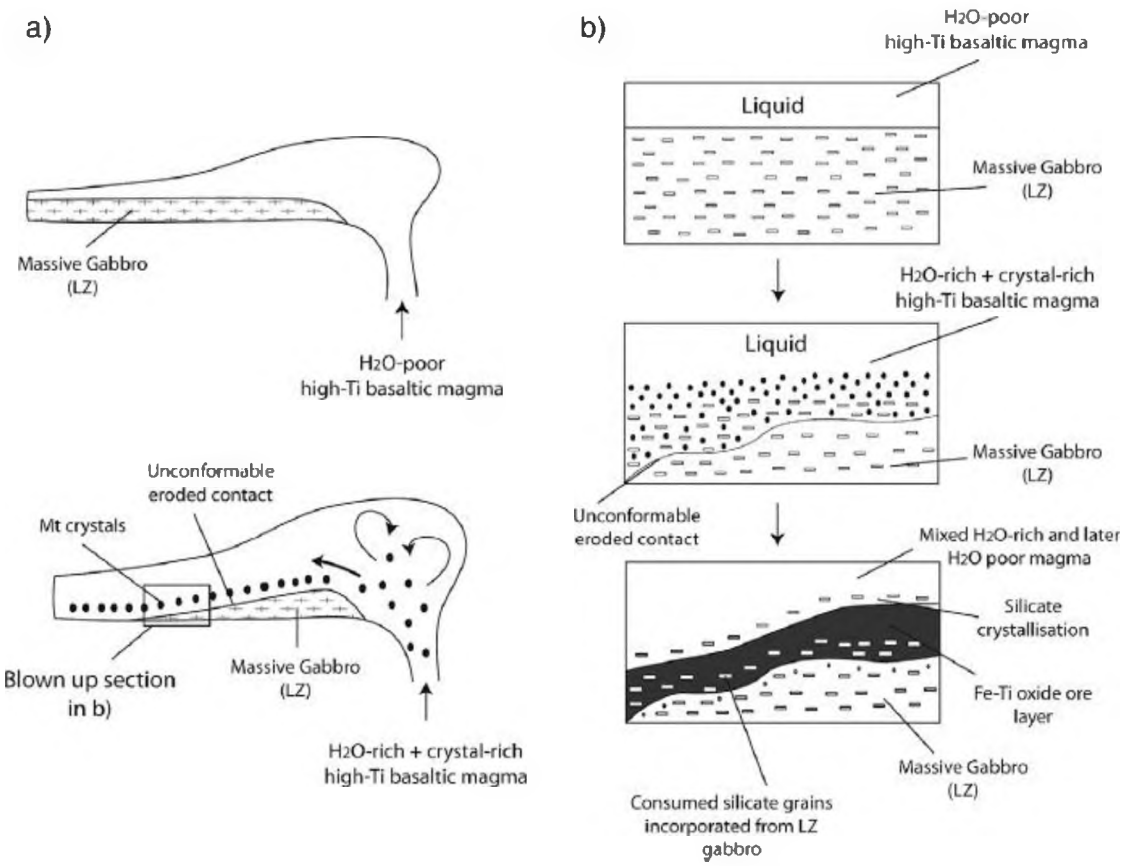

Figure 7.3: Simplified schematic illustration depicting the proposed model for the Fe-Ti oxide ore formation in the Panzhihua intrusion, SW China (adopted after Howarth and Prevec, 2013).

Zhou *et al.* (2005) agree that these textural relationships strongly support crystallisation of Fe-Ti oxides from an oxide melt that invaded a silicate crystal mush. However, their model also suggests that these melts formed as immiscible liquids (Figure 7.4) within the magma chamber and then settled to the bottom of the chamber, where they accumulated. However, the exact mechanism from which an immiscible melt formed from an evolved Fe-Ti-rich mafic magma is uncertain, however, the authors propose either mineral fractionation, magma mixing, abrupt changes in fO_2, and/or introduction of fluids (Zhou *et al.* 2005).

Liquid immiscibility is also a model described for the formation of Fe-Ti oxide ore layers in the BIC (Reynolds, 1985a) but as discussed in 7.1.6.2, this model has its problems and there is much uncertainty surrounding liquid immiscibility as a mechanism for Fe-Ti oxide ore layer formation. The increases in fO_2 in the Panzhihua intrusion can be accounted for by

significant CO_2 degassing of the footwall carbonates and thus significantly increasing the fO_2 of the magma (Ganino *et al.* 2008). Simple models of early equilibrium crystallisation and fractionation of Fe-Ti oxides to form these ore bodies (as proposed for Fe-Ti oxide ore layers in the BIC) cannot account for the evidence for variation in fO_2 and silicate disequilibrium in the Panzhihua intrusion. However, the CO_2 degassing along with intrusion of H_2O-rich magma into a crystallising magma chamber can account for both the increase in fO_2 and silicate disequilibrium textures (as well as the abundance of hydrous minerals) seen in the Fe-Ti oxide ore layers in the Panzhihua intrusion (Howarth and Prevec, 2013). The involvement of fluids is no doubt of vital importance to the formation of Fe-Ti oxides in the Panzhihua intrusion. The Fe-Ti oxides in the BIC do not necessarily require introduction of fluids to be present in their formation, thus making this the distinct difference between the Fe-Ti oxide ore deposits of the BIC and the Panzhihua intrusion, accounted for by the mineralogical and textural differences.

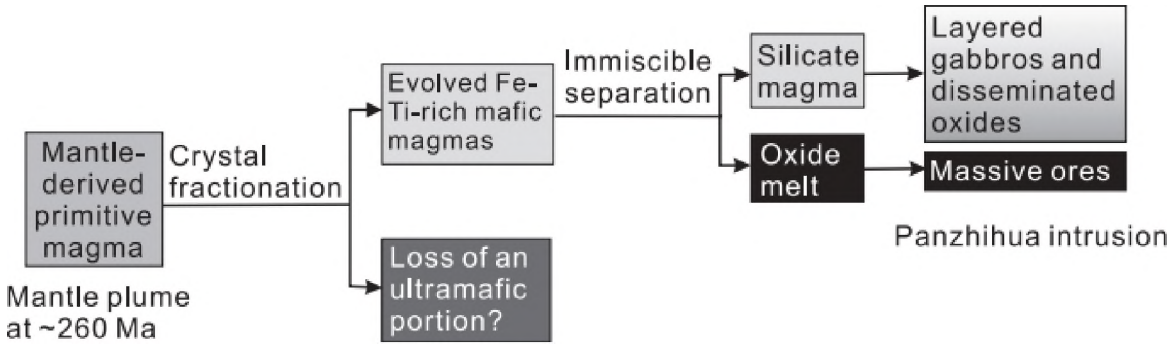

Figure 7.4: A schematic model for the formation of Fe-Ti oxide ore deposits in the Panzhihua gabbroic intrusion, SW China. Image adopted after Zhou *et al.* (2005).

7.4. Petrogenetic model

7.4.1. Fe-Ti oxide ore layer formation

The Fe-Ti oxide ore layer studied in this section of the basal UZ has distinctive features that need to be taken into account when deciphering a model that fits in the formation of such

magnetite layers. The following diagnostic features of the magnetite layer analysed need to be suitably addressed and accounted for:

1) Irregular basal contact with footwall anorthosite
2) Gradational upper contact with gabbroic host rocks
3) Higher Mg# of clinopyroxene inclusions in the magnetite layer in comparison to the disseminated magnetite gabbroic rocks
4) Higher An % of plagioclase in the magnetite layer in comparison to the disseminated magnetite gabbroic rocks
5) Rapid vertical depletion in Cr content from the base to the top of the ore layer

The consistency of An % above and below the magnetite ore layer suggests that new magma injection is not likely to be the mechanism responsible for layer formation. However, Higher An % of plagioclase and Mg# of clinopyroxene in the ore layer suggests that magma mixing processes may be operating during the formation of magnetite ore layers, which can be attributed to convective overturn within a stratified magma chamber (as detailed by Harney and von Gruenewaldt, 1995 for the MML). Magma mixing processes may have been operating yet this is not considered to be the crucial mechanism responsible for magnetite layer formation. In actual fact, the rapid vertical depletion of Cr from the base of the layer to the top somewhat discounts magma mixing as a model responsible for this. This rapid Cr profile is feature also described by McCarthy and Cawthorn (1985) for the MML. They propose a model of magma inhomogeneity and bottom crystallisation with a slow rate of material supply to the crystallisation surface. There is also no further Cr reversal throughout the disseminated magnetite gabbroic rocks above, suggesting no further cycles of magma mixing or discrete new pulses. However, other trace elements compatible with magnetite do not show the same rapid vertical depletion profiles that Cr does (Figure 6.4) but rather constant values throughout the magnetite layer, raising questions as to the inhomogeneity throughout magnetite layer formation.

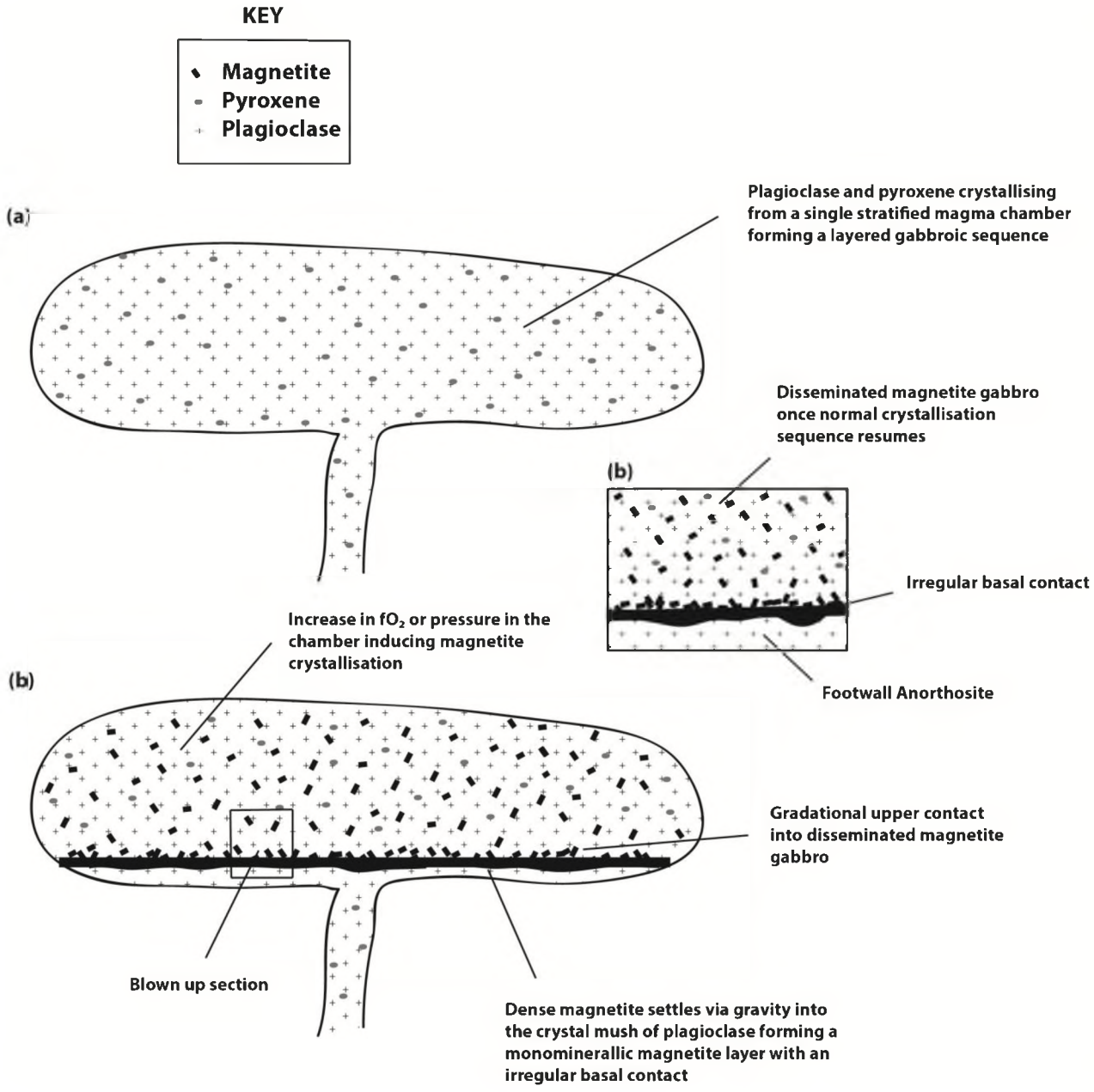

Figure 7.5: Simplified schematic illustration depicting a proposed petrogenetic model for the formation of Fe-Ti oxide ore layers in the basal UZ, BIC.

The irregular basal contact of the magnetite layer with the footwall anorthosite is consistent with gravity settling of magnetite into a crystal mush of less dense plagioclase. This feature is unlikely to be as a result of liquid immiscibility due to the problems already mentioned above in 7.2.2. with liquid immiscibility models. It is most likely that a magma undergoing silicate-dominated fractionation (crystallising cotectic proportions of plagioclase and pyroxene) switched to magnetite crystallisation as a result of an increase in fO_2 or a change

in pressure throughout the magma chamber (pressure increase possibly by external mechanisms). Consequently, gravity settling of dense magnetite to the floor of the chamber occurs, thus creating a monomineralic magnetite layer (with trapped inclusions of plagioclase and pyroxene). An increase in plagioclase content at the gradational top of the magnetite layer is as a result of the system then crystallising cotectic proportions of magnetite-plagioclase followed by magnetite-plagioclase-pyroxene and ultimately returning to the original gabbroic sequence of plagioclase-pyroxene once again. Episodic increases in fO_2 or a change in pressure throughout the magma chamber seem plausible models as these require no change in the magma chemistry (as seen by the An % of plagioclase above and below the magnetite layer). Fe-Ti oxide oxidation exsolution features throughout the magnetite layer also provide diagnostic evidence for increases in fO_2 in the magma chamber. Magma mixing may operate due to density inversions in the stratified liquid column once magnetite crystallisation begins, producing mineralogical breaks between fractionation cycles (Tegner *et al.* 2006). However, this is not considered to be the mechanism influential in the formation of individual magnetite layers but rather supplementing the formation of multiple Fe-Ti oxide ore layers throughout the UZ.

7.5. Implications for mineral extraction and V recovery

The magnetite layer analysed in this study (± 150 m below the MML), comprises > 90 % magnetite at the base and decreases to ± 50 % at the graded top, consisting of coarse-grained, well-annealed magnetite (Figure 4.1) with an average V_2O_3 grade of 1.05 wt. %. The ore grade is only slightly lower than that of the fresh disseminated magnetite gabbro but significantly lower than that of the weathered disseminated magnetite gabbro (Figure 7.6). The fresh disseminated magnetite gabbro (sample OFSZ-4 and OHSZ-5 in particular) located ± 30-147 m below the MML has an average V_2O_3 grade of 1.13 wt. %, but has a greater variation in terms of grade. These samples consist of ± 25-50 % disseminated magnetite intimately intergrown with plagioclase, clinopyroxene and orthopyroxene (Figure 4.2).

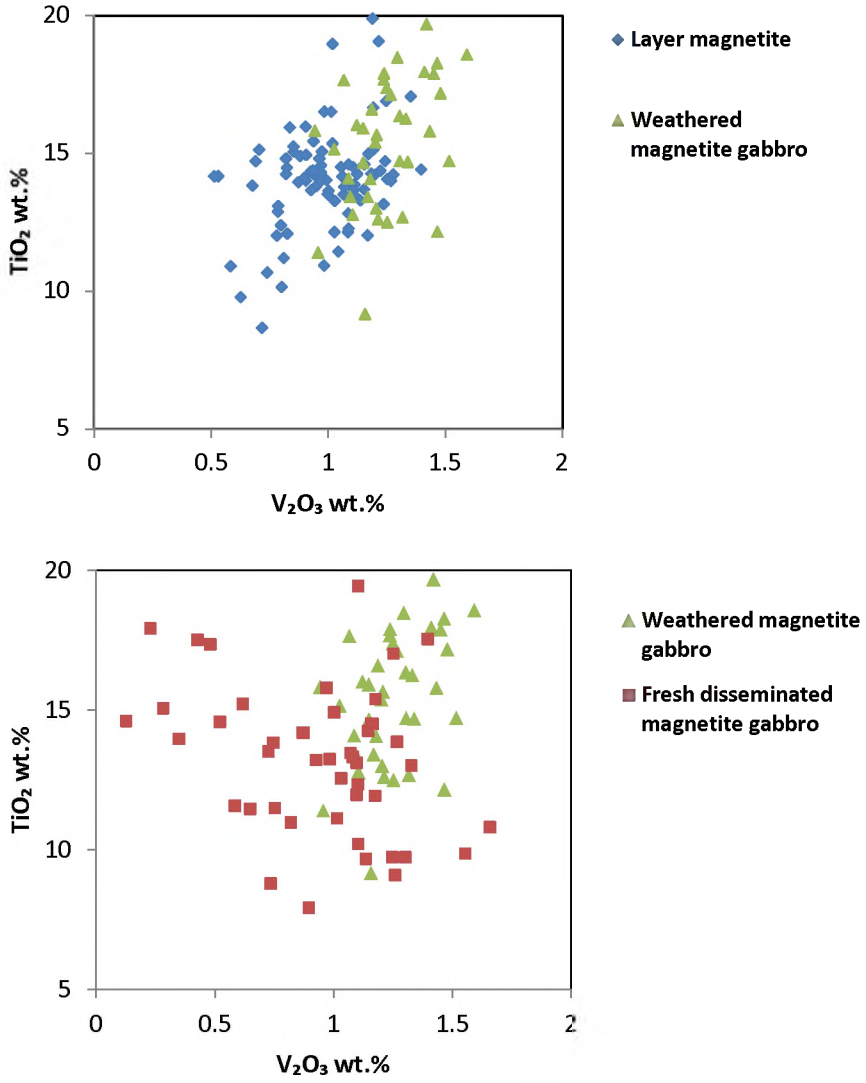

Figure 7.6: V_2O_3 versus TiO_2 of magnetite for different lithologies throughout the sequence. Note, V_2O_3 concentrations are reported as V^3+ occurs in magnetite, not V_2O_5.

The weathered disseminated magnetite gabbro, which is located from the surface of the borehole to ± 30 m in depth, has an average ore grade of 1.26 wt. % V_2O_3 (samples LS-5 and LS-1). These samples consist of extensively weathered plagioclase and pyroxene with relatively fresh disseminated magnetite.

Magnetite extraction from the fresh disseminated magnetite gabbro may be the most difficult as the oxides are more intimately intergrown with the silicates in comparison to the magnetite layer and weathered disseminated magnetite gabbroic rocks. This may bring

about problems with recovery if a roasting and leaching method is being used, as a higher degree of roasting may be required, and thus involving higher energy demands. However, if magnetic separation is the method used this becomes less of a problem, although high abundances of silicate waste will remain.

The Fe-Ti oxide ore layer has the highest abundance of magnetite and a similar in situ ore grade to that of the fresh disseminated magnetite gabbro. However, the lower modal abundance of silicates makes this a more attractive target in theory as there are limited amounts of other mineral phases to deal with in the recovery process. If the target is V or ferrovanadium, either way it becomes straight forward where there are less silicates in the system to separate out. The chief problem lies with the depth of the magnetite layer being 150 m below the surface as it may be less economically viable to target this layer as opposed to targeting the fresh disseminated magnetite gabbro as a result of this depth problem (they have the same in situ grade even though there is a smaller modal abundance of magnetite). The obvious option then lies in extracting magnetite from the extensively weathered magnetite gabbroic rocks near the surface. The silicates have already been converted to clay minerals, rendering them extremely less resistant than the primary silicates (plagioclase, clinopyroxene and orthopyroxene). This would result in a more efficient roasting and leaching/magnetic separation process. The fact that such high V_2O_3 grades occur in these is somewhat of an anomaly as V is essentially immobile during weathering (Habteselassie *et al.* 1996) limiting the possibility of ore upgrading. Either way it should be considered somewhat fortunate that such high ore grades occur so close to the surface and can allow for relatively easy mineral extraction. Concentrated ore grades may prove otherwise, however at an in situ grade level this would be the most suitable suggestion for mining.

Summary and Conclusions

Petrographic (textural and mineralogical) variation as well as major and trace element geochemical data are presented for the basal UZ section of the BIC. Data suggests a strong mineralogical control on whole-rock geochemistry by the presence of Fe-Ti oxides (magnetite in particular). Cr, highly compatible in magnetite, shows a pronounced vertical depletion from the base (>7000 ppm) of the magnetite layer through to the graded top (<100 ppm) which is interpreted to be compatible with a layered melt model involving bottom crystallisation under conditions of a slow rate of supply of material to the crystallisation zone. However, other trace elements compatible with magnetite (V, Nb, Co and Ni) do not show such a rapid vertical depletion profile, suggesting that the magnetite layer may not have formed by processes of early fractional crystallisation from a single magma pulse.

The development of coronas, reaction rims and symplectites are diagnostic features in these rocks, particularly of reactions occurring between Fe-Ti oxides and plagioclase. Fine-grained olivine (Fo_{63}) developed at the interface between magnetite and plagioclase is interpreted to be a product of a reaction between these two minerals with Mg been sourced externally, inferring an open system reaction. Orthopyroxene + plagioclase symplectite intergrowths formed as a result of sub-solidus cooling forming an exchange between Fe-Ti oxides (predominantly magnetite) and plagioclase, aided by the presence of an Fe and Mg-rich fluid phase reacting with plagioclase in particular.

The consistency of An content above and below the magnetite layer suggests that it is also unlikely that new magma injection is the mechanism responsible for magnetite layer formation. However, higher An % of plagioclase and Mg# of clinopyroxene within the magnetite layer suggests magma mixing processes may be operating, most likely due to convective overturn within the stratified magma chamber. Liquid immiscibility is also unlikely to be the mechanism responsible for magnetite layer formation because magnetite layers do not approximate to the composition of the observed Fe-rich immiscible liquids performed in experimental studies and contain no apatite at all (i.e. extremely low P_2O_5 contents), a feature expected to be observed in Fe-rich immiscible liquids. It is postulated that a magma undergoing silicate-dominated fractionation (crystallising cotectic proportions

of plagioclase and pyroxene) switched to magnetite crystallisation as a result of an increase in fO_2 or a change in pressure throughout the magma chamber. Consequently, gravity settling of dense magnetite to the floor of the chamber occurs, thus creating a monominerallic magnetite layer (with trapped inclusions of plagioclase and pyroxene). An increase in plagioclase content at the gradational top of the magnetite layer is as a result of the system then crystallising cotectic proportions of magnetite-plagioclase followed by magnetite-plagioclase-pyroxene and ultimately returning to the original gabbroic sequence of plagioclase-pyroxene once again. Fe-Ti oxide oxidation exsolution features throughout the magnetite layer provide further diagnostic evidence for increases in fO_2 in the magma chamber. Most common is internal granular ilmenite exsolutions followed by external granular ilmenite exsolution. This fits well with the assumption that higher fO_2 prevailed during formation of magnetite layers. In contrast, disseminated magnetite gabbroic rocks do not show internal or external granular ilmenite exsolution but rather lower oxidation degree microtextures. These are most commonly abundant cloth-textured ulvöspinel and trellis intergrowths of ilmenite.

Extracting magnetite from the extensively weathered disseminated magnetite gabbro is most plausible as the highest V_2O_3 grades (1.26 wt. %) occur closest to the surface. The fresh disseminated magnetite gabbro (located ± 30-147 m below the MML) has an average V_2O_3 grade of 1.13 wt. %, making ore extraction less economically viable in this zone. Furthermore, the magnetite layer in this study has an average V_2O_3 grade of only 1.05 wt. %, rendering it less attractive economically. It is also located at a considerably deeper level than the higher grade weathered product, making the latter a better option in terms of convenient, economically viable mineral extraction.

References

Acquafredda, P., Caggianelli, A., and Piccarreta, G. (1992). Late magmatic to subsolidus coronas in gabbroic rocks from the Sila Massif (Calabria Italy). *Mineralogy and Petrology*. 46, p.229-238.

Anders, E., and Grevesse N. (1989). Abundances of the elements: Meteoritic and solar. *Geochimica et Cosmochimica Acta*. 53, p.197-214.

Ashwal, L.D., Webb, S.J., and Knoper, M.W. (2005). Magmatic stratigraphy in the Bushveld northern lobe: continuous geophysical and mineralogical data from the 2950 m Bellevue drillcore. *South African Journal of Geology.* 108, p.199-232.

Bateman, A.M. (1951). The formation of late magmatic oxide ores. *Economic Geology.* 46, p.404-426.

Buchanon, P.C., Reimold, W.U., Koeberl, C., and FJ, K. (2002). Geochemistry of intermediate to siliceous volcanic rocks of the Rooiberg Group, Bushveld Magmatic Province, South Africa. *Contributions to Mineralogy and Petrography. 144*, p.131-143.

Buick, I.S., Maas, R., and Gibson, R. (2001). Precise U-Pb titanite age constraints on the emplacement of the Bushveld Complex, South Africa. *Journal of the Geological Society. 158*, p.3-6.

Cameron, E.N. (1982). Upper Critical Zone, Eastern Bushveld Complex. *Economic Geology. 77*(6), p.1307-1327.

Cameron, E.N. (1978). The Lower Zone of the Eastern Bushveld Complex in the Olifants River Trough. *Journal of Petrology.* 19, p.437-462.

Cawthorn, R.G., and Ashwal, L.D. (2009). Origin of Anorthosite and Magnetitite Layers in the Bushveld Complex, Contstrained by Major Element Compositions in Plagioclase. *Journal of Petrology.* 50, p.1607-1637.

Cawthorn, R.G., and Molyneux, T. (1986). The vanadiferous magnetite deposits of the Bushveld Complex. In: Anhaeusser, C.R & Maske, S. (eds). *Mineral deposits of Southern Africa.* 2. Johannesburg: Geological Society of South Africa. p.1251-1266.

Cawthorn, R.G., Davies, G., Clubley-Armstrong, A., and McCarthy, T.S. (1981). Sills associated with the Bushveld Complex, South Africa: an estimate of the parental magma composition. *Lithos.* 14, p.1-15.

Cawthorn, R.G., and McCarthy, T.S. (1980). Variations in Cr content of magnetite from the Upper Zone of the Bushveld Complex – evidence for heterogeneity and convection currents in magma chambers. *Earth and Planetary Science Letters.* 46, p.335-343.

Cleason, D. T. (1998). Coronas, reaction rims, symplectites and emplacement depth of the Rymmen gabbro, Transscandinavian igneous belt, southern Sweden. *Mineralogical Magazine*. 62, p.743-757.

Eales, H.V., and Cawthorn, R.G. (1996). The Bushveld Complex. In R.G. Cawthorn (Ed.). *Layered Intrusions.* P.181-229. Amsterdam: Elsevier.

Ganino, C., Arndt, N. T., Zhou, M.F., Gaillard, F., and Chauvel, C. (2008). Interaction of magma with sedimentary wall rock and magnetite ore genesis in the Panzhihua mafic intrusion, SW China. *Mineralium Deposita*. 43, p.677-694.

Griffin, W.L., and Heier, K.S. (1973). Petrological implications of some corona structures. *Lithos.* 6, p.315-35.

Grobler, N.J., and Whitfield, G.G. (1970). The olivine-apatite magnetitites and related rocks in the Villa Nora occurrence of the Bushveld Igneous Complex. *Special Publication Geological Society South Africa.* 1, p.208-227.

Habashi, F. (2002). Two hundred years of vanadium. In: Tanner, M.F., Riveros, P.A., Dutrizac, J.E., Gattrell, M., Perron, L. (eds.). Vanadium, Geology, Processing and Applications, Proceedings of the International Symposium on Vanadium, Conference of Metallurgists. Montreal, Canada. August 11–14. p.3–15.

Habteselassie, M.M., Mathison, C.I., and Gilkes, R.J. (1996). Vanadium in magnetite gabbros and its behaviour during lateritic weathering, Windimurra Complex, Western Australia. *Australian Journal of Earth Sciences.* 43, p.555-566.

Harmer, R.E., and Armstrong, R.A. (2000). New precise dates on the acid phase of the Bushveld and their implications. Abstract. Workshop on the Bushveld Complex, 18th-21st November 2000, Burgersfort. University of Witwatersrand, Johannesburg.

Harney, D.M.W., von Gruenewaldt, G., and Merkle, R.K.W. (1996). The use of plagioclase composition as an indicator of magmatic processes in the Upper Zone of the Bushveld Complex. *Mineralogy and Petrology.* 56, p.91-103.

Harney, D.M.W., von Gruenewaldt, G. (1995). Ore-forming processes in the upper part of the Bushveld Complex, South Africa. *Journal of African Earth Sciences.* 20, p.77-89.

Harney, D.M.W., Merkle, R.K.W., and von Gruenewaldt, G. (1990). Platinum-group element behaviour in the lower part of the Upper Zone, Eastern Bushveld Complex – implications for the formation of the main magnetite layer. *Economic Geology.* 85, p.1777-1789.

Hatton, C. J. (1984). The effect of pressure, temperature and composition on the distribution of Fe and Mg between olivine, orthopyroxene and liquid: An appraisal of the

reversal in the normal fractionation trend in the Bushveld Complex. *Contributions to Mineralogy and Petrology*. 86, p.45-53.

Hill, M., Barker, F., Hunter, D., and Knight, R. (1996). Geochemical characteristics and origin of the Lebowa Granite Suite, Bushveld Complex. *International Geology Review. 38*, p.195-227.

Holness, M. B., Stripp, G., Humphreys, M. C. S., Veksler, I. V., Nielson, T. F. D., and Tegner, C. (2011). Silicate liquid immiscibility within the crystal mush: Late-stage magmatic microstructures in the Skaergaard Intrusion, East Greenland. *Journal of Petrology*. 52, p.175-222.

Howarth, G.H., and Prevec, S.A. (2013). Hydration vs. Oxidation: Modelling implications for Fe-Ti oxide crystallisation in mafic intrusions, with specific reference to the Panzihua intrusion, SW China. *Geoscience Frontiers.* 4, p.555-569.

Irvine, T.N., and Sharpe, M.R. (1986). Magma mixing and the origin of stratiform oxide oxide ore zones in the Bushveld and Stillwater Complexes. In: *Metallogeny of Basic and Ultrabasic Rocks* (Edited by Gallagher, M.J., Ixer, R.A., Neary, C.R., Prichard, H.M.). p.183-198. Institute Mining and Metallurgy, London.

Irving, A.J. (1978). A review of experimental studies of crystal/liquid trace element partitioning. *Geochemica et Cosmochimica Acta.* 42, p.743-770.

Jakobsen, J. K. Veksler, I. V., Tegner, C., and Brooks, C. K. (2011). Crystallisation of Skaergaard intrusion from an emulsion of immiscible iron- and silica-rich liquids: evidence from melt inclusions in plagioclase. *Journal of Petrology*. 52, p.345-373.

Jakobsen, J.K., Veksler, I.V., Tegner, C., and Brooks, C.K. (2005). Immiscible iron- and silica-rich melts in basalt petrogenesis documented in the Skaergaard intrusion. *Geology.* 33, p.885-888.

Klemm, D.D., von Gruenewaldt, G., Henckel, J., and Dehm, R. (1985). The geochemistry of titanomagnetite in magnetite layers and their host rocks of the eastern Bushveld Complex. *Economic Geology*. 80, p.1075-1088.

Koepke, J., Feig, S. T., Snow, J., and Freise, M. (2004). Petrogenesis of oceanic plagiogranites by partial melting of gabbros: an experimental study. *Contributions of Mineralogy and Petrology*. p.146, 414-
432.

Kogiso, T., Tatsumi, Y., and Nakano, S. (1997). Trace element transport during dehydration processes in the subducted oceanic crust: 1. Experiments and implications for the origin of ocean island basalts. *Earth and Planetary Science Letters.* 148, p.193-205.

Kruger, F.J., and Smart, R. (1987). Diffusion of trace elements during bottom crystallisation of double-diffusive convective systems: the magnetitite layers of the Bushveld Complex. *Journal of Volcanoloogy and Geothermal Research.* 34, p.133-142.

Larikova, T. L and Zaraisky, G. P. (2009). Experimental modelling of corona textures. *Journal of Metamorphic Geology.* 27, p.139-151.

Li, J., Xu, J.F., Suzuki, K., He, B., Xu, Y.G. and and Ren, Z.Y. (2010). Os, Nd and Sr isotope and trace element geochemistry of the Muli picrites: Insights into the mantle source of the Emeishan Large Igneous Province. *Lithos*. 119, p.108-122.

Lindstrom, D.J. (1976). Experimental study of the partitioning of the transition metals between clinopyroxene and co-existing silicate liquids: Unpub. Ph.D. dissert., University of Oregon. 188p.

Lipin, B.R. (1993). Pressure increase, the formation of chromatite layers and the development of the Ultramafic series in the Stillwater Complex. *Journal of Petrology.* 34, p.9976-9995.

Mathez, E.A., Van Tongeren, J.A., and Schweitzer, J. (2013). On the relationships between the Bushveld Complex and its felsic roof rocks, part 1: petrogenesis of Rooiberg and related felsites. *Contributions to Mineralogy and Petrology. 166*, p.435-449.

McCarthy, T.S., Cawthorn, R.G., Wright, C.J., and McIver, J.R. (1985). Mineral Layering in the Bushveld Complex: Implications of Cr Abundances in Magnetite from Closely Spaced Magnetitite and Intervening Silicate-Rich Layers. *Economic Geology.* 80, p.1062-1074.

Merkle, R.K., and von Gruenewaldt, G. (1986). Compositional variation of Co-rich pentlandite: relation to evolution of the Upper Zone of the western Bushveld Complex, South Africa. *Canadian Mineralogist.* 24, p.529-546.

Molyneux, T.G. (1970). The geology of the area in the vicinity of Magnet Heights, Eastern Transvaal, with special reference to the magnetic iron ore. *Geological Society of South Africa*. Special Publication. 1, p.228-241.

Mongkoltip, P., and Ashworth, J.R. (1983). Quantitative Estimation of an Open-system Symplectite-forming Reaction: Restricted Diffusion of Al and Si in Coronas around Olivine. *Journal of Petrology.* 24, p.635-661.

Morimoto, N., Fabries, J., Ferguson, A. K., Ginzburg, I. V., Ross, M., Seifert, F. A., Zussman, J., Aoki, K. and Gottardi, G. (1988). Nomenclature of pyroxenes. *American Mineralogist*. 73, p.1123-1133.

Morse, S.A. (1979). Kiglapait geochemistry II: Petrography. *Journal of Petrology*. 20, p.591-624.

Moskalyk, R.R., and Alfantazi, A.M. (2003). Processing of vanadium: a review. *Minerals Engineering.* 16. P.793-805.

Namur, O., Charlier, B., Toplis, M.J., Higgins, M.D., Liégeois, J.P., and Vander Auwera, J. (2010). Crystallization sequence and magma chamber processes in the ferrobasaltic Sept Iles layered intrusion, Canada. *Journal of Petrology*. 51, p.1203–1236.

Nesbitt, H.W., and Young, G.M. (1984). Prediction of some weathering trends of plutonic and volcanic rocks based on thermodynamic and kinetic considerations. *Geochimica Cosmochimica Acta*. 48, p.1523-1534.

Osborn, E.F. (1980). On the cause of reversal of the normal fractionation trend – an addendum to the paper by E.N. Cameron 'Evolution of the Lower Critical Zone, central sector, eastern Bushveld Complex, and its chromite deposits'. *Economic Geology.* 75, p.872-875.

Pang, K.N., Li, C., Zhou, M.F., and Ripley, E.M., (2009). Mineral compositional constraints on petrogenesis and oxide ore genesis of the late Permian Panzhihua layered gabbroic intrusion, SW China. *Lithos*. 110, p.199–214.

Parsons, I. (1980). Alkali-feldspar and Fe-Ti oxide exsolution textures as indicators of the distribution and subsolidus effects of magmatic "water" in the Klokken layered syenite

intrusion, south Greenland. Royal Society of Edinburgh Transcript. *Earth Sciences*. 71, p.1-12.

Philpotts, A.R., and Doyle, C.D. (1983). Effect of magma oxidation state on the extent of silicate liquid immiscibility in a tholeiitic basalt. *American Journal of Science.* 283, p.967-986.

Philpotts, A. R. (1967). The origin of certain iron-titanium oxide and apatite rocks. *Economic Geology*. 62, p.303-315.

Ragan, D.M. (1969). Olivine recrystallization textures. *Mineralogical Magazine.* 37(286), p.238.

Reese, R.G. Jr. (2001). Vanadium, domestic survey tables by A.A. Wario and world data by R.G. Coleman. p.81.1-81.2.

Reynolds, I.M. (1985a). The Nature and Origin of Titaniferous Magnetite-Rich Layers in the Upper Zone of the Bushveld Complex: A Review and Synthesis. *Economic Geology*. 80, p.1089-1105.

Reynolds, I.M. (1985b). Contrasted Mineralogy and Textural Relationships in the Uppermost Titaniferous Magnetite Layers of the Bushveld Complex in the Bierkraal Area North of Rustenburg. *Economic Geology*. 80, p.1027-1048.

Saager, R. (1984). *Metallische Rohstoffe von Antimon bis Zirconium.* 176p. Bank Vontobel, Zurich.

SACS (South African Committee for Stratigraphy). 1980. Stratigraphy of South Africa. Part 1. Lithostratigraphy of the Republic of South Africa, South West Africa/Namibia, and the Republics of Bophuthatswana, Transkei and Venda. In: Kent, L.E. (Ed.). *Geological Survey of South Africa*. Handbook 8, 690 pp.

Scoates, J.S., Wall, C.J., Friedman, R.M., Van Tongeren, J.A., and Mathez, E.A. (2012). The age of the Bushveld Complex. Goldschmidt 2012 Conference Abstracts.

Sharpe, M.R. (1981). The chronology of magma influxes in the Eastern Bushveld Complex as exemplified by its marginal border groups. *Journal of Geological Society of London.* 138, p.307-326.

Starmer, I.C. (1969). Basic plutonic intrusions of the RisÖr-S/SÖndeled area, South Norway. The original lithologies and their metamorphism. *Norsk Geol. Tidsskr*. 49, p.403-431.

Tegner, C., Cawthorn, R.G., and Kruger, F.J. (2006). Cyclicity in the Main and Upper Zones of the Bushveld Complex, South Africa: crystallization from a zoned magma sheet. *Journal of petrology.* 47, 2257-2279.

Teigler, B., Eales, H.V., and Scoon, R.N. (1992). The cumulate succession in the Critical Zone of the Rustenburg Layered Suite at Brits, western Bushveld Complex. *South African Journal of Geology. 95*, p.17-28.

Toplis, M.J., and Corgne, A. (2002). An experimental study of element partitioning between magnetite, clinopyroxene and iron-bearing silicate liquids with particular emphasis on vanadium. *Contributions to Mineralogical Petrology.* 144, p.22-37.

Toplis, M.J., and Carroll, M.R. (1995). An experimental study of the influence of oxygen fugacity on Fe-Ti oxide stability, phase relations, and mineral-melt equilibria in ferro-basaltic systems. *Journal of Petrology*. 36, p.1137-1170.

Turner, S.P., and Stüwe, K. (1992). Low-pressure corona textures between olivine and plagioclase in un-metamorphosed gabbros from Black Hill, South Australia. *Mineralogical Magazine*. 56, p.503-509.

Twist, D., and French, B.M. (1983). Voluminous acid volcanism in the Bushveld Complex: a review of the Rooiberg Felsite. *Bulletin of Volcanism. 46*, p.225-242.

Ulmer, G.C. (1969). Experimental investigation of chromite spinels. *Economic Geology Monograph.* 4, p.114-131.

United States Geological Survey. (2015). Mineral commodity summaries 2015. US Department of Interior. p.176-177

Van Tongeren, J.A., Mathez, E.A., and Kelemen, P.B. (2010). A felsic end to Bushveld differentiation. *Journal of Petrology*. 51, p.1891-1912.

Veksler, I.V., Dorfman, A.M., Borisov, A.A., Wirth, R., and Dingwell, D.B. (2007). Liquid immiscibility and the evolution of basaltic magma. *Journal of Petrology.* 48, p.2187-2210.

Vermaak, C.F. (1976). The Merensky Reef-thoughts on its environment and genesis. *Economic Geology. 71*, p.1270-1298.

Viljoen M.J., and Schurmann, L.W. (1998). Platinum group metals. In: Wilson, M.G.C., Anhaeusser, C.R. (eds). The Mineral Resources of South Africa, Council for Geoscience, Pretoria. p.532-568.

von Gruenewaldt, G., Klemm, D.D., Henckel, J., and Dehm, R. (1985). Exsolution features in titanomagnetites from massive magnetite layers and their host rocks of the Upper Zone, eastern Bushveld Complex. *Economic Geology.* 80, p.1049-1061.

von Gruenewaldt, G. (1973). The Main and Upper Zone of the Bushveld Complex in the Roossenekal area, Eastern Transvaal. *Geological Society of South Africa*. 76, p.207-227.

Van Lamoen, H. (1979). Coronas in olivine gabbros and iron ores from Susimaki and Riuttamaa, Finland. *Contributions to Mineralogy and Petrology*. 68, p.259-268.

Wager, L.R., Brown, G.M. (1968). *Layered Igenous Rocks.* London: Oliver and Boyd. 572 pp.

Walraven, F.J. (1997). Geochronology of the Rooiberg Group, Transvaal Supergroup, South Africa. *Economic Geology Research Unit, University of Witwatersrand Information Circular, 316*.

Walraven, F., Armstrong, R.A., and Kruger, F.J. (1990). A chronostratigraphic framework for the north-central Kaapvaal craton, the Bushveld Complex and Vredefort structure. *Tectonophysics.* 171, p.23-48.

Watson, E.B. (1976). Two-liquid partition coefficients: experimental data and geochemical implications. *Contributions to Mineralogy and Petrology.* 56, p.119-134.

Whitney, P.R., and McLelland, J.M. (1973). Origin of coronas in metagabbros of the Adirondack Mts., N.Y. *Contributions to Mineralogy and Petrology.* 39, p.81-98.

Willemse, J. (1969). The geology of the Bushveld Igneous Complex, the largest repository of magmatic ore deposits in the world. *Economic Geology*. 4, p.1-22.

Xiao, L., Xu, Y.G., Mei, H.J., Zheng, Y.F., He, D., and Pirajno, F. (2004). Distinct mantle sources of low-Ti and high-Ti basalts from the western Emeishan large igneous province, SW China: implications for plume-lithosphere interaction. *Earth and Planetary Letters.* 228, p. 525-546.

Zhou, M.F., Robinson, P.T., Lesher, C. M., Keays, R. R., Zhang, C.J., and Malpas, J. (2005). Geochemistry, Petrogenesis and Metallogenesis of the Panzhihua gabbroic layered intrusion and associated Fe-Ti-V oxide deposits, Sichuan Province, SW China. *Journal of Petrology*. 46, p.2253-2280.

Appendix A: EPMA detection limits and standards

Oxide detection limits

Curr.(A) : 2.003E-008

Element	Peak(mm)	Net(cps)	Bg-	Bg+	S.D.(%)	D.L.(ppm)	K-raw(%)
1 Al	90.910	546.4	25.6	13.0	0.81	64	18.404
2 Si	77.791	7.9	54.0	29.8	22.13	92	0.111
3 Mg	107.758	143.4	11.4	7.4	1.62	77	2.782
4 Fe	134.685	706.1	3.4	2.0	0.69	471	336.376
5 Mn	146.215	1.0	4.2	4.6	57.49 ?	654	0.284
6 V	174.465	6.3	2.0	1.4	8.94	651	0.847
7 Cr	145.283	2.4	1.8	1.8	18.64	2592	1.796
8 Ti	88.268	4732.2	162.6	81.8	0.27	108	17.909

ZAF Oxide

Element	Mass(%)	Cation	K(%)	K-raw(%)	ZAF	Z	A	F
Al2O3	4.064	0.1908	3.107	18.404	1.3082	0.9275	1.3899	1.0148
SiO2	0.043	0.0017	0.043	0.111	0.9993	0.9402	1.0629	0.9999
MgO	2.019	0.1199	1.403	2.782	1.4392	0.9235	1.5544	1.0026
FeO	73.219	2.4392	78.275	336.376	0.9354	0.9306	1.0052	1.0000
MnO	0.116	0.0039	0.120	0.284	0.9631	0.9573	1.0061	1.0000
V2O3	1.248	0.0398	1.244	0.847	1.0029	1.0845	1.0054	0.9198
Cr2O3	1.594	0.0502	1.796	1.796	0.8874	0.9959	1.0147	0.8781
TiO2	16.894	0.5061	17.906	17.909	0.9435	0.9795	1.0139	0.9500
Total	99.197	3.3517	103.894	378.508	Total O =	4.0	Iteration = 4	

Silicate detection limits

Curr.(A) : 2.008E-008

Element	Peak(mm)	Net(cps)	Bg-	Bg+	S.D.(%)	D.L.(ppm)	K-raw(%)
1 Ca	107.712	951.1	11.0	6.0	0.60	90	44.248
2 Cr	73.566	1.1	23.4	26.0	117.94 ?	179	0.034
3 Si	77.786	10801.5	35.6	23.2	0.18	67	95.541
4 Al	90.923	5131.1	25.2	14.6	0.26	65	99.569
5 Fe	134.711	2.6	2.4	1.8	18.31	392	0.304
6 K	120.159	5.2	3.2	3.2	11.96	132	1.495
7 Mn	146.478	-0.4	1.2	2.0	100.00 ?	626	0.000

8 Na	129.815	814.5	21.0	21.6	0.66	68	33.752
9 Mg	107.929	9.4	57.4	25.2	18.01	47	0.028
10 Ti	88.202	20.9	78.6	47.8	10.60	75	0.076

ZAF Oxide

Element	Mass(%)	Cation	K(%)	K-raw(%)	ZAF	Z	A	F
CaO	11.388	0.8253	11.283	44.248	1.0093	1.0010	1.0080	1.0003
Cr2O3	0.017	0.0009	0.015	0.034	1.0859	1.0535	1.0141	1.0164 ?
SiO2	54.949	3.7164	52.156	95.541	1.0536	1.0005	1.0524	1.0005
Al2O3	28.411	2.2649	28.407	99.569	1.0001	1.0004	0.9999	0.9999
FeO	0.301	0.0170	0.273	0.304	1.1032	1.0944	1.0081	1.0000
K2O	0.149	0.0129	0.148	1.495	1.0051	1.0065	1.0083	0.9904
MnO	0.000	0.0000	0.000	0.000	0.0000	0.0000	0.0000	0.0000 ?
Na2O	4.696	0.6159	4.669	33.752	1.0058	0.9981	1.0089	0.9989
MgO	0.032	0.0032	0.028	0.028	1.1543	0.9948	1.1720	0.9901
TiO2	0.085	0.0043	0.076	0.076	1.1097	1.0671	1.0401	0.9998
Total	100.028	7.4607	97.055	275.046	Total O = 12.0		Iteration = 4	

Silicate standards

Element	Standard name	Mass(%)	ZAF Fac.	Z	A	F
1 CaO	Cr_Diopside_SPI	25.5000	0.8650	0.9360	0.9237	1.0005
2 Cr2O3	Chromite_SPI	45.6500	0.3567	0.3587	0.9779	1.0169
3 SiO2	Cr_Diopside_SPI	54.5900	3.2169	4.4069	0.7293	1.0009
4 Al2O3	Plag-An65_SPI	28.5300	4.1586	5.8530	0.7029	1.0109
5 FeO	Hematite_SPI	89.6933	0.2142	0.2169	0.9873	1.0000
6 K2O	Biotite_SPI	9.9100	1.0827	1.2070	0.8953	1.0019
7 MnO	Rhodonite_SPI	42.3000	0.2678	0.2737	0.9787	1.0000
8 Na2O	SRM_610	13.8330	5.1782	10.7395	0.4808	1.0027
9 MgO	Periclase_SPI	100.0039	5.3788	7.8316	0.6868	1.0000
10 TiO2	Rutile_SPI	99.9834	0.5913	0.6060	0.9757	1.0000

Oxide standards

Element	Standard name	Mass(%)	ZAF Fac.	Z	A	F
1 Al2O3	Orthoclase_SPI	16.8800	4.2385	5.8730	0.7112	1.0148
2 SiO2	Almandine_SPI	39.1900	2.9163	4.4824	0.6505	1.0001
3 MgO	Olivine_SPI	50.4300	4.8434	7.8682	0.6137	1.0031
4 FeO	Almandine_SPI	23.2700	0.1990	0.2024	0.9832	1.0000
5 MnO	Rhodonite_SPI	42.3000	0.2678	0.2737	0.9787	1.0000
6 V2O3	V_SPI	146.8200	0.5096	0.5216	0.9769	1.0000
7 Cr2O3	Chromium_Oxide_SPI	100.0131	0.3656	0.3706	0.9865	1.0000
8 TiO2	Rutile_SPI	99.9834	0.5913	0.6060	0.9757	1.0000

Appendix B: Whole-rock major and trace element geochemical data

Depth (m)	148	147.8	147.6	147.4	147.2	147	145.1	143.3	142.5	139.9
Sample	BS 1	BS 2	BS 3	BS 4	BS 5	OFSZ 1	OFSZ 5	P 2	P 1	OBSZ 3
SiO_2	1.46	1.67	5.81	2.38	21.88	41.79	40.41	51.86	48.79	44.58
TiO_2	>8.00	>8.00	>8.00	>8.00	>8.00	3.07	3.37	0.40	0.62	2.21
Al_2O_3	3.72	3.84	5.68	4.10	13.16	22.22	14.76	15.11	13.69	13.19
Fe_2O_3	80.04	79.73	73.35	78.66	48.57	19.00	23.48	7.56	13.50	20.54
MnO	0.27	0.27	0.24	0.26	0.17	0.08	0.19	0.17	0.26	0.22
MgO	2.21	2.11	2.00	2.02	1.32	0.54	4.10	6.86	7.37	6.26
Na_2O	0.10	0.15	0.45	0.17	1.81	3.52	2.32	2.58	2.45	2.02
K_2O	0.01	0.06	0.03	0.02	0.14	0.33	0.26	0.24	0.30	0.17
P_2O_5	<0.002	<0.002	<0.002	<0.002	<0.002	0.00	0.00	0.01	<0.002	<0.002
LOI	-2.62	-2.64	-2.23	-2.16	-1.11	0.03	0.95	0.62	2.21	0.52
Total	100.13	99.88	99.65	99.86	98.99	99.43	99.50	99.79	99.73	99.88
Li	0.70	0.80	1.30	1.10	2.70	5.60	10.50	4.30	12.40	5.00
Sc	32.10	31.30	29.30	31.40	19.60	8.10	41.90	36.20	34.30	50.50
V	17285.00	17744.00	15212.60	17081.30	8718.70	2658.40	2755.00	167.00	201.30	1917.50
Cr	7666.90	5086.50	2682.40	1442.70	487.60	129.90	14.70	311.10	299.90	40.10
Co	346.90	339.50	307.90	338.50	188.20	69.10	102.20	36.10	64.10	99.80
Ni	596.00	582.80	507.00	562.60	309.40	103.70	142.90	92.50	107.00	126.60
Cu	45.30	45.30	35.20	41.60	29.10	25.70	22.10	10.60	121.00	17.40
Zn	446.50	434.30	388.10	436.00	250.30	89.80	113.40	45.30	90.60	110.70
Rb	2.30	2.40	2.40	2.40	1.80	2.60	7.40	1.60	9.70	3.40
Sr	5.20	10.90	58.30	19.60	219.90	392.70	248.10	304.70	246.10	225.10
Y	2.40	2.40	2.30	2.40	1.80	1.20	5.40	17.20	9.60	b.d
Zr	26.20	28.10	25.20	28.20	16.70	5.90	11.90	13.20	4.00	6.40
Nb	5.80	6.70	6.10	6.00	3.80	1.50	1.20	0.90	1.00	b.d
Ba	2.40	4.20	13.00	7.70	58.60	110.50	76.90	71.30	111.90	62.90
La	0.13	0.14	0.35	0.19	0.70	1.66	1.41	1.60	5.61	1.07
Ce	0.28	0.28	0.68	0.34	0.98	2.77	3.00	3.42	14.63	2.30
Pr	0.04	0.03	0.07	0.04	0.11	0.28	0.41	0.55	2.26	0.35
Nd	0.20	0.13	0.32	0.13	0.36	0.98	2.05	3.04	11.35	2.02
Sm	0.06	0.04	0.06	b.d	0.06	0.15	0.63	0.95	2.88	0.65
Eu	0.02	0.02	0.08	0.03	0.29	0.54	0.52	0.65	1.19	0.47
Tb	0.01	0.00	0.01	0.00	0.01	0.01	0.13	0.23	0.47	0.15
Gd	0.07	0.03	0.05	0.04	0.04	0.10	0.81	1.29	3.01	0.83
Dy	0.07	0.03	0.06	0.03	0.04	0.08	0.90	1.54	2.96	1.00
Ho	0.02	0.01	0.01	0.01	0.01	0.01	0.18	0.33	0.58	0.21
Er	0.04	0.02	0.04	0.02	0.03	0.04	0.57	1.00	1.73	0.64
Tm	0.01	0.00	0.01	0.00	0.00	0.01	0.08	0.14	0.24	0.09
Yb	0.05	0.03	0.04	0.03	0.03	0.04	0.50	0.96	1.50	0.64
Lu	0.01	0.01	0.01	0.01	0.01	0.01	0.08	0.14	0.22	0.10
Hf	0.91	0.89	0.92	1.00	0.62	0.31	0.44	0.36	0.72	0.34
Ta	0.28	0.30	0.29	0.31	0.18	0.07	0.07	0.01	b.d.	0.04
Pb	6.40	6.40	6.00	6.40	4.80	3.20	3.50	2.60	2.90	b.d
Th	5.30	5.60	5.60	5.60	4.20	2.90	3.10	2.30	2.50	b.d
U	4.30	4.00	4.20	3.20	2.20	3.40	2.60	2.10	2.00	b.d

Whole-rock major and trace element geochemical data continued

Depth (m)	139.9	134.5	128.5	118.2	111	102.1	75.1	34.3	20.8	11.8	6
Sample	OBSZ 3	OBSZ 6	OHSZ 3	OHSZ 5	OHSZ 7	WG 1	WG 3	WG 6	LS 5	LS 3	LS 1
SiO_2	44.58	44.58	27.84	36.04	40.63	43.37	46.16	42.73	14.63	20.74	16.00
TiO_2	2.21	2.76	7.00	4.79	3.63	2.91	1.96	2.78	>8.00	>8.00	7.76
Al_2O_3	13.19	18.45	13.77	14.28	15.05	13.24	13.17	14.44	10.30	16.83	13.97
Fe_2O_3	20.54	16.17	40.53	30.15	24.81	23.12	19.42	21.44	56.96	42.91	50.61
MnO	0.22	0.14	0.17	0.19	0.19	0.23	0.23	0.17	0.19	0.14	0.14
MgO	6.26	2.35	2.13	3.53	4.25	5.84	6.41	5.49	0.85	0.35	0.33
Na_2O	2.02	2.86	2.03	2.20	2.39	2.12	2.12	2.29	0.82	0.04	0.04
K_2O	0.17	0.30	0.19	0.22	0.19	0.19	0.14	0.21	0.04	0.02	0.01
P_2O_5	<0.002	0.11	<0.002	<0.002	<0.002	<0.002	<0.002	0.01	<0.002	<0.002	0.01
LOI	0.52	1.12	-0.93	-0.22	-0.43	-0.79	-0.54	-0.07	2.36	8.17	8.83
Total	99.88	99.83	98.77	99.13	99.50	100.08	99.82	99.59	98.94	98.32	97.76
Li	5.00	5.30	2.90	3.20	3.60	2.30	3.20	2.70	2.90	3.60	5.10
Sc	50.50	34.70	25.70	35.70	38.10	53.60	58.50	51.60	25.70	20.70	17.80
V	1917.50	708.70	5969.40	3608.90	2521.70	1861.00	1246.50	1531.40	10075.40	5430.30	5258.70
Cr	40.10	54.70	6.30	0.00	5.10	7.00	12.40	28.00	7.60	6.00	6.40
Co	99.80	57.10	177.50	132.80	114.10	112.20	99.20	114.90	140.20	71.90	113.50
Ni	126.60	88.70	264.70	171.60	124.40	107.00	85.40	91.70	320.30	140.50	182.80
Cu	17.40	104.00	834.60	604.50	493.20	387.40	343.60	318.80	1084.20	575.90	1368.20
Zn	110.70	87.50	207.20	153.30	125.80	110.60	97.20	93.40	310.00	139.60	200.40
Rb	3.40	5.70	4.80	2.40	3.10	1.30	2.00	3.70	2.00	1.60	1.70
Sr	225.10	346.50	244.20	256.90	270.00	235.00	230.60	248.50	118.10	9.00	6.30
Y	b.d	7.90	1.70	4.00	4.00	5.30	5.50	4.20	2.00	1.60	1.70
Zr	6.40	19.60	11.40	8.30	7.00	5.90	4.20	8.80	16.00	3.60	8.30
Nb	b.d	1.30	4.00	2.30	1.20	1.20	1.10	1.20	3.90	1.40	2.60
Ba	62.90	117.00	61.30	67.60	71.00	57.90	51.40	61.40	77.30	22.80	35.70
La	1.07	6.00	0.80	0.97	1.03	0.92	0.88	1.69	0.26	0.37	0.81
Ce	2.30	12.32	1.24	1.76	1.99	2.00	1.91	3.37	0.38	1.61	1.08
Pr	0.35	1.57	0.15	0.23	0.27	0.31	0.29	0.43	0.04	0.07	0.17
Nd	2.02	6.70	0.60	1.14	1.38	1.63	1.61	2.03	0.17	0.26	0.61
Sm	0.65	1.46	0.15	0.34	0.44	0.59	0.55	0.51	0.04	0.05	0.10
Eu	0.47	1.08	0.35	0.40	0.45	0.46	0.44	0.34	0.10	0.15	0.20
Tb	0.15	0.22	0.03	0.07	0.09	0.13	0.13	0.10	0.01	0.01	0.02
Gd	0.83	1.46	0.17	0.43	0.52	0.72	0.80	0.62	0.04	0.04	0.11
Dy	1.00	1.31	0.21	0.49	0.64	0.88	0.98	0.68	0.04	0.04	0.09
Ho	0.21	0.26	0.05	0.10	0.13	0.19	0.21	0.14	0.01	0.01	0.02
Er	0.64	0.73	0.14	0.32	0.43	0.55	0.62	0.41	0.03	0.02	0.06
Tm	0.09	0.10	0.02	0.05	0.06	0.08	0.09	0.06	0.00	0.00	0.01
Yb	0.64	0.62	0.13	0.31	0.39	0.57	0.61	0.41	0.03	0.03	0.05
Lu	0.10	0.09	0.02	0.05	0.06	0.09	0.10	0.06	0.00	0.00	0.01
Hf	0.34	0.75	0.48	0.36	0.31	0.31	0.24	0.33	0.60	0.18	0.35
Ta	0.04	0.12	0.15	0.08	0.06	0.04	0.02	0.04	0.24	0.06	0.14
Pb	b.d	3.00	4.40	3.80	3.50	3.40	3.30	3.40	5.20	4.20	4.50
Th	b.d	2.70	3.90	3.40	3.10	3.00	2.90	3.00	4.60	3.70	4.00
U	b.d	2.10	3.00	2.60	2.40	2.30	2.20	2.30	3.50	2.80	3.10

Whole-rock major and trace element geochemical data continued

Depth(m)	150	149.5	149	148.5	148.1	146.2	146	145.5	143.8	142.1	141.1
Sample	AN 1	AN 2	AN 3	AN 4	AN 5	OFSZ 2	OFSZ 3	OFSZ 4	P 3	OBSZ 1	OBSZ 2
V	349.80	68.90	39.50	32.30	6980.80	10376.90	1499.60	2463.50	221.40	9338.70	2964.00
Cr	152.90	23.60	15.10	19.90	2856.90	34.00	31.20	13.70	306.90	347.50	86.10
Co	68.10	16.40	11.50	8.10	170.90	222.90	79.30	93.60	55.20	232.30	99.60
Ni	87.00	17.70	9.60	9.40	271.50	351.70	94.20	117.80	113.00	355.20	130.40
Cu	20.00	13.40	11.00	23.80	93.00	32.50	25.90	26.40	9.00	38.80	25.40
Zn	84.80	20.80	20.80	21.60	207.30	283.40	90.00	107.70	92.10	323.30	118.40
Rb	3.20	10.70	8.10	8.40	40.50	3.90	6.00	7.10	1.70	2.40	2.60
Sr	280.70	423.10	440.70	455.20	221.00	157.60	309.40	306.80	294.70	106.90	304.00
Y	5.70	2.40	2.20	1.30	1.70	1.90	3.90	3.20	14.10	1.70	2.90
Zr	7.10	7.40	5.30	4.70	13.40	17.00	9.00	10.90	9.80	17.90	7.10
Nb	1.00	0.80	0.80	0.80	3.30	3.70	1.30	2.00	1.00	4.60	1.80
Pb	2.90	2.30	2.30	2.20	4.40	5.10	3.10	3.40	2.80	5.10	3.50
Th	2.50	2.00	2.00	2.00	3.90	4.50	2.70	3.00	2.50	4.50	3.10
U	1.90	1.60	1.50	1.50	4.30	2.10	2.30	2.30	2.30	2.00	2.60

Depth(m)	138.9	136.7	131.8	130.8	123.8	112	89.2	63.1	48.1	14.1	8.5
Sample	OBSZ 4	OBSZ 5	OHSZ 1	OHSZ 2	OHSZ 4	OHSZ 6	WG 2	WG 4	WG 5	LS 4	LS 2
V	1178.90	844.80	3893.80	3198.00	4815.30	2650.10	1515.90	1184.90	1120.50	2884.50	5620.20
Cr	29.80	28.20	5.60	8.80	5.90	5.10	1.50	6.30	8.30	4.80	18.60
Co	87.10	85.20	139.20	119.90	154.20	119.00	91.70	104.90	97.20	87.90	89.30
Ni	106.20	101.40	223.00	198.90	205.40	130.20	88.30	81.70	81.10	190.20	152.20
Cu	13.60	18.00	657.20	698.00	691.40	451.80	516.90	346.60	442.80	954.60	485.60
Zn	87.70	83.60	151.90	132.60	180.60	138.50	102.70	94.90	89.30	181.80	187.70
Rb	3.60	1.20	2.60	1.40	2.90	2.90	4.20	1.20	2.10	1.90	1.60
Sr	228.20	214.50	221.10	252.50	265.70	278.40	274.40	213.70	242.30	25.80	6.30
Y	7.30	9.90	5.00	5.10	1.90	3.70	4.30	6.40	5.90	1.30	1.60
Zr	6.40	6.70	8.70	9.00	9.80	7.10	5.40	2.70	3.00	7.80	4.70
Nb	1.10	1.00	2.00	1.40	2.30	1.20	1.10	1.10	1.10	1.70	2.20
Pb	3.10	3.00	3.90	3.60	4.10	3.60	3.20	3.30	3.20	3.40	6.80
Th	2.70	2.70	3.50	3.20	3.60	3.10	2.80	2.90	2.80	3.00	3.80
U	2.40	3.00	2.00	2.00	2.70	2.40	2.20	2.20	2.10	2.30	2.90

Appendix C: Mineral compositional data

Plagioclase mineral compositional data

Depth(m)	148.1	148.1	148.1	147.8
Sample	AN5_plag2	AN5_plag3	AN5_plag8	BS2_plag1
SiO_2	54.50	55.02	53.62	55.08
Al_2O_3	28.48	27.61	28.49	28.18
FeO	0.41	0.26	1.95	0.31
CaO	11.32	10.80	10.42	11.25
Na_2O	5.03	5.37	4.94	5.08
K_2O	0.18	0.11	0.38	0.02
BaO	0.00	0.00	0.00	0.00
Total	**99.91**	**99.16**	**99.81**	**99.91**
Si	2.46	2.50	2.44	2.48
Al	1.51	1.47	1.53	1.50
Fe	0.01	0.01	0.07	0.01
Ca	0.54	0.52	0.50	0.54
Na	0.44	0.47	0.43	0.44
K	0.01	0.01	0.02	0.00
Ba	0.00	0.00	0.00	0.00
Total	**4.97**	**4.98**	**4.99**	**4.97**
An	54	52	53	55
Ab	44	47	45	45
Or	2	1	2	0

147.8	147.8	147.8	147.4	147.4	147.4
BS2_plag2	BS2_plag3	BS2_plag5	BS4_plag1	BS4_plag4	BS4_plag5
54.02	54.62	54.95	54.84	55.99	53.86
28.31	27.59	28.41	27.11	28.91	28.28
0.21	0.39	0.30	0.37	0.34	0.30
11.50	10.99	11.39	10.91	10.84	11.28
5.09	5.25	4.70	5.45	5.22	4.88
0.00	0.02	0.15	0.06	0.15	0.14
0.00	0.00	0.00	0.00	0.00	0.00
99.13	**98.87**	**99.89**	**98.74**	**101.45**	**98.74**
2.46	2.49	2.48	2.50	2.49	2.46
1.51	1.48	1.51	1.46	1.51	1.52
0.01	0.01	0.01	0.01	0.01	0.01
0.56	0.53	0.55	0.53	0.51	0.55
0.44	0.48	0.41	0.48	0.45	0.43
0.00	0.01	0.01	0.01	0.01	0.01
0.00	0.00	0.00	0.00	0.00	0.00
4.98	**5.00**	**4.97**	**4.99**	**4.98**	**4.98**
55	53	57	52	53	55
45	46	42	47	46	44
0	1	1	1	1	1

Plagioclase mineral compositional data continued

Depth(m)	147.2	147.2	147.2	147.2	147.2
Sample	BS5_plag1	BS5_plag2	BS5_plag3	BS5_plag4	BS5_plag6
SiO_2	54.23	54.04	54.16	54.07	54.64
Al_2O_3	27.74	29.00	29.41	29.41	27.69
FeO	0.37	0.38	0.27	0.26	0.45
CaO	12.97	13.36	13.10	12.90	11.70
Na_2O	4.75	4.55	4.67	4.36	5.01
K_2O	0.21	0.07	0.12	0.12	0.35
BaO	0.00	0.00	0.00	0.00	0.00
Total	**100.28**	**101.40**	**101.72**	**101.11**	**99.84**
Si	2.45	2.42	2.41	2.42	2.48
Al	1.48	1.53	1.54	1.56	1.48
Fe	0.01	0.01	0.01	0.01	0.01
Ca	0.63	0.64	0.63	0.61	0.57
Na	0.41	0.39	0.40	0.37	0.44
K	0.01	0.00	0.01	0.01	0.02
Ba	0.00	0.00	0.00	0.00	0.00
Total	**4.99**	**4.99**	**5.00**	**4.98**	**5.00**
An	59	61	60	61	55
Ab	39	38	39	38	43
Or	2	1	1	1	2

147.2	147.2	147.2	147.2	145
BS5_plag7	BS5_plag8	BS5_plag10	BS5_plag12	OFSZ4_plag1
54.55	54.32	53.44	55.25	56.50
28.22	28.32	27.53	27.22	27.42
0.34	0.37	0.17	0.23	0.99
12.20	12.20	12.43	11.42	10.49
4.79	4.89	4.93	4.89	4.65
0.24	0.11	0.19	0.33	0.28
0.00	0.00	0.00	0.00	0.00
100.34	**100.21**	**98.70**	**99.34**	**100.33**
2.46	2.46	2.45	2.51	2.54
1.50	1.51	1.49	1.46	1.45
0.01	0.01	0.01	0.01	0.03
0.59	0.59	0.61	0.56	0.50
0.42	0.42	0.43	0.43	0.40
0.01	0.01	0.01	0.01	0.01
0.00	0.00	0.00	0.00	0.00
4.99	**5.00**	**5.00**	**4.98**	**4.93**
58	58	58	55	55
41	42	41	43	44
1	1	1	2	1

Plagioclase mineral compositional data continued

Depth(m)	145	145	145	145	145
Sample	OFSZ4_plag2	OFSZ4_plag4	OFSZ4_plag5	OFSZ4_plag6	OFSZ4_plag8
SiO_2	54.50	54.62	53.42	54.47	54.51
Al_2O_3	27.41	27.17	28.26	27.23	28.17
FeO	0.37	0.29	0.34	0.32	0.58
CaO	11.57	11.64	13.17	11.77	11.06
Na_2O	5.23	5.24	4.59	5.17	5.02
K_2O	0.40	0.27	0.23	0.30	0.33
BaO	0.00	0.00	0.00	0.00	0.00
Total	**99.49**	**99.23**	**100.00**	**99.26**	**99.66**
Si	2.48	2.49	2.43	2.48	2.47
Al	1.47	1.46	1.51	1.46	1.50
Fe	0.01	0.01	0.01	0.01	0.02
Ca	0.56	0.57	0.64	0.58	0.53
Na	0.46	0.46	0.40	0.45	0.44
K	0.02	0.01	0.01	0.01	0.01
Ba	0.00	0.00	0.00	0.00	0.00
Total	**5.00**	**5.00**	**5.00**	**4.99**	**4.97**
An	53	54	61	55	54
Ab	44	44	38	44	44
Or	2	2	1	1	2

145	145	145	145	143
OFSZ4_plag9	OFSZ4_plag10	OFSZ4_plag11	OFSZ4_plag12	P1_plag3
54.56	55.75	55.09	55.57	54.30
27.05	28.07	28.62	27.75	27.36
0.39	0.42	0.09	0.39	0.23
11.82	11.98	11.96	11.45	12.13
5.14	5.18	5.11	5.06	4.66
0.22	0.34	0.30	0.31	0.31
0.00	0.00	0.00	0.00	0.00
99.18	**101.74**	**101.18**	**100.53**	**98.99**
2.49	2.48	2.46	2.50	2.48
1.45	1.47	1.50	1.47	1.47
0.01	0.01	0.03	0.01	0.01
0.57	0.57	0.57	0.55	0.59
0.45	0.44	0.44	0.44	0.41
0.01	0.01	0.01	0.01	0.01
0.00	0.00	0.00	0.00	0.00
4.98	**4.98**	**5.01**	**4.98**	**4.97**
55	55	55	55	58
44	43	43	44	40
1	2	2	1	2

Plagioclase mineral compositional data continued

Depth(m)	143	143	143	143	143
Sample	P1_plag4	P1_plag5	P1_plag9	P1_plag10	P1_plag11
SiO_2	54.61	54.22	54.65	54.93	54.21
Al_2O_3	27.94	27.59	28.21	29.16	28.44
FeO	0.34	0.29	0.30	0.41	0.34
CaO	11.93	12.09	12.16	12.27	12.00
Na_2O	4.84	4.73	4.66	4.72	4.76
K_2O	0.23	0.20	0.30	0.28	0.25
BaO	0.00	0.00	0.00	0.00	0.00
Total	**99.88**	**99.12**	**100.28**	**101.76**	**99.99**
Si	2.47	2.47	2.46	2.46	2.45
Al	1.49	1.49	1.50	1.53	1.51
Fe	0.01	0.01	0.01	0.01	0.01
Ca	0.58	0.59	0.59	0.58	0.58
Na	0.42	0.41	0.40	0.40	0.41
K	0.01	0.01	0.01	0.01	0.01
Ba	0.00	0.00	0.00	0.00	0.00
Total	**4.98**	**4.98**	**4.97**	**4.99**	**4.97**
An	57	58	58	58	57
Ab	42	41	40	40	41
Or	1	1	2	2	2

143	143	143	143	143
P1_plag12	P1_plag8	P1_plag16	P1_plag20	P1_plag21
54.28	54.05	55.20	54.24	54.80
28.37	27.90	27.79	27.61	27.52
0.22	0.21	0.34	0.20	0.37
12.13	12.16	12.01	11.89	11.93
4.72	4.71	4.79	4.88	4.85
0.32	0.31	0.31	0.22	0.29
0.00	0.00	0.00	0.00	0.00
100.04	**99.33**	**100.42**	**99.03**	**99.76**
2.45	2.46	2.48	2.47	2.48
1.51	1.50	1.47	1.48	1.47
0.01	0.01	0.01	0.01	0.01
0.58	0.59	0.58	0.58	0.58
0.41	0.41	0.41	0.43	0.42
0.01	0.01	0.01	0.01	0.01
0.00	0.00	0.00	0.00	0.00
4.97	**4.98**	**4.96**	**4.98**	**4.97**
57	58	57	57	57
41	40	41	42	42
2	2	2	1	1

Plagioclase mineral compositional data continued

Depth(m)	143	143	143	143	134.5
Sample	P1_plag22	P1_plag23	P1_plag24	P1_plag26	OBSZ6_plag1
SiO_2	54.67	54.29	54.61	54.20	54.40
Al_2O_3	27.01	27.40	27.34	27.66	27.28
FeO	0.14	0.27	0.21	0.25	0.42
CaO	11.60	12.18	12.03	12.22	11.42
Na_2O	4.87	4.87	4.41	4.78	4.60
K_2O	0.27	0.30	0.25	0.21	0.37
BaO	0.00	0.00	0.00	0.00	0.00
Total	**98.55**	**99.30**	**98.84**	**99.32**	**98.48**
Si	2.50	2.48	2.49	2.47	2.49
Al	1.46	1.47	1.47	1.48	1.47
Fe	0.01	0.01	0.01	0.01	0.01
Ca	0.57	0.60	0.59	0.59	0.56
Na	0.43	0.43	0.39	0.42	0.41
K	0.01	0.01	0.01	0.01	0.02
Ba	0.00	0.00	0.00	0.00	0.00
Total	**4.98**	**5.00**	**4.96**	**4.98**	**4.96**
An	56	57	59	58	57
Ab	41	41	39	41	41
Or	3	2	2	1	2

134.5	134.5	134.5	134.5	134.5
OBSZ6_plag2	OBSZ6_plag3	OBSZ6_plag6	OBSZ6_plag7	OBSZ6_plag8
55.18	54.25	54.41	55.20	55.81
27.37	28.14	27.76	28.83	29.02
0.43	0.32	0.40	0.36	0.19
11.53	12.03	11.66	11.68	11.08
4.86	4.89	4.90	4.94	5.19
0.44	0.30	0.36	0.50	0.30
0.00	0.00	0.00	0.00	0.00
99.80	**99.93**	**99.50**	**101.51**	**101.58**
2.50	2.46	2.47	2.46	2.48
1.46	1.50	1.49	1.51	1.51
0.01	0.01	0.01	0.01	0.01
0.56	0.58	0.57	0.56	0.52
0.42	0.43	0.43	0.42	0.44
0.02	0.01	0.02	0.02	0.01
0.00	0.00	0.00	0.00	0.00
4.97	**4.99**	**4.99**	**4.98**	**4.97**
55	57	56	55	53
42	42	42	42	45
2	1	2	3	2

Plagioclase mineral compositional data continued

Depth(m)	134.5	134.5	134.5	134.5	134.5
Sample	OBSZ6_plag9	OBSZ6_plag11	OBSZ6_plag12	OBSZ6_plag14	OBSZ6_plag16
SiO_2	54.34	53.84	53.80	54.27	54.36
Al_2O_3	28.17	28.46	28.07	27.59	28.50
FeO	0.29	0.29	0.12	0.37	0.23
CaO	11.71	11.81	11.77	11.80	11.84
Na_2O	4.90	4.96	4.78	4.89	4.69
K_2O	0.41	0.35	0.44	0.38	0.37
BaO	0.00	0.00	0.00	0.00	0.00
Total	**99.82**	**99.71**	**98.99**	**99.30**	**100.00**
Si	2.46	2.44	2.46	2.47	2.46
Al	1.50	1.52	1.51	1.48	1.52
Fe	0.01	0.01	0.01	0.01	0.01
Ca	0.57	0.57	0.57	0.57	0.57
Na	0.43	0.43	0.42	0.43	0.41
K	0.02	0.02	0.02	0.02	0.02
Ba	0.00	0.00	0.00	0.00	0.00
Total	**4.99**	**4.99**	**4.99**	**4.98**	**4.99**
An	56	56	56	56	57
Ab	42	42	41	42	41
Or	2	2	3	2	2

134.5	134.5	134.5	134.5	134.5
OBSZ6_plag17	OBSZ6_plag18	OBSZ6_plag19	OBSZ6_plag20	OBSZ6_plag21
55.07	55.48	55.17	54.50	53.62
27.88	28.32	29.19	28.41	28.46
0.25	0.37	0.27	1.12	0.37
11.19	11.59	11.97	11.70	12.08
5.13	5.12	4.69	4.79	4.71
0.42	0.51	0.44	0.40	0.36
0.00	0.00	0.00	0.00	0.00
99.94	**101.38**	**101.73**	**100.93**	**99.61**
2.49	2.48	2.45	2.45	2.44
1.48	1.49	1.53	1.51	1.52
0.01	0.01	0.01	0.04	0.01
0.54	0.55	0.57	0.56	0.59
0.45	0.44	0.40	0.41	0.41
0.02	0.02	0.02	0.02	0.02
0.00	0.00	0.00	0.00	0.00
4.99	**4.99**	**4.98**	**4.99**	**4.99**
53	54	57	56	57
44	43	40	42	41
3	3	3	2	2

Plagioclase mineral compositional data continued

Depth(m)	134.5	134.5	134.5	134.5
Sample	OBSZ6_plag22	OBSZ6_plag23	OBSZ6_plag24	OBSZ6_plag25
SiO_2	53.91	55.46	54.88	54.58
Al_2O_3	27.59	28.58	29.15	28.72
FeO	0.51	0.52	0.28	0.36
CaO	11.73	9.21	11.81	11.82
Na_2O	4.86	4.34	4.78	4.97
K_2O	0.51	1.58	0.42	0.32
BaO	0.00	0.00	0.00	0.00
Total	**99.11**	**99.68**	**101.32**	**100.78**
Si	2.47	2.50	2.45	2.45
Al	1.49	1.52	1.53	1.52
Fe	0.01	0.01	0.01	0.01
Ca	0.57	0.45	0.56	0.57
Na	0.43	0.38	0.41	0.43
K	0.02	0.09	0.02	0.01
Ba	0.00	0.00	0.00	0.00
Total	**4.99**	**4.95**	**4.98**	**4.99**
An	56	49	56	56
Ab	42	41	41	42
Or	2	10	3	2

63.1 WG4_plag4	63.1 WG4_plag8	63.1 WG4_plag9	20.8 LS1_altplag2	20.8 LS1_altplag3
54.90	55.26	55.20	54.91	54.14
26.53	28.01	27.28	26.92	27.62
0.42	0.36	0.27	0.28	0.28
11.17	11.72	11.53	11.00	12.11
5.21	4.92	4.96	5.25	4.82
0.30	0.27	0.38	0.24	0.14
0.00	0.00	0.00	0.00	0.00
98.53	**100.54**	**99.62**	**98.60**	**99.10**
2.52	2.48	2.50	2.51	2.47
1.43	1.48	1.46	1.45	1.48
0.01	0.01	0.01	0.01	0.01
0.55	0.56	0.56	0.54	0.59
0.46	0.42	0.43	0.47	0.42
0.01	0.01	0.02	0.01	0.01
0.00	0.00	0.00	0.00	0.00
4.98	**4.96**	**4.98**	**4.99**	**4.98**
53	56	55	53	57
45	43	43	46	42
2	1	2	1	1

Plagioclase mineral compositional data continued

Depth (m)	20.8	20.8	20.8
Sample	LS1_altplag4	LS1_altplag8	LS1_altplag11
SiO_2	53.85	55.09	54.60
Al_2O_3	27.94	27.47	28.65
FeO	0.16	0.30	0.30
CaO	11.94	10.96	11.49
Na_2O	4.60	5.11	4.87
K_2O	0.07	0.15	0.15
BaO	0.00	0.00	0.00
Total	**98.56**	**99.09**	**100.06**
Si	2.47	2.50	2.46
Al	1.51	1.47	1.52
Fe	0.01	0.01	0.01
Ca	0.58	0.53	0.55
Na	0.41	0.45	0.42
K	0.00	0.01	0.01
Ba	0.00	0.00	0.00
Total	**4.98**	**4.97**	**4.97**
An	59	54	56
Ab	41	45	43
Or	0	1	1

20.8	20.8	20.8	20.8
LS1_altplag13	LS1_altplag15	LS1_altplag16	LS1_altplag20
52.12	56.14	54.25	54.05
31.12	28.87	28.45	27.84
0.15	0.37	0.42	0.44
13.47	10.91	11.88	11.78
3.84	5.16	4.78	4.93
0.07	0.11	0.16	0.13
0.00	0.00	0.00	0.00
100.75	**101.56**	**99.93**	**99.16**
2.34	2.49	2.45	2.46
1.65	1.51	1.51	1.49
0.01	0.01	0.01	0.01
0.65	0.51	0.57	0.57
0.33	0.44	0.42	0.43
0.00	0.01	0.01	0.00
0.00	0.00	0.00	0.00
4.98	**4.97**	**4.97**	**4.96**
66	53	57	57
34	46	42	43
0	1	1	0

Pyroxene mineral compositional data

Depth(m)	148	148	148	148
Sample	BS1_pyx1	BS1_pyx2	BS1_pyx3	BS1_pyx4
SiO_2	51.91	52.19	50.59	52.14
TiO_2	0.42	0.42	0.40	0.38
Al_2O_3	1.66	1.69	1.65	1.58
Cr_2O_3	0.17	0.18	0.19	0.26
FeO	9.09	10.93	9.95	8.67
MnO	0.20	0.35	0.00	0.06
MgO	14.79	15.64	14.30	15.09
CaO	21.54	18.76	21.49	22.07
Na_2O	0.20	0.14	0.24	0.19
Total	**99.98**	**100.30**	**98.81**	**100.44**
Si	1.93	1.94	1.92	1.93
Ti	0.01	0.01	0.01	0.01
Al	0.07	0.07	0.07	0.07
Cr	0.01	0.01	0.01	0.01
Fe	0.28	0.34	0.31	0.27
Mn	0.01	0.01	0.00	0.00
Mg	0.82	0.87	0.81	0.83
Ca	0.86	0.74	0.86	0.88
Na	0.01	0.01	0.01	0.00
Total	**4.00**	**4.00**	**4.00**	**4.00**
En	42	44	40	42
Wo	44	38	44	44
Fe	14	18	16	14
Mg#	74	72	72	76

148	148	148	148	148
BS1_pyx5	BS1_pyx6	BS1_pyx7	BS1_pyx8	BS1_pyx11
53.05	52.56	52.35	51.66	52.60
0.24	0.38	0.48	0.39	0.54
0.93	1.74	1.65	1.65	1.96
0.11	0.12	0.19	0.15	0.14
20.74	9.72	9.44	7.90	9.66
0.41	0.09	0.50	0.35	0.14
23.50	15.29	14.83	15.33	14.67
1.36	21.54	21.08	21.11	21.06
0.00	0.15	0.23	0.18	0.23
100.34	**101.58**	**100.76**	**98.72**	**101.01**
1.95	1.93	1.94	1.94	1.94
0.01	0.01	0.01	0.01	0.01
0.04	0.07	0.07	0.07	0.08
0.00	0.01	0.01	0.00	0.00
0.64	0.29	0.29	0.25	0.30
0.01	0.00	0.01	0.01	0.00
1.29	0.83	0.82	0.86	0.81
0.05	0.85	0.83	0.85	0.83
0.01	0.01	0.01	0.01	0.01
4.00	**4.00**	**3.99**	**4.00**	**3.98**
65	42	42	44	42
3	43	43	43	43
33	15	15	13	15
67	74	74	78	73

Pyroxene mineral compositional data continued

Depth(m)	145	145	145	145
Sample	OFSZ4_pyx3	OFSZ4_pyx4	OFSZ4_pyx5	OFSZ4_pyx6
SiO_2	50.06	50.27	50.46	51.00
TiO_2	0.21	0.48	0.43	0.40
Al_2O_3	0.70	1.56	1.56	1.55
Cr_2O_3	0.00	0.03	0.05	0.00
FeO	25.37	12.84	12.90	12.43
MnO	0.59	0.16	0.38	0.33
MgO	17.84	13.06	13.36	13.28
CaO	4.22	22.17	20.42	21.82
Na_2O	0.01	0.19	0.15	0.22
Total	**99.00**	**100.76**	**99.69**	**101.02**
Si	1.92	1.88	1.91	1.90
Ti	0.01	0.01	0.01	0.01
Al	0.03	0.07	0.07	0.07
Cr	0.00	0.00	0.00	0.00
Fe	0.82	0.41	0.41	0.39
Mn	0.02	0.01	0.01	0.01
Mg	1.03	0.73	0.76	0.74
Ca	0.17	0.90	0.84	0.88
Na	0.00	0.01	0.01	0.01
Total	**4.00**	**4.02**	**4.02**	**4.01**
En	50	36	38	37
Wo	9	44	41	43
Fe	41	20	21	20
Mg#	56	64	65	66

145	145	143	143	143	143
OFSZ4_pyx7	OFSZ4_pyx8	P1_pyx1	P1_pyx2	P1_pyx3	P1_pyx4
50.13	50.04	51.04	51.97	51.74	51.81
0.42	0.37	0.31	0.20	0.30	0.31
1.46	1.37	1.23	0.94	1.33	1.56
0.00	0.00	0.21	0.16	0.16	0.16
12.20	11.65	11.50	9.90	13.36	11.60
0.82	0.18	0.40	0.36	0.54	0.20
13.42	13.32	12.91	13.35	13.49	12.76
22.14	22.72	22.85	22.93	20.79	23.06
0.15	0.19	0.22	0.20	0.15	0.24
100.73	**99.84**	**100.66**	**100.01**	**101.87**	**101.71**
1.87	1.88	1.92	1.96	1.93	1.93
0.01	0.01	0.01	0.01	0.01	0.01
0.06	0.06	0.05	0.04	0.05	0.06
0.00	0.00	0.01	0.00	0.00	0.00
0.38	0.37	0.36	0.31	0.41	0.36
0.02	0.01	0.01	0.01	0.01	0.01
0.75	0.75	0.72	0.75	0.75	0.71
0.90	0.92	0.92	0.92	0.83	0.92
0.01	0.01	0.01	0.01	0.01	0.01
4.00	**4.01**	**4.01**	**4.01**	**4.00**	**4.01**
37	37	36	38	37	35
43	45	46	46	41	46
20	18	18	16	22	19
66	67	67	70	64	66

Pyroxene mineral compositional data continued

Depth(m)	143	143	143	143	143
Sample	P1_pyx5	P1_pyx7	P1_pyx9	P1_pyx10	P1_pyx11
SiO_2	51.15	51.11	51.62	51.67	50.26
TiO_2	0.33	0.36	0.14	0.21	0.15
Al_2O_3	1.52	2.31	0.64	0.99	0.57
Cr_2O_3	0.15	0.21	0.14	0.10	0.19
FeO	11.30	11.79	27.94	14.82	27.35
MnO	0.47	0.59	0.36	0.28	0.74
MgO	12.76	12.63	19.14	15.17	18.88
CaO	22.60	21.82	0.93	16.38	1.26
Na_2O	0.22	0.20	0.00	0.12	0.00
Total	**100.50**	**101.02**	**100.89**	**99.74**	**99.40**
Si	1.93	1.91	1.96	1.96	1.95
Ti	0.01	0.01	0.00	0.01	0.00
Al	0.06	0.10	0.02	0.04	0.02
Cr	0.00	0.01	0.00	0.00	0.01
Fe	0.35	0.37	0.88	0.47	0.88
Mn	0.01	0.01	0.01	0.01	0.02
Mg	0.71	0.71	1.08	0.85	1.08
Ca	0.91	0.87	0.03	0.66	0.05
Na	0.01	0.01	0.00	0.01	0.00
Total	**3.99**	**4.00**	**3.98**	**4.01**	**4.01**
En	36	36	54	43	53
Wo	46	44	2	33	3
Fe	18	20	44	24	44
Mg#	67	66	55	65	55

143 P1_pyx12	143 P1_pyx13	143 P1_pyx14	143 P1_pyx16	143 P1_pyx17
50.42	51.57	51.58	51.75	50.44
0.17	0.25	0.26	0.24	0.16
0.57	1.18	1.18	0.91	0.59
0.18	0.18	0.15	0.13	0.13
27.63	10.76	10.90	17.48	29.35
1.00	0.44	0.45	0.72	0.54
19.50	13.42	13.48	15.58	19.13
0.77	22.37	22.59	14.23	0.80
0.00	0.15	0.18	0.11	0.01
100.24	**100.32**	**100.76**	**101.14**	**101.14**
1.93	1.94	1.94	1.94	1.94
0.00	0.01	0.01	0.01	0.00
0.02	0.05	0.05	0.04	0.02
0.01	0.01	0.00	0.00	0.00
0.88	0.34	0.34	0.55	0.94
0.03	0.01	0.01	0.02	0.01
1.11	0.75	0.75	0.87	1.09
0.03	0.90	0.91	0.57	0.03
0.00	0.01	0.01	0.01	0.00
4.01	**4.02**	**4.02**	**4.01**	**4.03**
54	38	37	37	43
2	45	45	28	2
44	17	17	25	45
58	69	69	61	54

Pyroxene mineral compositional data continued

Depth(m)	143	143	143	143	143
Sample	P1_pyx32	P1_pyx19	P1_pyx20	P1_pyx21	P1_pyx22
SiO_2	51.98	51.70	50.38	51.14	51.26
TiO_2	0.34	0.15	0.27	0.26	0.24
Al_2O_3	1.57	0.63	1.37	1.26	1.39
Cr_2O_3	0.12	0.02	0.00	0.14	0.10
FeO	11.35	25.70	10.98	11.63	10.94
MnO	0.54	1.27	0.44	0.22	0.38
MgO	13.03	19.04	13.29	13.28	12.93
CaO	22.53	0.76	22.24	22.72	22.12
Na_2O	0.22	0.00	0.15	0.22	0.18
Total	**101.67**	**99.28**	**99.11**	**100.86**	**99.53**
Si	1.94	1.98	1.92	1.92	1.94
Ti	0.01	0.00	0.01	0.01	0.01
Al	0.06	0.02	0.06	0.05	0.06
Cr	0.01	0.00	0.00	0.00	0.00
Fe	0.35	0.82	0.35	0.36	0.34
Mn	0.01	0.04	0.01	0.01	0.01
Mg	0.72	1.08	0.75	0.75	0.74
Ca	0.90	0.03	0.91	0.91	0.90
Na	0.01	0.00	0.01	0.01	0.01
Total	**4.01**	**3.97**	**4.02**	**4.02**	**4.01**
En	36	55	37	37	37
Wo	45	2	45	45	45
Fe	19	43	18	18	18
Mg#	67	57	68	67	68

143 P1_pyx23	143 P1_pyx24	143 P1_pyx25	143 P1_pyx26	143 P1_pyx27
51.72	50.49	50.82	50.86	51.34
0.13	0.40	0.40	0.35	0.18
0.61	1.78	1.61	1.55	0.85
0.14	0.09	0.13	0.14	0.13
27.24	15.23	11.96	11.18	9.92
0.80	0.30	0.58	0.42	0.58
19.16	13.17	12.71	12.83	13.26
0.95	17.94	22.86	22.03	23.14
0.00	0.13	0.27	0.21	0.21
100.73	**99.51**	**101.33**	**99.57**	**99.61**
1.96	1.93	1.91	1.93	1.94
0.00	0.01	0.01	0.01	0.03
0.02	0.08	0.07	0.06	0.03
0.00	0.00	0.00	0.00	0.00
0.86	0.48	0.37	0.35	0.31
0.02	0.01	0.01	0.01	0.01
1.08	0.75	0.71	0.72	0.75
0.03	0.73	0.92	0.89	0.94
0.00	0.01	0.01	0.01	0.01
3.97	**4.00**	**4.01**	**3.98**	**4.02**
54	38	35	36	37
2	37	45	45	47
44	25	20	19	16
56	61	65	67	70

Pyroxene mineral compositional data continued

Depth(m)	143	143	118.2	118.2	118.2
Sample	P1_pyx30	P1_pyx31	OHSZ5_pyx1	OHSZ5_pyx3	OHSZ5_pyx4
SiO_2	50.23	52.53	51.73	51.07	52.09
TiO_2	0.37	0.22	0.24	0.26	0.21
Al_2O_3	1.58	1.00	0.81	0.75	0.75
Cr_2O_3	0.06	0.03	0.04	0.01	0.02
FeO	11.82	11.61	26.05	26.79	26.46
MnO	0.48	0.48	0.98	0.46	0.49
MgO	12.48	13.39	19.73	19.32	19.95
CaO	21.94	22.14	1.42	1.41	1.36
Na_2O	0.22	0.19	0.00	0.00	0.03
Total	**99.18**	**101.58**	**100.99**	**100.07**	**101.35**
Si	1.92	1.95	1.95	1.95	1.95
Ti	0.01	0.01	0.01	0.01	0.01
Al	0.07	0.04	0.03	0.03	0.03
Cr	0.00	0.00	0.00	0.00	0.00
Fe	0.37	0.36	0.81	0.85	0.83
Mn	0.01	0.01	0.03	0.01	0.01
Mg	0.71	0.74	1.11	1.10	1.10
Ca	0.90	0.88	0.05	0.05	0.05
Na	0.01	0.01	0.05	0.00	0.00
Total	**4.00**	**4.00**	**4.04**	**4.00**	**3.98**
En	35	37	55	54	55
Wo	45	44	3	3	3
Fe	20	19	42	43	42
Mg#	65	67	57	56	57

118.2	118.2	118.2	118.2	118.2
OHSZ5_pyx5	OHSZ5_pyx6	OHSZ5_pyx7	OHSZ5_pyx8	OHSZ5_pyx9
51.94	51.76	51.89	52.20	52.17
0.22	0.47	0.43	0.46	0.42
0.74	1.80	1.61	1.45	1.49
0.01	0.00	0.00	0.00	0.04
27.48	12.18	12.82	11.00	11.60
0.64	0.43	0.22	0.44	0.30
19.52	12.93	13.43	13.51	13.50
1.22	22.21	21.30	21.94	21.72
0.00	0.17	0.19	0.16	0.15
101.76	**101.95**	**101.88**	**101.16**	**101.40**
1.95	1.92	1.93	1.94	1.94
0.01	0.01	0.01	0.01	0.01
0.03	0.07	0.07	0.06	0.06
0.00	0.00	0.00	0.00	0.00
0.86	0.37	0.40	0.34	0.36
0.02	0.01	0.01	0.01	0.01
1.09	0.71	0.74	0.75	0.75
0.04	0.88	0.84	0.87	0.87
0.00	0.01	0.01	0.01	0.01
4.00	**3.98**	**4.01**	**3.99**	**4.01**
54	36	37	38	38
2	44	43	44	44
44	20	20	18	18
56	65	65	68	67

Pyroxene mineral compositional data continued

Depth(m)	63.1	63.1	63.1	63.1
Sample	WG4_pyx1	WG4_pyx2	WG4_pyx4	WG4_pyx5
SiO_2	51.24	51.57	50.89	50.12
TiO_2	0.56	0.55	0.58	0.19
Al_2O_3	2.09	1.99	1.87	0.53
Cr_2O_3	0.01	0.07	0.01	0.04
FeO	11.29	12.79	13.54	29.33
MnO	0.44	0.14	0.44	1.02
MgO	12.61	12.75	13.25	17.44
CaO	21.54	21.53	19.14	1.03
Na_2O	0.18	0.23	0.19	0.00
Total	**99.94**	**101.61**	**99.90**	**99.71**
Si	1.93	1.92	1.93	1.95
Ti	0.01	0.01	0.01	0.01
Al	0.09	0.08	0.08	0.02
Cr	0.00	0.00	0.00	0.00
Fe	0.35	0.40	0.43	0.95
Mn	0.01	0.00	0.01	0.03
Mg	0.71	0.71	0.75	1.01
Ca	0.87	0.86	0.78	0.04
Na	0.01	0.01	0.01	0.00
Total	**3.98**	**3.99**	**4.00**	**4.01**
En	36	36	38	50
Wo	45	44	39	2
Fe	19	20	23	48
Mg#	67	64	64	51

63.1 WG4_pyx6	63.1 WG4_pyx7	63.1 WG4_pyx10	63.1 WG4_pyx11	63.1 WG4_pyx12
51.93	51.60	50.82	51.36	52.51
0.47	0.19	0.52	0.52	0.22
1.67	0.47	1.60	1.76	0.79
0.04	0.06	0.04	0.00	0.04
12.27	28.89	10.68	12.84	24.56
0.22	0.74	0.46	0.08	0.63
12.83	17.41	12.55	12.73	15.97
22.37	0.85	21.85	20.95	6.20
0.19	0.00	0.19	0.16	0.07
101.98	**100.22**	**98.70**	**100.40**	**100.99**
1.93	1.98	1.94	1.93	1.99
0.01	0.01	0.01	0.01	0.01
0.07	0.02	0.07	0.07	0.03
0.00	0.00	0.00	0.00	0.00
0.38	0.93	0.34	0.40	0.78
0.01	0.02	0.01	0.00	0.02
0.71	0.99	0.71	0.71	0.90
0.89	0.03	0.89	0.84	0.25
0.01	0.00	0.01	0.01	0.01
4.01	**3.98**	**3.98**	**3.97**	**3.99**
36	50	36	36	46
45	2	46	43	13
19	48	18	21	41
65	52	67	67	54

Ilmenite mineral compositional data

Depth (m)	148.1	148.1	148.1	148.1
Sample	AN5_ilm2	AN5_ilm3	AN5_ilm4	AN5_ilm5
Al_2O_3	0.01	0.01	0.01	0.01
SiO_2	0.03	0.03	0.02	0.01
MgO	0.07	0.04	0.06	0.04
FeO	45.56	47.87	46.33	46.52
MnO	0.91	1.09	1.12	1.06
V_2O_3	0.13	0.22	0.21	0.08
Cr_2O_3	0.00	0.00	0.00	0.00
TiO_2	52.02	51.83	51.97	51.39
Total	**98.71**	**101.09**	**99.71**	**99.11**
Al	0.00	0.00	0.00	0.00
Si	0.00	0.00	0.00	0.00
Mg	0.00	0.00	0.00	0.00
Fe	0.63	0.67	0.65	0.65
Mn	0.01	0.02	0.02	0.02
V	0.00	0.00	0.00	0.00
Cr	0.00	0.00	0.00	0.00
Ti	1.30	1.30	1.30	1.30
Total	**1.95**	**1.98**	**1.96**	**1.96**

148.1	148.1	147.8	147.2	147.2	147.2
AN5_ilm6	AN5_ilm7	BS2_ilm1	BS5_ilm3	BS5_ilm4	BS5_ilm5
0.01	0.00	0.03	0.05	0.02	0.08
0.00	0.01	0.02	0.04	0.00	0.02
0.01	0.10	4.07	2.45	2.77	2.42
45.71	46.94	41.86	44.91	43.11	44.40
1.28	1.20	0.36	0.49	0.23	0.53
0.42	0.18	0.25	0.23	0.48	0.29
0.06	0.00	0.00	0.00	0.00	0.17
51.61	51.63	53.63	52.88	52.57	53.70
99.10	**100.06**	**100.23**	**101.05**	**99.17**	**101.60**
0.00	0.00	0.00	0.00	0.00	0.00
0.00	0.00	0.00	0.00	0.00	0.00
0.00	0.00	0.00	0.10	0.07	0.06
0.65	0.64	0.65	0.58	0.60	0.62
0.02	0.02	0.02	0.01	0.00	0.01
0.00	0.00	0.00	0.00	0.00	0.00
0.00	0.00	0.00	0.00	0.00	0.00
1.29	1.29	1.29	1.34	1.32	1.34
1.95	**1.95**	**1.97**	**2.04**	**1.99**	**2.03**

Ilmenite mineral compositional data continued

Depth(m)	147.2	147.2	147.2	147.2	147.2
Sample	BS5_ilm6	BS5_ilm7	BS5_ilm8	BS5_ilm9	BS5_ilm10
Al_2O_3	0.04	0.02	0.07	0.04	0.04
SiO_2	0.02	0.03	0.00	0.11	0.03
MgO	2.62	2.83	2.74	2.80	2.78
FeO	45.07	43.31	44.82	44.10	43.90
MnO	0.59	0.59	0.39	0.75	0.50
V_2O_3	0.30	0.23	0.38	0.38	0.14
Cr_2O_3	0.02	0.25	0.00	0.90	0.00
TiO_2	53.32	53.20	53.03	52.12	52.71
Total	**101.99**	**100.47**	**101.44**	**101.12**	**100.10**
Al	0.00	0.00	0.00	0.00	0.00
Si	0.00	0.00	0.00	0.00	0.00
Mg	0.07	0.07	0.07	0.07	0.07
Fe	0.63	0.60	0.62	0.61	0.61
Mn	0.01	0.01	0.01	0.01	0.01
V	0.00	0.00	0.00	0.01	0.00
Cr	0.00	0.00	0.00	0.00	0.00
Ti	1.34	1.33	1.33	1.31	1.32
Total	**2.04**	**2.02**	**2.03**	**2.01**	**2.01**

147.2	147.2	147.2	145.5	145.5
BS5_ilm11	BS5_ilm12	BS5_ilm13	OFSZ4_ilm1	OFSZ4_ilm3
0.11	0.03	0.01	0.03	0.06
0.05	0.03	0.02	0.05	0.01
2.08	2.58	2.65	1.72	0.74
43.21	42.97	41.31	43.24	44.43
0.62	0.36	0.33	0.71	0.97
0.26	0.18	0.29	0.04	0.30
0.00	0.37	0.02	0.00	0.00
52.15	52.22	53.31	52.81	52.54
98.48	**98.74**	**97.95**	**98.60**	**99.04**
0.00	0.00	0.00	0.00	0.00
0.00	0.00	0.00	0.00	0.00
0.05	0.06	0.07	0.04	0.02
0.60	0.60	0.58	0.60	0.62
0.01	0.01	0.01	0.01	0.01
0.00	0.00	0.00	0.00	0.00
0.00	0.00	0.00	0.00	0.00
1.31	1.31	1.34	1.32	1.32
1.98	**1.98**	**1.98**	**1.98**	**1.97**

Ilmenite mineral compositional data continued

Depth(m)	145.5	145.5	145.5	134.5	134.5
Sample	OFSZ4_ilm4	OFSZ4_ilm5	OFSZ4_ilm6	OBSZ6_ilm12	OBSZ6_ilm2
Al_2O_3	0.00	0.03	0.05	0.01	0.00
SiO_2	0.04	0.02	0.03	0.02	0.01
MgO	1.38	2.00	1.64	0.92	0.66
FeO	45.51	44.59	44.43	45.94	46.45
MnO	1.08	0.76	0.62	0.43	0.65
V_2O_3	0.31	0.17	0.30	0.00	0.16
Cr_2O_3	0.61	0.00	0.66	0.00	0.00
TiO_2	53.01	53.06	52.18	52.35	52.38
Total	**101.93**	**100.63**	**99.90**	**99.67**	**100.31**
Al	0.00	0.00	0.00	0.00	0.00
Si	0.00	0.00	0.00	0.00	0.00
Mg	0.03	0.05	0.04	0.02	0.02
Fe	0.63	0.62	0.62	0.64	0.65
Mn	0.02	0.01	0.01	0.01	0.01
V	0.00	0.00	0.00	0.00	0.00
Cr	0.00	0.00	0.00	0.00	0.00
Ti	1.33	1.33	1.31	1.31	1.31
Total	**2.02**	**2.01**	**1.98**	**1.98**	**1.98**

134.5	134.5	134.5	134.5	134.5
OBSZ6_ilm3	OBSZ6_ilm5	OBSZ6_ilm6	OBSZ6_ilm7	OBSZ6_ilm8
0.03	0.04	0.03	0.01	0.05
0.03	0.00	0.00	0.02	0.01
0.65	0.84	0.57	1.22	1.25
46.63	46.11	46.29	44.70	44.63
0.66	0.39	0.66	0.87	0.36
0.35	0.11	0.13	0.34	0.31
0.31	0.00	0.00	0.06	0.56
52.33	52.67	51.98	52.35	52.54
100.98	**100.16**	**99.66**	**99.57**	**99.70**
0.00	0.00	0.00	0.00	0.00
0.00	0.00	0.00	0.00	0.00
0.02	0.02	0.01	0.03	0.03
0.65	0.64	0.64	0.62	0.62
0.01	0.01	0.01	0.01	0.01
0.00	0.00	0.00	0.00	0.00
0.00	0.00	0.00	0.00	0.00
1.31	1.32	1.30	1.31	1.32
1.99	**1.99**	**1.97**	**1.98**	**1.98**

Ilmenite mineral compositional data continued

Depth(m)	134.5	134.5	118.2	118.2
Sample	OBSZ6_ilm9	OBSZ6_ilm10	OHSZ5_ilm1	OHSZ5_ilm2
Al_2O_3	0.02	0.04	0.00	0.00
SiO_2	0.01	0.02	0.02	0.02
MgO	1.13	1.34	1.93	1.04
FeO	46.49	46.80	44.06	45.80
MnO	0.53	0.30	0.66	0.80
V_2O_3	0.06	0.42	0.37	0.12
Cr_2O_3	0.00	0.37	0.00	0.00
TiO_2	52.31	51.91	52.72	52.07
Total	**100.54**	**101.21**	**99.77**	**99.85**
Al	0.00	0.00	0.00	0.00
Si	0.00	0.00	0.00	0.00
Mg	0.03	0.03	0.05	0.03
Fe	0.65	0.65	0.61	0.64
Mn	0.01	0.00	0.01	0.01
V	0.00	0.00	0.00	0.00
Cr	0.00	0.00	0.00	0.00
Ti	1.31	1.30	1.32	1.30
Total	**1.99**	**2.00**	**1.99**	**1.98**

63.1	63.1	63.1	63.1	20.8	20.8
WG4_ilm5	WG4_ilm6	WG4_ilm7	WG4_ilm9	LS5_ilm1	LS5_ilm3
0.04	0.04	0.01	0.01	0.05	0.02
0.00	0.00	0.01	0.00	0.04	0.00
1.84	1.65	1.38	1.44	2.56	2.24
45.18	43.87	45.54	45.63	44.08	43.44
0.61	0.49	0.97	0.74	0.42	0.42
0.44	0.13	0.44	0.24	0.54	0.25
0.00	0.00	0.00	0.26	0.00	0.00
53.23	52.78	52.30	52.30	52.98	52.60
101.34	**98.96**	**100.64**	**100.62**	**100.66**	**98.97**
0.00	0.00	0.00	0.00	0.00	0.00
0.00	0.00	0.00	0.00	0.00	0.00
0.05	0.04	0.03	0.04	0.06	0.06
0.63	0.61	0.63	0.64	0.61	0.61
0.01	0.01	0.01	0.01	0.01	0.01
0.00	0.00	0.00	0.00	0.00	0.00
0.00	0.00	0.00	0.00	0.00	0.00
1.33	1.32	1.31	1.31	1.33	1.32
2.02	**1.98**	**1.99**	**2.00**	**2.02**	**1.99**

Ilmenite mineral compositional data continued

Depth (m)	20.8	20.8	20.8
Sample	LS5_ilm4	LS5_ilm6	LS5_ilm7
Al_2O_3	0.04	0.05	0.03
SiO_2	0.00	0.01	0.00
MgO	2.14	2.39	2.64
FeO	44.38	44.92	44.09
MnO	0.45	0.36	0.20
V_2O_3	0.44	0.23	0.28
Cr_2O_3	0.00	0.00	0.51
TiO_2	53.32	52.63	52.94
Total	**100.77**	**100.59**	**100.70**
Al	0.00	0.00	0.00
Si	0.00	0.00	0.00
Mg	0.05	0.06	0.07
Fe	0.62	0.63	0.61
Mn	0.01	0.01	0.00
V	0.00	0.00	0.00
Cr	0.00	0.00	0.00
Ti	1.34	1.32	1.33
Total	**2.02**	**2.01**	**2.02**

20.8	20.8	20.8	20.8
LS5_ilm8	LS5_ilm10	LS5_ilm11	LS5_ilm12
0.05	0.03	0.05	0.05
0.00	0.00	0.03	0.00
2.11	2.80	2.52	2.61
43.82	44.07	43.19	44.09
0.44	0.31	0.49	0.41
0.28	0.27	0.31	0.60
0.16	0.00	0.00	0.00
52.35	53.04	52.60	52.63
99.21	**100.53**	**99.19**	**100.39**
0.00	0.00	0.00	0.00
0.00	0.00	0.00	0.00
0.05	0.07	0.06	0.07
0.61	0.61	0.60	0.61
0.01	0.00	0.01	0.01
0.00	0.00	0.00	0.00
0.00	0.00	0.00	0.00
1.31	1.33	1.32	1.32
1.98	**2.02**	**1.99**	**2.01**

Ti-magnetite mineral compositional data

Depth(m)	148	148	148	148	148
Sample	BS1_mag1	BS1_mag3	BS1_mag4	BS1_mag5	BS1_mag6
Al_2O_3	2.08	2.49	2.26	1.49	3.98
SiO_2	0.06	0.05	0.04	0.04	0.03
MgO	1.14	1.29	0.38	1.01	1.69
FeO	79.20	78.54	82.95	76.53	73.29
MnO	0.19	0.15	0.22	0.25	0.17
V_2O_3	0.74	0.68	1.09	1.04	0.82
Cr_2O_3	1.36	0.02	0.57	0.19	0.07
TiO_2	10.68	13.82	12.15	11.44	14.25
Total	**95.43**	**97.04**	**99.65**	**91.99**	**94.31**
Al	0.09	0.11	0.10	0.07	0.18
Si	0.00	0.00	0.00	0.00	0.00
Mg	0.06	0.07	0.02	0.06	0.10
Fe2+	1.24	1.31	1.31	1.27	1.31
Fe3+	1.25	1.12	1.23	1.25	1.01
Mn	0.01	0.05	0.01	0.01	0.01
V	0.03	0.02	0.03	0.03	0.03
Cr	0.04	0.00	0.00	0.01	0.01
Ti	0.30	0.38	0.33	0.34	0.40
Total	**3.02**	**3.07**	**3.03**	**3.03**	**3.03**

148	148	148	148	148	148
BS1_mag7	BS1_mag8	BS1_mag10	BS1_mag11	BS1_mag12	BS1_mag13
3.59	2.28	2.32	3.67	3.26	3.31
0.04	0.03	0.05	0.04	0.05	0.05
1.79	0.93	1.22	0.88	1.39	1.49
73.35	76.56	82.23	75.02	71.42	79.37
0.31	0.35	0.27	0.48	0.33	0.02
0.94	0.80	0.58	1.11	1.11	0.94
0.00	0.05	0.90	0.24	0.22	0.73
14.23	12.39	10.91	13.87	13.68	15.43
94.26	**93.37**	**98.48**	**95.31**	**91.45**	**101.34**
0.16	0.10	0.10	0.16	0.15	0.14
0.00	0.00	0.00	0.00	0.00	0.00
0.10	0.05	0.07	0.05	0.08	0.08
1.29	1.30	1.23	1.33	1.31	1.33
1.03	1.17	1.28	1.04	1.03	1.02
0.01	0.01	0.01	0.02	0.01	0.00
0.03	0.03	0.02	0.04	0.04	0.03
0.00	0.00	0.03	0.01	0.01	0.02
0.41	0.36	0.30	0.39	0.40	0.41
3.03	**3.03**	**3.02**	**3.04**	**3.04**	**3.02**

Ti-magnetite mineral compositional data continued

Depth(m)	148	148	148	148	148
Sample	BS1_mag14	BS1_mag15	BS1_mag16	BS1_mag17	BS1_mag18
Al_2O_3	2.64	3.62	2.03	1.87	4.34
SiO_2	0.06	0.04	0.02	0.08	0.06
MgO	0.97	1.40	1.02	0.79	2.33
FeO	76.66	75.36	76.69	77.80	68.62
MnO	0.39	0.18	0.11	0.34	0.47
V_2O_3	1.09	0.98	0.72	0.81	0.90
Cr_2O_3	1.50	0.37	0.96	0.65	0.67
TiO_2	12.27	10.93	8.67	11.21	15.97
Total	**95.58**	**92.89**	**90.21**	**93.54**	**93.34**
Al	0.12	0.16	0.10	0.09	0.19
Si	0.00	0.00	0.00	0.00	0.00
Mg	0.06	0.08	0.06	0.05	0.13
Fe2+	1.28	1.23	1.20	1.27	1.31
Fe3+	1.14	1.19	1.36	1.24	0.87
Mn	0.01	0.01	0.00	0.01	0.02
V	0.03	0.03	0.03	0.03	0.03
Cr	0.05	0.01	0.03	0.02	0.02
Ti	0.35	0.32	0.26	0.33	0.33
Total	**3.03**	**3.03**	**3.03**	**3.03**	**2.90**

148	148	148	148	148
BS1_mag19	BS1_mag20	BS1_mag21	BS1_mag22	BS1_mag24
3.51	3.47	3.36	3.00	3.54
0.04	0.04	0.06	0.05	0.05
1.82	1.69	1.20	1.83	2.06
76.63	74.31	76.97	74.10	68.23
0.32	0.22	0.10	0.44	0.49
0.79	0.97	0.80	1.03	0.88
1.18	0.00	0.82	0.00	0.81
12.88	14.00	10.15	13.27	14.90
97.17	**94.70**	**93.47**	**93.72**	**90.96**
0.15	0.15	0.15	0.14	0.16
0.00	0.00	0.00	0.00	0.00
0.10	0.10	0.07	0.10	0.12
1.25	1.30	1.22	1.26	1.30
1.10	1.05	1.24	1.10	0.93
0.00	0.01	0.00	0.01	0.02
0.02	0.03	0.03	0.03	0.03
0.03	0.00	0.03	0.00	0.03
0.36	0.40	0.29	0.38	0.44
3.01	**3.03**	**3.02**	**3.03**	**3.03**

Ti-magnetite mineral compositional data continued

Depth(m)	148	148	148	148	148
Sample	BS1_mag25	BS1_mag26	BS1_mag27	BS1_mag28	BS1_mag29
Al_2O_3	3.47	3.94	3.46	3.51	3.48
SiO_2	0.03	0.00	0.02	0.06	0.04
MgO	1.94	1.81	0.70	1.96	1.74
FeO	72.47	73.36	73.85	73.13	75.53
MnO	0.15	0.21	0.26	0.26	0.29
V_2O_3	1.00	0.84	1.11	0.85	1.11
Cr_2O_3	0.20	0.00	0.66	0.00	0.45
TiO_2	13.64	15.94	13.51	15.06	13.48
Total	**92.91**	**96.10**	**93.56**	**94.82**	**96.11**
Al	0.16	0.17	0.16	0.16	0.15
Si	0.00	0.00	0.00	0.00	0.00
Mg	0.11	0.10	0.04	0.11	0.10
Fe2+	1.28	1.34	1.34	1.31	1.27
Fe3+	1.05	0.94	1.04	0.99	1.08
Mn	0.01	0.01	0.01	0.01	0.01
V	0.03	0.03	0.04	0.027	0.04
Cr	0.01	0.00	0.02	0.00	0.01
Ti	0.39	0.45	0.39	0.42	0.38
Total	**3.03**	**3.03**	**3.04**	**3.02**	**3.04**

148	148	148	148	148
BS1_mag30	BS1_mag31	BS1_mag32	BS1_mag33	BS1_mag34
3.89	2.88	3.20	3.63	4.15
0.06	0.05	0.04	0.07	0.03
2.00	1.32	1.75	1.87	2.37
69.45	79.30	74.41	68.24	68.35
0.27	0.22	0.46	0.32	0.43
1.35	1.17	0.91	0.97	1.22
0.02	0.93	0.00	0.46	1.18
17.06	12.03	14.01	14.56	19.06
94.09	**97.88**	**94.77**	**90.12**	**96.78**
0.18	0.13	0.14	0.17	0.18
0.00	0.00	0.00	0.00	0.00
0.11	0.07	0.10	0.11	0.13
1.37	1.26	1.29	1.32	1.39
0.84	1.18	1.06	0.94	0.72
0.01	0.01	0.02	0.01	0.01
0.04	0.04	0.03	0.03	0.04
0.00	0.03	0.00	0.01	0.03
0.49	0.33	0.40	0.43	0.52
3.04	**3.03**	**3.03**	**3.03**	**3.03**

Ti-magnetite mineral compositional data continued

Depth(m)	147.8	147.8	147.8	147.8	147.8
Sample	BS2_mag1	BS2_mag2	BS2_mag3	BS2_mag4	BS2_mag5
Al_2O_3	3.78	3.83	3.71	3.66	3.86
SiO_2	0.07	0.04	0.04	0.04	0.05
MgO	1.88	1.80	1.73	1.32	1.75
FeO	71.43	77.03	73.45	72.88	72.15
MnO	0.25	0.19	0.44	0.55	0.20
V_2O_3	0.97	1.28	0.93	1.12	1.06
Cr_2O_3	0.07	0.91	1.14	0.21	0.00
TiO_2	14.32	14.23	14.34	14.25	14.16
Total	**92.75**	**99.31**	**95.78**	**94.03**	**93.22**
Al	0.17	0.16	0.16	0.17	0.17
Si	0.00	0.00	0.00	0.00	0.00
Mg	0.11	0.10	0.10	0.08	0.10
Fe2+	1.30	1.29	1.29	1.32	1.30
Fe3+	0.99	1.04	1.00	1.01	1.01
Mn	0.01	0.01	0.01	0.02	0.01
V	0.03	0.04	0.03	0.04	0.03
Cr	0.00	0.03	0.03	0.01	0.00
Ti	0.41	0.39	0.40	0.41	0.41
Total	**3.03**	**3.04**	**3.03**	**3.04**	**3.03**

147.8	147.8	147.8	147.8	147.8
BS2_mag6	BS2_mag7	BS2_mag8	BS2_mag9	BS2_mag10
3.78	4.25	3.70	4.06	3.62
0.04	0.05	0.07	0.04	0.05
2.01	1.86	1.74	2.02	1.52
74.32	76.25	74.21	73.22	78.90
0.09	0.22	0.34	0.12	0.36
1.24	1.24	1.25	1.25	1.07
1.11	0.27	0.00	1.59	0.49
14.72	13.15	14.06	16.89	13.51
97.31	**97.27**	**95.37**	**99.20**	**99.52**
0.16	0.18	0.16	0.17	0.15
0.00	0.00	0.00	0.00	0.00
0.11	0.10	0.01	0.11	0.08
1.30	1.26	1.29	1.35	1.28
0.99	1.08	1.04	0.86	1.10
0.00	0.01	0.01	0.00	0.00
0.04	0.04	0.04	0.04	0.03
0.03	0.01	0.00	0.05	0.01
0.41	0.36	0.40	0.46	0.37
3.04	**3.04**	**2.95**	**3.04**	**3.02**

Ti-magnetite mineral compositional data continued

Depth(m)	147.8	147.8	147.8	147.8	147.8
Sample	BS2_mag11	BS2_mag12	BS2_mag13	BS2_mag14	BS2_mag15
Al_2O_3	3.82	3.58	3.41	3.92	3.84
SiO_2	0.02	0.08	0.04	0.05	0.04
MgO	1.95	1.49	1.28	1.79	1.88
FeO	76.86	75.25	78.06	75.77	74.10
MnO	0.40	0.31	0.37	0.51	0.50
V_2O_3	1.40	1.09	1.14	1.16	1.22
Cr_2O_3	0.53	0.65	0.21	0.65	1.66
TiO_2	14.41	12.82	13.29	14.60	14.37
Total	**99.39**	**95.26**	**97.80**	**98.43**	**97.61**
Al	0.16	0.16	0.15	0.17	0.17
Si	0.00	0.00	0.00	0.00	0.00
Mg	0.11	0.11	0.07	0.10	0.10
Fe2+	1.25	1.27	1.29	1.29	1.28
Fe3+	1.04	1.09	1.11	1.01	0.99
Mn	0.01	0.01	0.01	0.02	0.02
V	0.04	0.03	0.04	0.04	0.04
Cr	0.02	0.02	0.01	0.02	0.05
Ti	0.39	0.36	0.37	0.40	0.40
Total	**3.02**	**3.06**	**3.04**	**3.04**	**3.04**

147.8	147.8	147.8	147.8	147.8
BS2_mag16	BS2_mag17	BS2_mag18	BS2_mag20	BS2_mag21
3.69	3.11	4.01	5.40	3.92
0.04	0.04	0.09	0.05	0.04
1.54	1.85	1.97	2.34	1.66
73.10	76.76	75.91	77.29	77.47
0.35	0.21	0.35	0.16	0.18
1.19	0.87	0.53	1.39	1.12
0.79	0.13	0.46	0.00	0.00
15.15	13.95	14.17	15.17	13.22
95.85	**96.91**	**97.48**	**101.80**	**97.61**
0.16	0.14	0.17	0.22	0.17
0.00	0.00	0.00	0.00	0.00
0.09	0.10	0.11	0.12	0.09
1.33	1.28	1.27	1.27	1.27
0.96	1.09	1.03	0.98	1.10
0.01	0.01	0.01	0.01	0.01
0.04	0.03	0.02	0.04	0.03
0.02	0.00	0.01	0.00	0.00
0.43	0.39	0.39	0.40	0.36
3.04	**3.03**	**3.02**	**3.04**	**3.03**

Ti-magnetite mineral compositional data continued

Depth(m)	147.8	147.8	147.8	147.8	147.8
Sample	BS2_mag22	BS2_mag23	BS2_mag24	BS2_mag25	BS2_mag26
Al_2O_3	3.93	3.36	3.58	3.36	4.80
SiO_2	0.04	0.05	0.04	0.06	0.03
MgO	2.05	1.68	1.16	1.66	1.85
FeO	75.87	75.39	76.15	77.07	75.26
MnO	0.36	0.11	0.23	0.26	0.21
V_2O_3	1.25	0.91	1.20	1.22	1.15
Cr_2O_3	0.06	0.27	0.42	0.00	0.37
TiO_2	13.98	12.98	12.35	11.52	15.44
Total	**97.54**	**94.74**	**95.13**	**95.13**	**99.12**
Al	0.17	0.15	0.16	0.15	0.20
Si	0.00	0.00	0.00	0.00	0.00
Mg	0.11	0.09	0.07	0.09	0.10
Fe2+	1.26	1.27	1.28	1.23	1.31
Fe3+	1.06	1.10	1.12	1.20	0.95
Mn	0.01	0.00	0.01	0.01	0.01
V	0.04	0.03	0.04	0.04	0.04
Cr	0.00	0.01	0.01	0.00	0.01
Ti	0.38	0.37	0.35	0.33	0.42
Total	**3.04**	**3.03**	**3.04**	**3.04**	**3.03**

147.8	147.8	147.8	147.8	147.8
BS2_mag29	BS2_mag30	BS2_mag31	BS2_mag32	BS2_mag33
3.48	3.66	3.68	3.71	3.59
0.05	0.03	0.07	0.06	0.05
1.39	1.52	1.46	1.67	1.66
76.32	69.69	72.97	75.34	73.62
0.28	0.22	0.30	0.16	0.11
1.11	0.95	1.31	1.32	1.37
0.27	0.53	0.52	0.00	1.17
13.52	16.54	13.86	14.12	13.43
96.41	**93.15**	**94.16**	**96.38**	**95.00**
0.15	0.17	0.17	0.16	0.16
0.00	0.00	0.00	0.00	0.00
0.08	0.09	0.08	0.09	0.09
1.29	1.39	1.31	1.30	1.29
1.08	0.86	1.02	1.04	1.04
0.01	0.01	0.01	0.01	0.00
0.04	0.03	0.04	0.04	0.04
0.01	0.02	0.02	0.00	0.04
0.38	0.48	0.40	0.40	0.38
3.03	**3.03**	**3.04**	**3.04**	**3.04**

Ti-magnetite mineral compositional data continued

Depth(m)	147.8	147.4	147.4	147.4
Sample	BS2_mag34	BS4_mag1	BS4_mag2	BS4_mag3
Al_2O_3	3.74	3.93	1.64	4.00
SiO_2	0.01	0.05	0.08	0.05
MgO	1.12	1.64	0.72	1.71
FeO	73.69	73.26	73.69	76.98
MnO	0.22	0.05	0.39	0.37
V_2O_3	0.98	0.82	0.71	0.40
Cr_2O_3	0.55	0.24	0.96	0.34
TiO_2	13.82	14.48	15.13	14.81
Total	**94.13**	**94.60**	**92.74**	**99.09**
Al	0.17	0.17	0.08	0.17
Si	0.00	0.00	0.00	0.00
Mg	0.06	0.09	0.04	0.09
Fe2+	1.33	1.34	1.39	1.30
Fe3+	1.02	0.96	1.01	1.02
Mn	0.01	0.00	0.01	0.01
V	0.03	0.03	0.02	0.01
Cr	0.02	0.01	0.03	0.01
Ti	0.40	0.43	0.44	0.40
Total	**3.03**	**3.03**	**3.02**	**3.01**

147.4 BS4_mag4	147.4 BS4_mag5	147.4 BS4_mag6	147.4 BS4_mag7	147.4 BS4_mag8	147.4 BS4_mag9
4.19	3.72	3.81	4.28	4.00	3.09
0.04	0.03	0.04	0.05	0.06	0.05
1.20	2.05	1.84	1.91	1.39	1.61
72.72	71.46	75.36	77.35	71.92	74.06
0.10	0.18	0.17	0.47	0.28	0.45
1.15	0.98	1.01	0.63	0.97	0.69
0.00	0.00	0.47	0.05	0.60	0.00
13.69	16.52	16.51	9.79	15.06	14.71
93.11	**94.94**	**99.20**	**94.52**	**94.28**	**94.65**
0.19	0.17	0.16	0.19	0.18	0.14
0.00	0.00	0.00	0.00	0.00	0.00
0.07	0.12	0.10	0.11	0.08	0.09
1.33	1.35	1.35	1.16	1.35	1.31
1.02	0.90	0.93	1.26	0.94	1.02
0.00	0.01	0.01	0.02	0.01	0.01
0.04	0.03	0.03	0.02	0.03	0.02
0.00	0.00	0.01	0.00	0.02	0.00
0.40	0.47	0.45	0.28	0.43	0.42
3.04	**3.03**	**3.03**	**3.02**	**3.03**	**3.02**

Ti-magnetite mineral compositional data continued

Depth(m)	147.4	147.4	147.4	147.4	147.4
Sample	BS4_mag10	BS4_mag11	BS4_mag12	BS4_mag13	BS4_mag14
Al_2O_3	3.85	3.47	3.92	2.77	3.58
SiO_2	0.08	0.10	0.06	0.05	0.03
MgO	1.25	1.49	1.19	1.19	1.66
FeO	76.15	75.95	75.49	72.75	74.58
MnO	0.23	0.19	0.46	0.22	0.30
V_2O_3	1.20	1.11	0.95	1.19	1.09
Cr_2O_3	0.16	0.28	0.00	0.00	0.19
TiO_2	14.23	14.50	13.80	16.66	14.60
Total	**97.15**	**97.07**	**95.88**	**94.82**	**96.02**
Al	0.17	0.15	0.17	0.13	0.16
Si	0.00	0.00	0.00	0.00	0.00
Mg	0.07	0.08	0.07	0.07	0.09
Fe2+	1.32	1.32	1.31	1.41	1.31
Fe3+	1.03	1.03	1.05	0.92	1.02
Mn	0.01	0.01	0.02	0.01	0.01
V	0.04	0.03	0.03	0.04	0.03
Cr	0.01	0.01	0.00	0.00	0.01
Ti	0.40	0.40	0.39	0.48	0.41
Total	**3.03**	**3.03**	**3.03**	**3.04**	**3.03**

147.4	147.4	147.4	147.4	147.4
BS4_mag15	BS4_mag16	BS4_mag17	BS4_mag18	BS4_mag19
3.88	3.59	3.65	3.82	3.25
0.04	0.03	0.05	0.06	0.05
1.19	1.75	1.44	1.52	2.02
76.14	75.35	74.52	76.91	74.27
0.32	0.05	0.24	0.28	0.30
1.17	0.78	0.79	1.27	0.51
0.00	0.51	0.10	0.33	0.40
14.98	12.01	13.09	14.00	14.17
97.71	**94.08**	**93.87**	**98.20**	**94.97**
0.17	0.16	0.16	0.16	0.14
0.00	0.00	0.00	0.00	0.00
0.07	0.10	0.08	0.08	0.11
1.34	1.24	1.29	1.30	1.28
1.00	1.14	1.08	1.05	1.04
0.01	0.00	0.01	0.01	0.01
0.04	0.03	0.03	0.04	0.02
0.00	0.02	0.00	0.01	0.01
0.41	0.34	0.37	0.38	0.40
3.03	**3.02**	**3.02**	**3.03**	**3.01**

Ti-magnetite mineral compositional data continued

Depth(m)	147.4	147.4	147.4	147.4	147.4
Sample	BS4_mag20	BS4_mag21	BS4_mag22	BS4_mag23	BS4_mag24
Al_2O_3	3.47	3.87	3.39	3.35	3.54
SiO_2	0.07	0.04	0.11	0.04	0.05
MgO	1.79	1.66	1.02	1.64	1.78
FeO	77.14	75.22	75.77	77.33	72.91
MnO	0.16	0.30	0.38	0.12	0.41
V_2O_3	0.83	0.99	0.93	1.07	0.91
Cr_2O_3	0.32	0.03	0.39	0.00	0.01
TiO_2	12.09	14.03	13.66	13.79	14.94
Total	**95.88**	**96.16**	**95.65**	**97.33**	**94.54**
Al	0.16	0.14	0.15	0.17	0.15
Si	0.00	0.00	0.00	0.00	0.00
Mg	0.08	0.11	0.10	0.09	0.06
Fe2+	1.30	1.28	1.24	1.29	1.32
Fe3+	1.05	1.04	1.16	1.04	1.06
Mn	0.01	0.01	0.01	0.01	0.01
V	0.04	0.02	0.03	0.03	0.03
Cr	0.01	0.01	0.01	0.00	0.01
Ti	0.38	0.40	0.34	0.39	0.39
Total	**3.04**	**3.01**	**3.02**	**3.03**	**3.03**

147.4	147.4	147.4	147.4	147.4
BS4_mag25	BS4_mag26	BS4_mag27	BS4_mag28	BS4_mag29
3.31	6.14	3.60	4.04	3.68
0.02	0.08	0.01	0.05	0.06
0.99	2.83	1.44	1.86	1.35
75.22	64.74	74.39	72.32	74.71
0.23	0.29	0.39	0.16	0.41
1.00	0.85	0.82	1.02	1.06
0.00	0.43	0.01	0.08	0.29
13.51	15.25	14.81	15.36	14.50
94.29	**90.61**	**95.47**	**94.89**	**96.04**
0.15	0.28	0.16	0.18	0.16
0.00	0.00	0.00	0.00	0.00
0.09	0.16	0.08	0.10	0.08
1.29	1.27	1.33	1.33	1.32
1.09	0.82	1.01	0.95	1.01
0.00	0.01	0.01	0.01	0.01
0.03	0.03	0.03	0.03	0.03
0.00	0.01	0.00	0.00	0.01
0.38	0.44	0.42	0.43	0.41
3.03	**3.02**	**3.03**	**3.03**	**3.03**

Ti-magnetite mineral compositional data continued

Depth(m)	147.4	147.4	147.4	147.4	147.2
Sample	BS4_mag30	BS4_mag31	BS4_mag32	BS4_mag33	BS5_mag1
Al_2O_3	3.62	3.46	1.22	1.97	4.75
SiO_2	0.03	0.03	0.06	0.04	0.04
MgO	1.65	1.01	0.27	1.82	1.24
FeO	71.57	74.98	77.94	80.48	74.89
MnO	0.29	0.14	0.32	0.27	0.22
V_2O_3	0.90	0.94	1.19	1.03	1.07
Cr_2O_3	0.00	0.15	0.00	0.51	0.16
TiO_2	14.11	14.38	14.27	12.14	14.48
Total	**92.17**	**95.08**	**95.26**	**98.25**	**96.85**
Al	0.17	0.15	0.06	0.09	0.21
Si	0.00	0.00	0.00	0.00	0.00
Mg	0.10	0.06	0.02	0.10	0.07
Fe2+	1.31	1.35	1.39	1.23	1.33
Fe3+	1.01	1.02	1.12	1.23	0.98
Mn	0.01	0.00	0.01	0.01	0.01
V	0.03	0.03	0.04	0.03	0.03
Cr	0.00	0.00	0.00	0.02	0.01
Ti	0.41	0.41	0.41	0.33	0.40
Total	**3.03**	**3.03**	**3.04**	**3.03**	**3.03**

147.2	147.2	147.2	147.2	147.2
BS5_mag2	BS5_mag3	BS5_mag4	BS5_mag5	BS5_mag6
4.27	4.39	7.36	5.04	4.74
0.04	0.01	0.02	0.05	0.06
0.81	0.30	0.85	0.84	0.92
74.84	76.05	72.86	76.91	78.58
0.49	0.21	0.40	0.05	0.21
0.94	1.15	1.82	1.24	1.14
0.51	0.00	0.47	0.00	0.08
12.63	12.37	14.96	11.72	14.41
94.53	**94.48**	**98.73**	**95.84**	**100.13**
0.19	0.20	0.31	0.22	0.20
0.00	0.00	0.00	0.00	0.00
0.05	0.02	0.05	0.05	0.05
1.30	1.33	1.35	1.28	1.34
1.07	1.09	0.86	1.12	1.02
0.02	0.01	0.01	0.00	0.01
0.03	0.04	0.06	0.04	0.03
0.02	0.00	0.01	0.00	0.00
0.36	0.36	0.41	0.33	0.39
3.03	**3.04**	**3.05**	**3.04**	**3.03**

Ti-magnetite mineral compositional data continued

Depth (m)	147.2	147.2	147.2	147.2	147.2
Sample	BS5_mag7	BS5_mag8	BS5_mag9	BS5_mag10	BS5_mag11
Al_2O_3	4.38	5.32	5.54	7.78	3.49
SiO_2	0.03	0.05	0.06	0.04	0.05
MgO	0.25	1.40	1.27	1.13	0.45
FeO	79.92	72.45	71.61	71.85	77.13
MnO	0.32	0.26	0.17	0.26	0.33
V_2O_3	1.35	0.88	1.17	0.94	1.34
Cr_2O_3	0.00	0.68	0.00	0.00	0.21
TiO_2	11.88	16.15	16.71	13.52	11.64
Total	**98.12**	**97.19**	**96.53**	**95.50**	**94.63**
Al	0.19	0.23	0.24	0.34	0.16
Si	0.00	0.00	0.00	0.00	0.00
Mg	0.01	0.08	0.07	0.06	0.03
Fe2+	1.31	1.36	1.39	1.31	1.30
Fe3+	1.15	0.86	0.82	0.91	1.16
Mn	0.01	0.01	0.01	0.01	0.01
V	0.04	0.03	0.04	0.03	0.04
Cr	0.00	0.02	0.00	0.00	0.01
Ti	0.33	0.45	0.47	0.38	0.33
Total	**3.04**	**3.03**	**3.03**	**3.03**	**3.04**

147.2	147.2	147.2	147.2	147.2
BS5_mag12	BS5_mag13	BS5_mag14	BS5_mag15	BS5_mag16
6.16	4.85	4.01	4.35	4.29
0.08	0.06	0.05	0.06	0.03
1.00	0.91	0.86	1.11	0.62
71.23	72.12	75.36	74.56	74.33
0.39	0.28	0.20	0.35	0.28
1.62	1.78	1.18	1.13	1.48
0.92	0.15	0.00	0.26	0.15
16.43	12.92	12.44	13.24	12.77
97.83	**93.06**	**94.10**	**95.04**	**93.95**
0.27	0.22	0.18	0.19	0.19
0.00	0.00	0.00	0.00	0.00
0.06	0.05	0.05	0.06	0.04
1.39	1.32	1.30	1.30	1.33
0.80	1.02	1.10	1.05	1.06
0.01	0.01	0.01	0.01	0.01
0.05	0.06	0.04	0.04	0.05
0.03	0.01	0.00	0.01	0.01
0.45	0.38	0.36	0.38	0.37
3.05	**3.06**	**3.04**	**3.03**	**3.05**

Ti-magnetite mineral compositional data continued

Depth(m)	147.2	147.2	147.2	145	145
Sample	BS5_mag19	BS5_mag20	BS5_mag21	OBSZ6_mag11	OBSZ6_mag16
Al_2O_3	3.62	5.58	4.49	0.75	2.94
SiO_2	0.23	0.05	0.06	0.18	4.00
MgO	0.59	1.43	0.39	0.04	0.50
FeO	82.19	74.01	77.64	86.06	72.54
MnO	0.30	0.24	0.44	0.29	0.30
V_2O_3	1.10	1.58	0.96	0.43	0.92
Cr_2O_3	0.46	0.00	0.62	0.40	0.00
TiO_2	11.05	13.81	12.98	11.58	13.97
Total	**99.53**	**96.69**	**97.58**	**99.72**	**95.16**
Al	0.15	0.24	0.20	0.03	0.13
Si	0.01	0.00	0.00	0.00	0.15
Mg	0.03	0.08	0.02	0.00	0.03
Fe2+	1.27	1.30	1.33	1.31	1.51
Fe3+	1.22	0.99	1.06	1.32	0.78
Mn	0.01	0.01	0.01	0.01	0.01
V	0.03	0.05	0.03	0.01	0.03
Cr	0.01	0.00	0.02	0.01	0.00
Ti	0.30	0.38	0.36	0.32	0.40
Total	**3.03**	**3.05**	**3.03**	**3.01**	**3.03**

145	134.5	118.2	118.2	118.2
OBSZ6_mag17	OBSZ6_mag20	OHSZ5_mag1	OHSZ5_mag2	OHSZ5_mag3
2.47	2.74	4.09	3.05	2.96
3.17	4.20	0.05	0.06	0.08
0.27	0.45	0.02	0.17	0.07
74.51	73.40	73.39	79.21	77.60
0.18	0.30	0.44	0.19	0.22
0.35	0.41	1.15	0.99	1.10
0.00	0.00	0.00	0.00	0.27
17.36	15.07	17.02	14.25	13.24
98.30	**96.56**	**96.17**	**97.90**	**95.55**
0.11	0.12	0.18	0.13	0.13
0.12	0.16	0.00	0.00	0.00
0.02	0.03	0.00	0.01	0.00
1.57	1.54	1.47	1.38	1.37
0.71	0.73	0.85	1.07	1.10
0.01	0.01	0.01	0.01	0.01
0.01	0.01	0.04	0.03	0.04
0.00	0.00	0.00	0.00	0.01
0.48	0.42	0.48	0.40	0.38
3.01	**3.01**	**3.04**	**3.03**	**3.03**

Ti-magnetite mineral compositional data continued

Depth (m)	118.2	118.2	118.2	118.2	118.2
Sample	OHSZ5_mag4	OHSZ5_mag5	OHSZ5_mag6	OHSZ5_mag7	OHSZ5_mag8
Al_2O_3	2.92	3.25	2.31	2.53	1.95
SiO_2	0.30	0.04	0.03	0.03	0.06
MgO	0.14	0.01	0.03	0.05	0.00
FeO	76.29	82.26	80.27	80.09	76.86
MnO	0.24	0.15	0.23	0.25	0.41
V_2O_3	1.10	1.08	1.10	0.75	1.30
Cr_2O_3	0.00	0.70	0.00	0.19	0.00
TiO_2	13.12	10.21	13.32	11.97	13.84
Total	**94.10**	**97.70**	**97.28**	**95.85**	**94.42**
Al	0.13	0.14	0.10	0.11	0.09
Si	0.01	0.00	0.00	0.00	0.00
Mg	0.01	0.00	0.00	0.00	0.00
Fe2+	1.38	1.28	1.37	1.33	1.39
Fe3+	1.08	1.27	1.15	1.20	1.10
Mn	0.01	0.01	0.01	0.01	0.01
V	0.04	0.03	0.03	0.02	0.04
Cr	0.00	0.02	0.00	0.01	0.00
Ti	0.38	0.28	0.38	0.34	0.40
Total	**3.04**	**3.03**	**3.03**	**3.02**	**3.04**

118.2	118.2	118.2	118.2	118.2
OHSZ5_mag9	OHSZ5_mag10	OHSZ5_mag11	OHSZ5_mag12	OHSZ5_mag14
1.36	1.68	1.92	2.95	3.42
0.03	0.08	0.05	0.05	0.05
0.00	0.00	0.11	0.06	0.25
85.87	83.03	83.16	82.42	77.74
0.44	0.22	0.21	0.33	0.32
1.03	1.10	0.75	1.06	0.87
0.00	0.57	0.14	0.40	0.53
9.74	12.56	12.34	11.50	14.20
98.48	**99.24**	**98.68**	**98.76**	**97.39**
0.06	0.07	0.08	0.13	0.15
0.00	0.00	0.00	0.00	0.00
0.00	0.00	0.01	0.00	0.01
1.26	1.34	1.33	1.31	1.37
1.40	1.21	1.23	1.22	1.04
0.01	0.01	0.01	0.01	0.01
0.03	0.03	0.02	0.03	0.03
0.00	0.02	0.00	0.01	0.02
0.27	0.35	0.34	0.32	0.40
3.03	**3.03**	**3.02**	**3.03**	**3.03**

Ti-magnetite mineral compositional data continued

Depth(m)	118.2	118.2	118.2	118.2	118.2	118.2	63.1	63.1	63.1
Sample	OHSZ5_mag15	OHSZ5_mag16	OHSZ5_mag17	OHSZ5_mag18	OHSZ5_mag19	OHSZ5_mag20	WG4_mag1	WG4_mag2	WG4_mag3
Al_2O_3	3.59	7.06	4.69	3.89	6.48	5.29	1.88	2.68	3.37
SiO_2	0.03	0.05	0.00	0.05	0.05	0.06	0.07	0.05	0.02
MgO	0.02	0.35	0.09	0.05	0.05	0.03	0.25	0.10	0.45
FeO	76.87	66.73	75.38	73.69	75.68	74.14	83.05	75.37	79.67
MnO	0.16	0.26	0.41	0.35	0.41	0.57	0.27	0.43	0.29
V_2O_3	0.93	1.10	1.17	1.02	1.40	1.18	1.16	1.26	1.27
Cr_2O_3	0.00	0.00	0.00	0.00	0.26	0.00	0.00	0.00	0.00
TiO_2	13.21	19.44	14.51	11.13	17.54	15.39	13.86	14.92	11.47
Total	**94.81**	**94.99**	**96.24**	**90.16**	**101.87**	**96.65**	**100.55**	**94.81**	**96.53**
Al	0.16	0.31	0.21	0.18	0.27	0.23	0.08	0.12	0.15
Si	0.00	0.00	0.00	0.00	0.00	0.00	0.00	0.00	0.00
Mg	0.00	0.02	0.01	0.00	0.00	0.00	0.01	0.01	0.03
Fe2+	1.37	1.53	1.39	1.32	1.45	1.41	1.36	1.41	1.29
Fe3+	1.08	0.58	0.97	1.14	0.79	0.90	1.16	1.01	1.20
Mn	0.01	0.01	0.01	0.01	0.01	0.02	0.01	0.01	0.01
V	0.03	0.04	0.04	0.03	0.04	0.04	0.04	0.04	0.04
Cr	0.00	0.00	0.00	0.00	0.01	0.00	0.00	0.00	0.00
Ti	0.38	0.55	0.41	0.34	0.47	0.43	0.38	0.43	0.32
Total	**3.03**	**3.04**	**3.04**	**3.03**	**3.04**	**3.04**	**3.04**	**3.04**	**3.04**

Ti-magnetite mineral compositional data continued

Depth(m)	63.1	63.1	63.1	63.1
Sample	WG4_mag4	WG4_mag5	WG4_mag6	WG4_mag11
Al_2O_3	2.91	6.85	2.48	2.78
SiO_2	0.05	0.05	0.03	0.03
MgO	0.33	0.17	0.21	0.29
FeO	75.02	74.72	78.83	80.51
MnO	0.35	0.28	0.48	0.29
V_2O_3	1.00	0.65	1.07	0.88
Cr_2O_3	0.10	0.00	0.49	0.21
TiO_2	13.47	14.19	15.80	9.87
Total	**93.22**	**96.90**	**99.39**	**94.85**
Al	0.13	0.30	0.11	0.13
Si	0.00	0.00	0.00	0.00
Mg	0.02	0.01	0.01	0.02
Fe2+	1.37	1.38	1.41	1.26
Fe3+	1.07	0.92	1.01	1.30
Mn	0.01	0.01	0.02	0.01
V	0.03	0.02	0.03	0.03
Cr	0.00	0.00	0.01	0.01
Ti	0.39	0.39	0.44	0.28
Total	**3.03**	**3.02**	**3.03**	**3.03**

63.1	63.1	63.1	63.1	63.1
WG4_mag13	WG4_mag14	WG4_mag15	WG4_mag17	WG4_mag18
2.74	3.05	3.39	3.49	2.02
0.05	0.07	0.06	0.04	0.04
0.53	0.31	0.55	0.25	0.27
77.81	80.68	75.73	81.43	84.79
0.27	0.19	0.08	0.24	0.27
0.97	1.25	1.18	1.33	1.14
0.00	0.00	0.00	0.78	0.47
13.02	9.68	10.98	9.53	10.25
95.37	**95.22**	**91.98**	**97.09**	**99.25**
0.12	0.14	0.16	0.15	0.09
0.00	0.00	0.00	0.00	0.00
0.03	0.02	0.03	0.01	0.02
1.33	1.26	1.29	1.25	1.26
1.13	1.31	1.19	1.29	1.33
0.01	0.01	0.00	0.01	0.01
0.03	0.04	0.04	0.04	0.04
0.00	0.00	0.00	0.02	0.01
0.37	0.28	0.32	0.27	0.28
3.03	**3.04**	**3.04**	**3.04**	**3.03**

Ti-magnetite mineral compositional data continued

Depth(m)	63.1	63.1	20.8	20.8
Sample	WG4_mag19	WG4_mag20	LS5_mag1	LS5_mag2
Al_2O_3	2.44	1.16	1.49	4.36
SiO_2	0.05	0.19	0.32	0.09
MgO	0.23	0.16	0.44	0.80
FeO	82.93	89.39	71.97	77.65
MnO	0.20	0.33	0.34	0.24
V_2O_3	0.82	0.99	1.31	1.03
Cr_2O_3	0.00	0.00	0.03	0.00
TiO_2	8.22	6.83	14.72	15.15
Total	**94.88**	**99.04**	**90.60**	**99.32**
Al	0.11	0.05	0.07	0.19
Si	0.00	0.01	0.01	0.00
Mg	0.01	0.01	0.03	0.04
Fe2+	1.22	1.18	1.42	1.37
Fe3+	1.42	1.56	1.01	0.98
Mn	0.01	0.01	0.01	0.01
V	0.03	0.03	0.04	0.03
Cr	0.00	0.00	0.00	0.00
Ti	0.24	0.19	0.45	0.41
Total	**3.03**	**3.03**	**3.04**	**3.03**

20.8	20.8	20.8	20.8	20.8	20.8
LS5_mag4	LS5_mag6	LS5_mag7	LS5_mag8	LS5_mag9	LS5_mag10
5.50	1.68	3.16	4.80	5.02	5.15
0.05	0.27	0.07	0.26	0.03	0.03
0.68	0.42	0.55	0.85	1.01	1.05
76.61	73.77	82.58	70.61	64.87	72.25
0.02	0.27	0.23	0.19	0.27	0.05
1.32	1.12	0.96	1.24	1.00	1.47
0.23	0.40	0.00	0.00	0.00	0.00
12.68	16.02	11.40	20.45	21.28	18.27
97.09	**93.94**	**98.96**	**98.40**	**93.47**	**98.26**
0.24	0.08	0.14	0.21	0.23	0.22
0.00	0.01	0.00	0.01	0.00	0.00
0.04	0.02	0.03	0.05	0.06	0.06
1.32	1.45	1.28	1.52	1.55	1.45
1.05	0.95	1.24	0.65	0.54	0.77
0.00	0.01	0.01	0.01	0.01	0.00
0.04	0.04	0.03	0.04	0.03	0.05
0.01	0.01	0.00	0.00	0.00	0.00
0.35	0.47	0.31	0.56	0.62	0.50
3.04	**3.04**	**3.03**	**3.04**	**3.03**	**3.04**

Ti-magnetite mineral compositional data continued

Depth(m)	20.8	20.8	20.8	20.8	20.8
Sample	LS5_mag11	LS5_mag12	LS5_mag13	LS5_mag14	LS5_mag16
Al_2O_3	4.25	4.14	5.55	4.05	5.52
SiO_2	0.05	0.05	0.02	0.03	0.06
MgO	0.89	0.90	0.93	1.06	0.81
FeO	77.17	70.37	72.35	72.24	66.19
MnO	0.08	0.37	0.20	0.44	0.47
V_2O_3	1.20	1.15	1.06	1.31	1.67
Cr_2O_3	0.00	0.07	1.01	0.00	0.49
TiO_2	15.39	15.91	20.55	16.36	22.07
Total	**99.03**	**92.96**	**101.67**	**95.49**	**97.26**
Al	0.18	0.19	0.23	0.18	0.24
Si	0.00	0.00	0.00	0.00	0.00
Mg	0.05	0.05	0.05	0.06	0.05
Fe2+	1.37	1.40	1.49	1.39	1.56
Fe3+	0.97	0.88	0.65	0.89	0.50
Mn	0.00	0.01	0.01	0.01	0.02
V	0.04	0.04	0.03	0.04	0.05
Cr	0.00	0.00	0.03	0.00	0.01
Ti	0.42	0.46	0.55	0.46	0.62
Total	**3.04**	**3.04**	**3.03**	**3.04**	**3.05**

20.8	20.8	20.8	20.8	20.8
LS5_mag17	LS5_mag18	LS5_mag19	LS5_mag20	LS5_mag21
3.23	4.70	3.78	5.36	3.93
0.08	0.05	0.28	0.06	0.10
0.76	1.80	0.64	1.39	0.83
75.64	65.21	72.10	64.77	71.55
0.13	0.17	0.37	0.34	0.19
1.09	1.22	1.21	1.56	1.07
0.03	0.00	0.00	0.00	0.00
14.09	20.44	12.61	21.08	17.65
95.04	**93.58**	**90.98**	**94.56**	**95.30**
0.15	0.21	0.18	0.24	0.18
0.00	0.00	0.01	0.00	0.00
0.04	0.10	0.04	0.08	0.05
1.36	1.48	1.34	1.52	1.45
1.04	0.61	1.05	0.55	0.81
0.00	0.01	0.01	0.01	0.01
0.04	0.04	0.04	0.05	0.03
0.00	0.00	0.00	0.00	0.00
0.40	0.59	0.38	0.60	0.50
3.04	**3.04**	**3.04**	**3.05**	**3.03**

Ti-magnetite mineral compositional data continued

Depth(m)	20.8	20.8	20.8	6
Sample	LS5_mag23	LS5_mag24	LS5_mag26	LS1_mag2
Al_2O_3	5.44	6.52	1.95	3.09
SiO_2	0.05	0.04	0.36	0.01
MgO	1.05	0.89	0.42	0.64
FeO	69.39	78.00	76.78	80.85
MnO	0.21	0.06	0.13	0.00
V_2O_3	1.42	1.47	1.21	1.16
Cr_2O_3	0.00	0.27	0.00	0.08
TiO_2	19.68	12.16	15.78	9.17
Total	**97.23**	**99.40**	**96.63**	**95.00**
Al	0.24	0.28	0.09	0.14
Si	0.00	0.00	0.01	0.00
Mg	0.06	0.05	0.02	0.04
Fe2+	1.49	1.28	1.43	1.23
Fe3+	0.66	1.06	0.99	1.34
Mn	0.01	0.00	0.00	0.00
V	0.04	0.04	0.04	0.04
Cr	0.00	0.01	0.00	0.00
Ti	0.55	0.33	0.45	0.26
Total	**3.04**	**3.04**	**3.04**	**3.04**

6	6	6	6	6	6
LS1_mag4	LS1_mag5	LS1_mag7	LS1_mag9	LS1_mag10	LS1_mag11
3.45	2.97	3.95	5.23	4.75	4.60
0.37	0.07	0.08	0.45	0.05	0.13
0.69	0.68	0.69	0.76	0.43	0.63
79.21	80.08	70.68	70.18	69.41	67.72
0.30	0.38	0.45	0.19	0.37	0.40
0.94	1.25	1.34	1.24	1.25	1.19
0.00	0.00	0.40	0.00	0.10	0.00
15.82	12.50	14.69	17.67	17.38	16.59
100.78	**97.93**	**92.28**	**95.72**	**93.74**	**91.25**
0.15	0.13	0.18	0.23	0.22	0.21
0.01	0.00	0.00	0.02	0.00	0.01
0.04	0.04	0.04	0.04	0.03	0.04
1.39	1.30	1.38	1.47	1.47	1.45
0.98	1.17	0.93	0.74	0.77	0.79
0.01	0.01	0.02	0.01	0.01	0.01
0.03	0.04	0.04	0.04	0.04	0.04
0.00	0.00	0.01	0.00	0.00	0.00
0.43	0.35	0.43	0.50	0.50	0.49
3.03	**3.04**	**3.04**	**3.04**	**3.04**	**3.04**

Ti-magnetite mineral compositional data continued

Depth(m)	6	6	6	6	6
Sample	LS1_mag12	LS1_mag13	LS1_mag14	LS1_mag15	LS1_mag16
Al_2O_3	5.14	3.79	4.70	3.66	4.01
SiO_2	0.04	0.21	0.06	0.03	0.08
MgO	1.29	1.08	0.98	1.03	0.94
FeO	71.11	69.02	76.72	77.41	69.62
MnO	0.32	0.38	0.33	0.44	0.43
V_2O_3	1.41	1.43	1.33	1.09	1.18
Cr_2O_3	0.00	0.26	0.00	0.67	0.16
TiO_2	17.95	15.80	16.25	13.42	14.06
Total	**97.27**	**91.98**	**100.37**	**97.75**	**90.47**
Al	0.22	0.18	0.20	0.16	0.19
Si	0.00	0.01	0.00	0.00	0.00
Mg	0.07	0.06	0.05	0.06	0.06
Fe2+	1.42	1.40	1.38	1.30	1.35
Fe3+	0.78	0.87	0.92	1.08	0.96
Mn	0.01	0.01	0.01	0.01	0.01
V	0.04	0.05	0.04	0.03	0.04
Cr	0.00	0.01	0.00	0.02	0.01
Ti	0.50	0.47	0.44	0.37	0.42
Total	**3.04**	**3.05**	**3.04**	**3.03**	**3.04**

6	6	6	6	6	6
LS1_mag17	LS1_mag18	LS1_mag19	LS1_mag20	LS1_mag21	LS1_mag22
5.08	4.79	5.00	5.27	4.16	4.86
0.70	0.02	0.13	0.66	0.06	0.59
0.86	1.11	0.80	1.37	0.46	0.95
71.39	74.59	64.65	65.25	73.38	69.50
0.03	0.33	0.16	0.37	0.31	0.40
1.63	1.24	1.59	1.30	1.21	1.48
0.00	0.02	0.00	0.00	0.00	0.29
20.48	17.89	18.58	18.48	15.67	17.18
100.17	**99.99**	**90.91**	**92.69**	**95.25**	**95.24**
0.22	0.20	0.23	0.24	0.19	0.22
0.03	0.00	0.01	0.03	0.00	0.02
0.05	0.06	0.05	0.08	0.03	0.05
1.53	1.42	1.51	1.47	1.41	1.44
0.62	0.83	0.64	0.64	0.92	0.75
0.00	0.01	0.01	0.01	0.01	0.01
0.05	0.04	0.05	0.04	0.04	0.05
0.00	0.00	0.00	0.00	0.00	0.01
0.56	0.48	0.56	0.54	0.45	0.49
3.05	**3.04**	**3.05**	**3.04**	**3.04**	**3.05**

Appendix D: Comparisons of trace element concentrations analysed using XRF versus ICP-MS

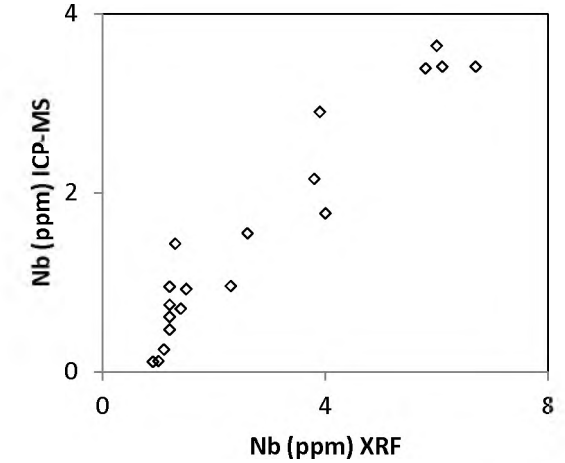

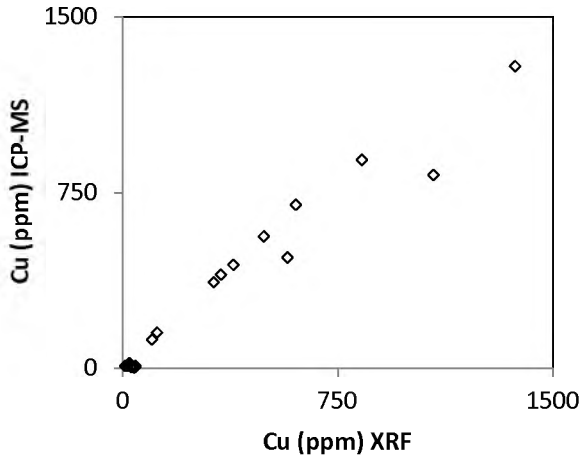

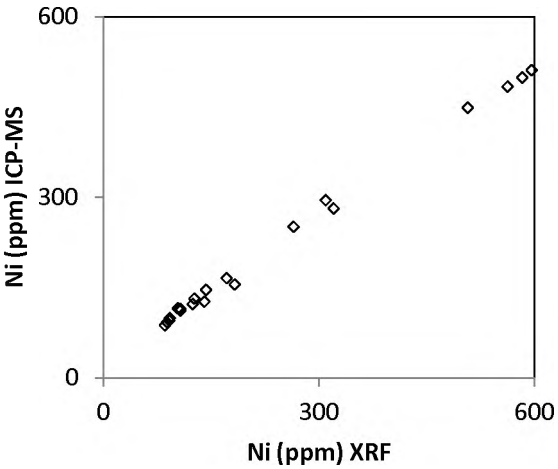

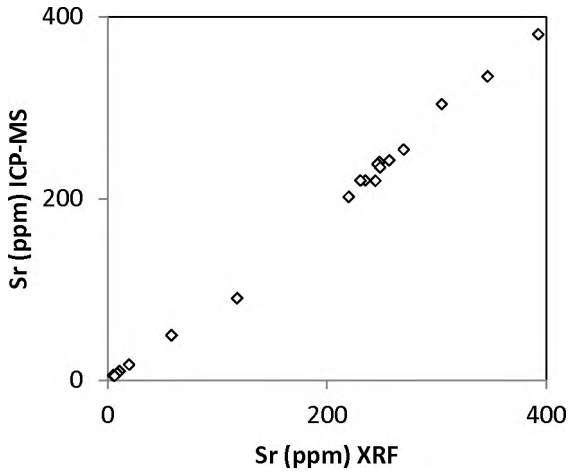

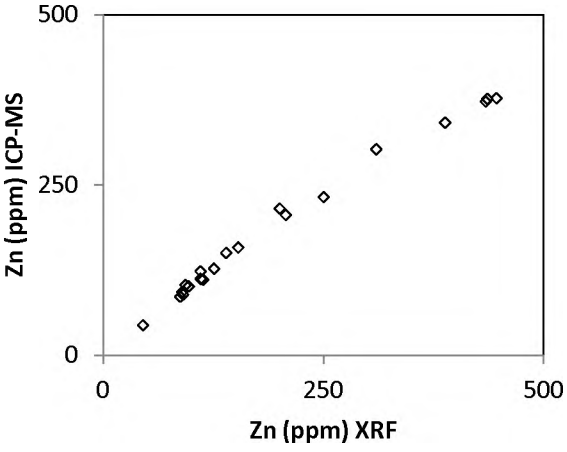

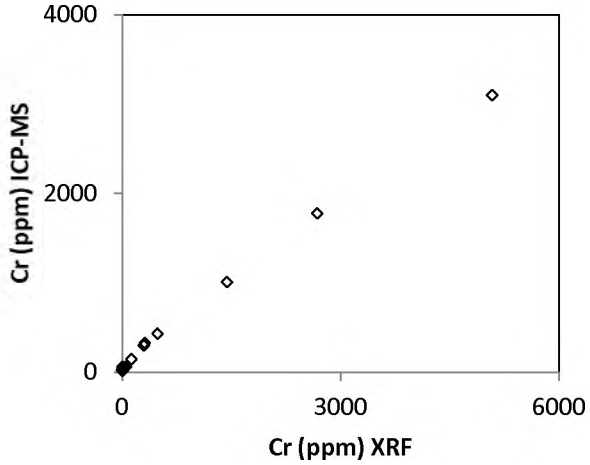

Comparisons of trace element concentrations analysed using XRF versus ICP-MS continued

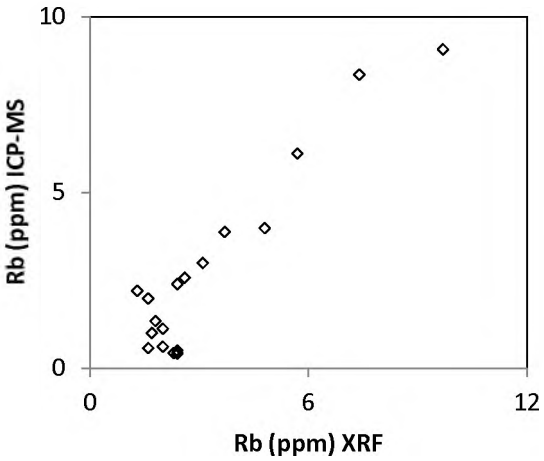

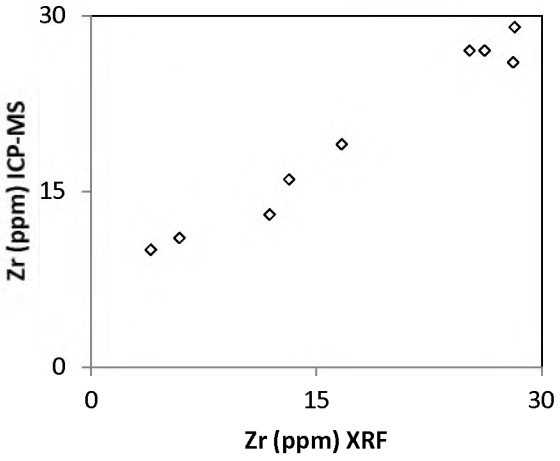

Appendix E: Google Earth image showing the location of Rhovan vanadium mine with specific landmarks for reference

Appendix F: List of abbreviations

Plag – Altered Plagioclase

Mag – Magnetite

Cpx – Clinopyroxene

Alt cpx – Altered Clinopyroxene

Opx – Orthopyroxene

Ilm – Ilmenite

Bt – Biotite

Chl – Chlorite

Ol – Olivine

Hem. margin – Hematised Margin

Ulv. Exs. – Ulvöspinel Exsolution

Exs. Lam. – Exsolution Lamellae

Symp – Symplectite

Py – Pyrite

Cpy – Chalcopyrite

BIC – Bushveld Igneous Complex

PGE – platinum group elements

RLS – Rustenburg Layered Suite

LZ – Lower Zone

PPL – Plane Polarised Light

XPL – Cross Polarised Light

BSE – Backscatter Electron Image

CZ – Critical Zone

CUZ – Upper Critical Zone

CLZ – Lower Critical Zone

MZ – Main Zone

UZ – Upper Zone

MML – Main Magnetite Layer

fO_2 - Oxygen Fugacity

EPMA – Electron Probe Micro analysis

XRF – X-ray Fluorescence Spectrometry

ICP-MS – Inductively Coupled Plasma Mass Spectrometry

SHRIMP – Sensitive High Resolution Ion Microprobe

HFSE – High Field Strength Elements

LILE – Large Ion Lithophile Elements

REE – Rare Earth Elements

LREE – Light Rare Earth Elements

HREE – Heavy Rare Earth Elements

ELIP – Emeishan Large Igneous Province

FMQ – Fayalite-Magneite-Quartz